

# Development and Testing of a Scale Model Clamshell Mucker, and Validation by Discrete Element Modelling

Steven Moss

A research report submitted to the Faculty of Engineering and the Built Environment, University of the Witwatersrand, Johannesburg, in partial fulfilment of the requirements for the degree of Master of Science in Engineering

February 2011

## **Declaration**

I declare that this research report is my own unaided work. It is being submitted for the Degree of Master of Science in Engineering to the University of the Witwatersrand, Johannesburg. It has not been submitted before for any degree or examination at any other University.

Steven Thomas Moss

..... day of ....., .....

## Executive Summary

Shaft sinking is an important part of the mining process, of which “mucking” (clearing the broken rock from the bottom of the shaft) plays a critical role. The aim of the research was to develop a scaled experimental replica of the so-called *Clamshell Mucker* and compare its performance, over a range of operating parameters, with those yielded by numerical simulations, for the long-term purpose of validating the simulation as a tool for optimizing the design of full-scale machines.

Towards this end a scaled experimental rig of the clamshell mucker was developed and tested over an appropriate range of geometrical and operating parameters, for two different materials: hard plastic balls and thereafter 13 mm decomposed granite stone. Hydraulic actuator forces were established by measuring line pressures, while angular rotation of the jaws of the mucker was monitored using an angular potentiometer. Simple analysis provided a relationship between actuator force and torque on the buckets. The stone in the muck reservoir was agitated after each test run, to ensure random particle arrangements with no structuring, and a constant digging depth.

Testing of the hard plastic balls was used to establish a qualitative comparison between Discrete Element Modelling (DEM) and physical testing, using both video and still photography comparisons, corresponding to the teeth initially touching the surface with a bucket closing velocity of 20 deg/s. Heuristic correlations obtained by this means were generally favourable.

Quantitative testing using 13 mm granite stone yielded the bucket closing torque variation with bucket angle for various combinations of:- (a) bucket closing velocity, (b) initial distance of the bucket from the muck pile, (c) proximity of the bucket to the side and front walls of the container, and (d) the angle at which bucket assembly enters the muck pile. The main set of tests took place with the bucket entering vertically and positioned in the middle of the bed. Three different initial distances from the surface to the starting position of the bucket teeth were investigated (20 mm, 10 mm and 0 mm), with bucket angular velocities of 10 deg/s, 15 deg/s and 20 deg/s. Thereafter, testing was conducted at the forward (polycarbonate) boundary of the container and one of the lateral boundaries (steel) respectively, each for a single bucket velocity of 20 deg/s and covering the three above-mentioned initial distances from the surface. This testing was performed in an attempt to simulate the proximity effects that would be encountered in practice - for example, digging close to a side wall. Finally, torque variations with bucket angle were established at four different angles of attack ( $0^\circ$ ,  $5^\circ$ ,  $15^\circ$  and  $30^\circ$ ), at a constant bucket closing velocity of 20 deg/s, with the closest portion of the bucket initially touching the surface.

Data was generally interpreted in the context of the fact the torque required to rotate the buckets appears to depend on an interplay between:- (a) the level of fluidization between particles in the bed, increasing with bucket closing velocity, results in a reduced torque; (b) particulate congestion, increasing as the initial distance from the surface of the granular material decreases, results in an increased torque; and (c) the momentum required to move the particles and change their direction, increasing with bucket velocity, results in an increased torque.

Accordingly, for the larger initial distances from the surface momentum effects are dominant, generally leading to an increase of torque with angular velocity. However, as the initial distance reduces, congestion becomes increasingly important, until for the zero initial separation case, the lowest angular velocity yields the highest torques, probably because fluidization has been inhibited.

Because particle to boundary interactions have lower friction than particle to particle interactions, torques in the presence of boundaries were lower than for the middle position in the initial stages. Beyond a certain point, proximity to the forward boundary led to congestion with a commensurate increase in torque above that of the middle case, whereas proximity to the lateral boundary led to

no congestion, so the torques remained generally lower than for the middle case.

When considering the effects of angle of penetration, it was found that the largest angle of penetration ( $30^\circ$ ) gave the highest torque in the initial stages, probably because the highest volumes of material are captured relative to other angles of attack. Beyond a bucket angle of about  $14^\circ$  congestion becomes increasingly dominant, with the rise in torque due to this effect generally delayed with increasing angles of attack. This phenomenon was ascribed to the fact that in all cases other than zero angle of penetration, only one jaw initially enters the material, with the second following at a later stage: therefore particles escape to a free surface for the mid-range bucket angles, with the onset of congestion commensurately delayed to the larger ones.

Comparisons between DEM data and measurements for various testing parameters showed that the simulated and physical results display similar values of torque towards the beginning and end of the digging motion, but DEM predictions are low in the middle of the range. This is thought to arise primarily from the fact that simplified particle geometries (smooth, with no sharp edges) were incorporated into the DEM model because of computational resource limitations, whereas the real granular particles have sharp edges and are blocky, thus increasing particle interlocking effects and the high level of congestion frequently exhibited in the physical experimentation. This effect was generally reflected by poor comparisons between DEM data and experimentation in the context of torque variations with velocity in the middle range of angular positions. Because the coefficients of rolling friction and restitution were obtained from published data, additional simplified simulations were run to determine the sensitivity of these parameters (in addition to static friction coefficient, for comparative purposes) on the force characteristics of the model. It was established that specifically chosen percentage changes in all of the parameter values relative to the base system led to percentages of force deviation that were at least 3 to 5 times smaller, reinforcing the inference that particle interlocking effects were the dominant reason for poor mid-range correlations between experimentation and the DEM modelling.

The maximum energy to fill the buckets was required at a zero angle of penetration, diminishing significantly to an angle of about  $15^\circ$  and then increasing once again. This trend is attributed to the fact that the  $0^\circ$  case is most affected by congestion, whereas the larger angles of attack (beyond about  $20^\circ$ ) cause the weight of the material to significantly affect the energy required to close the buckets. While it was considered possible that similar trends would be observed in practice, that could potentially reflect in improved operational guidelines for the mucking process, further analysis suggested that an energy saving of less than 814.3 kJ might be attainable for clearing a 6 m diameter shaft during a single cycle. While this appears to be inconsequential in the broader context, it should be subjected to a more comprehensive investigation in the context of full-scale cleaning strategies.

It is recommended that:- (a) the test facility be modified to extend the range of bucket angular velocities; (b) testing be conducted with a broader range of particle sizes; (c) research into the interlocking and frictional effects of rock be pursued, to create representative particulate shapes as input to the DEM model; (d) higher friction coefficients be attempted as a means of artificially compensating for interlocking effects that are impractical to achieve because of computer resource limitations; and (e) testing be conducted with a range of different bucket shapes and sizes for the purpose of optimizing the design by way of minimizing structural stresses and the specific energies required to collect individual loads.

## Acknowledgements

I wish to thank the following individuals most sincerely for their contributions towards this project:

Mr Terry Frangakis my primary supervisor, who has made himself accessible at all times on a day-to-day basis, and who has provided excellent ideas and interactions.

Dr Murray Bwalya from the School of Chemical and Metallurgical Engineering, for his valued tutelage in Discrete Element Methods.

Professor Ramsay Brierley and Mr Thomas Dessen for their broad inputs and insights.

Messrs Tim Wakefield and Rob Bradley of Murray and Roberts Cementation, who have provided excellent support and access.

# Contents

Declaration . . . . .	ii
Executive Summary . . . . .	iii
Acknowledgements . . . . .	v
Table of Contents . . . . .	viii
List of Figures . . . . .	xiii
List of Tables . . . . .	xiv
Nomenclature . . . . .	xv
<b>1 Introduction</b>	<b>1</b>
1.1 Background . . . . .	1
1.2 Literature Review . . . . .	4
1.2.1 Mining Equipment . . . . .	4
1.2.2 Granular Flow . . . . .	12
1.2.3 Discrete Modelling Techniques . . . . .	16
1.2.4 Modelling in DEM . . . . .	18
1.2.5 DEM Input Parameters . . . . .	22
1.2.6 Experimental Validation with DEM . . . . .	25
1.2.7 Developments in DEM Modelling . . . . .	26
1.3 Objectives . . . . .	30
<b>2 Development of Test Facility</b>	<b>31</b>
2.1 Preliminary Design Considerations . . . . .	31

2.1.1	Design Process . . . . .	31
2.1.2	Geometry of Test Facility; Force and Displacement Relationships . . . . .	32
2.1.3	Initial Experimentation - Hydraulic Cylinder Capacities . . . . .	35
2.2	Design of the Experimental Facility . . . . .	36
2.2.1	Frame, Primary Assembly and Muck box . . . . .	37
2.2.2	Hydraulic Circuit . . . . .	39
2.2.3	Instrumentation . . . . .	39
2.2.4	Velocity Control Mechanism . . . . .	40
<b>3</b>	<b>Numerical Modelling</b>	<b>41</b>
3.1	Physical Parameters . . . . .	41
3.1.1	Sensitivity Analysis . . . . .	42
3.2	DEM Model Development . . . . .	44
3.2.1	Development of the Particles . . . . .	44
3.2.2	Model Geometry . . . . .	46
3.2.3	Particle factory Configuration . . . . .	47
3.2.4	Simulation Parameters . . . . .	48
<b>4</b>	<b>Experimentation</b>	<b>49</b>
4.1	Calibration and Actuator Base Loading . . . . .	49
4.2	Experimental Method . . . . .	50
4.2.1	Testing Procedure . . . . .	50
4.2.2	Testing Hard Plastic Balls . . . . .	52
4.2.3	Testing 13 mm Decomposed Granite Stone . . . . .	52
4.3	Observations . . . . .	54
4.3.1	Hard Plastic Balls . . . . .	54
4.3.2	Decomposed Granite Stone . . . . .	54
4.4	Data Processing . . . . .	56

4.4.1	Hard Plastic Balls . . . . .	56
4.4.2	Decomposed Granite Stone . . . . .	56
4.4.3	Estimates of Energy Levels . . . . .	58
<b>5</b>	<b>Results</b>	<b>59</b>
5.1	Qualitative Data - Flow Visualization . . . . .	59
5.2	Experimental Data . . . . .	61
5.3	DEM Results . . . . .	66
5.4	Comparison Between DEM and Experimental Results . . . . .	69
5.5	Energy Levels . . . . .	73
<b>6</b>	<b>Closure</b>	<b>74</b>
6.1	Discussion . . . . .	74
6.1.1	Qualitative Data - Flow Visualization . . . . .	74
6.1.2	Quantitative Data . . . . .	77
6.2	Conclusions . . . . .	85
6.3	Recommendations . . . . .	88
6.4	References . . . . .	90
<b>7</b>	<b>Appendices</b>	<b>94</b>
	Appendix A - Bucket Torques . . . . .	94
	Appendix B - Determination of the Hydraulic Cylinder Parameters . . . . .	101
	Appendix C - Detailed Description of Test facility . . . . .	104
	Appendix D - Input Parameters and Sensitivity Analysis . . . . .	112
	Appendix E - Calibration of Angular Potentiometer and Base Loading . . . . .	118
	Appendix F - Raw Data . . . . .	124
	Appendix H - Technical Drawings . . . . .	129



# List of Figures

1.1	Schematic illustration of the cactus-grab lashing unit (Douglas and Pftzenreuter, 1989) . . . . .	5
1.2	A cactus-grab lashing unit in operation (Yardley, 1970). . . . .	6
1.3	An illustration of the 630 Loader lashing unit (Taylor, 1981) . . . . .	8
1.4	Operational motion of the 630 Loader lashing unit (Eimco, N.D.). . . . .	9
1.5	Clamshell Mucker unit in Operation (MacChonachie, 1959). . . . .	10
1.6	Schematic illustration of the Clamshell Mucker lashing unit (Cryderman, 1952). . .	11
1.7	Force chains as visualised by using particles made from a photoelastic material (Liu, 2009). . . . .	15
1.8	Fundamental basis for the linear spring contact model (Coetzee, 2009). . . . .	20
1.9	A dragline bucket (Cleary, 1999). . . . .	28
2.1	Design concept for testing facility. . . . .	33
2.2	Free body diagram of forces in the bucket and hydraulic actuator. . . . .	34
2.3	Schematic of experimental rig. . . . .	36
2.4	Photograph of experimental rig. . . . .	37
2.5	Schematic of experimental equipment and required instrumentation. . . . .	40
3.1	Sensitivity analysis: penetrating force as a function of varying physical parameters (coefficient of rolling friction and restitution and static friction . . . . .	43
3.2	A Solid Edge template of the decomposed granite . . . . .	45
3.3	Resultant spherical particle configurations for final particle shapes . . . . .	46
3.4	Geometry as defined in the EDEM programme . . . . .	47

4.1	Visual illustration of the different testing parameters. . . . .	53
4.2	Matrix describing the experimental parameter hierarchy. . . . .	53
4.3	Typical variation of voltage with time representing the pressure in the hydraulic cylinder and the angle of the bucket respectively. . . . .	55
4.4	Typical variation of torque with bucket angle for a bucket closing velocity of 20 deg/s, in the middle, starting at 20 mm from the surface of the material. . . . .	58
5.1	Motion comparison of the bucket part 1. . . . .	59
5.2	Motion comparison of the bucket part 2. . . . .	60
5.3	Motion comparison of the bucket part 3. . . . .	60
5.4	Motion comparison of the bucket part 4. . . . .	60
5.5	Variation of torque with bucket angle for various initial distances from the surface, at a constant velocity (20 deg/s) and a constant boundary position (middle). . . . .	61
5.6	Variation of torque with bucket angle for various bucket closing velocities at an initial distance to surface of 20 mm. . . . .	62
5.7	Variation of torque with bucket angle for various bucket closing velocities at an initial distance to surface of 10 mm. . . . .	62
5.8	Variation of torque with bucket angle for various bucket closing velocities at an initial distance to surface of 0 mm. . . . .	63
5.9	Variation of torque with bucket angle for various boundary conditions at an initial distance to surface of 20 mm. . . . .	63
5.10	Variation of torque with bucket angle for various boundary conditions at an initial distance to surface of 10 mm. . . . .	64
5.11	Variation of torque with bucket angle for various boundary conditions at an initial distance to surface of 0 mm. . . . .	64
5.12	Variation of torque with bucket angle for various angles of attack, at a constant velocity (20 deg/s) and a constant boundary position (middle). . . . .	65
5.13	Variation of torque with bucket angle for bucket closing velocities of 10 deg/s and 20 deg/s at an initial distance to surface of 0 mm. . . . .	67
5.14	Variation of torque with bucket angle for various bucket closing velocities at an initial distance to surface of 10 mm. . . . .	67
5.15	Variation of torque with bucket angle for bucket closing velocities of 10 deg/s and 20 deg/s at an initial distance to surface of 20 mm. . . . .	68

5.16	Variation of torque with bucket angle for various initial distances from the surface, at a constant velocity (20 deg/s) and a constant boundary position (middle). . . . .	68
5.17	Variation of torque with bucket angle for an initial distance from the surface of 0mm and a bucket closing velocity of 20 deg/s for simulated and physical cases. . .	69
5.18	Variation of torque with bucket angle for an initial distance from the surface of 0mm and a bucket closing velocity of 10 deg/s for simulated and physical cases. . .	70
5.19	Variation of torque with bucket angle for an initial distance from the surface of 10mm and a bucket closing velocity of 20 deg/s for simulated and physical cases. . .	70
5.20	Variation of torque with bucket angle for an initial distance from the surface of 10mm and a bucket closing velocity of 15 deg/s for simulated and physical cases. . .	71
5.21	Variation of torque with bucket angle for an initial distance from the surface of 10mm and a bucket closing velocity of 10 deg/s for simulated and physical cases. . .	71
5.22	Variation of torque with bucket angle for an initial distance from the surface of 20mm and a bucket closing velocity of 20 deg/s for simulated and physical cases. . .	72
5.23	Variation of torque with bucket angle for an initial distance from the surface of 20mm and a bucket closing velocity of 10 deg/s for simulated and physical cases. . .	72
5.24	Variation of energy required to fill the buckets with angle of attack. . . . .	73
6.1	Motion comparison of the bucket part 1. . . . .	75
6.2	Motion comparison of the bucket part 2. . . . .	76
6.3	Motion comparison of the bucket part 3. . . . .	76
6.4	Motion comparison of the bucket part 4. . . . .	77
7.1	Forces exerted by the cylinder on pin joints. . . . .	95
7.2	Forces exerted on a linkage. . . . .	96
7.3	Forces exerted on the bucket. . . . .	97
7.4	A schematic of the angular position of the cylinder relative to the linear position of the sliding pin. . . . .	98
7.5	The relationship between $x$ and the bucket angle. . . . .	98
7.6	Formatted EES equations. . . . .	100
7.7	Illustration of the experimental set-up to size the hydraulic cylinders. . . . .	102
7.8	Variation of load with time for a penetration velocity of 80mm/s. . . . .	103

7.9	Variation of average maximum load with descent speed. . . . .	103
7.10	Illustration of the stationary base assembly. . . . .	104
7.11	An illustration of the bearing assembly. . . . .	105
7.12	Illustration of the main body assembly. . . . .	106
7.13	Illustration of the clamshell configuration. . . . .	107
7.14	Illustration of the muck box. . . . .	107
7.15	Illustration of the assembly frame. . . . .	108
7.16	Schematic of the hydraulic circuit. . . . .	109
7.17	An illustration of the wiring diagram for the pressure transducers. . . . .	111
7.18	An illustration of the wiring diagram for the angular and linear potentiometers. . . . .	111
7.19	DEM model for the friction test using triangular particles. . . . .	113
7.20	Variation of time of flight with bounce number for granite on steel. . . . .	116
7.21	DEM geometry setup for the sensitivity analysis. . . . .	117
7.22	Calibration curve for the angular potentiometer. . . . .	119
7.23	Calibration curve for the bucket operation pressure transducer. . . . .	119
7.24	Calibration curve for the vertical motion pressure transducer. . . . .	120
7.25	Calibration curve for the linear potentiometer. . . . .	120
7.26	Variation of bucket angular displacement with time for a 20 deg/s closing velocity. . . . .	121
7.27	Variation of bucket angular displacement with time for a 15 deg/s closing velocity. . . . .	121
7.28	Variation of bucket angular displacement with time for a 10 deg/s closing velocity. . . . .	122
7.29	Free air (base) test for a 20 deg/s closing velocity. . . . .	122
7.30	Free air (base) test for a 15 deg/s closing velocity. . . . .	123
7.31	Free air (base) test for a 10 deg/s closing velocity. . . . .	123
7.32	Typical variation of torque with bucket angle for a bucket closing velocity of 20 deg/s, in the middle, starting at 10 mm from the surface of the material. . . . .	127
7.33	Typical variation of torque with bucket angle for a bucket closing velocity of 20 deg/s, in the middle, starting at 0 mm from the surface of the material. . . . .	128

7.34 Typical variation of torque with bucket angle for a bucket closing velocity of 20 deg/s, at the forward/polycarbonate boundary, starting at 0 mm from the surface of the material. . . . . 128

# List of Tables

2.1	Values of maximum force readings for various penetration velocities . . . . .	35
3.1	Comparisons between measured physical parameters and published values. . . . .	42
3.2	Global Physics Settings of the testing materials. . . . .	44
7.1	Systems constants . . . . .	99
7.2	List of parts for the Hydraulic Circuit . . . . .	110
7.3	Sample of the raw data generated, with a bucket velocity of 20 deg/s, in the middle of the granular bed and a penetration depth of 20 mm. . . . .	125
7.4	Sample of raw data converted into a pressure. . . . .	126
7.5	Sample of raw data converted into an angular displacement. . . . .	126

## Nomenclature

Symbol	Definition	Unit
A	Closed dead centre length of hydraulic cylinder	m
c	Horizontal distance between hydraulic cylinder pin and initial position of sliding pin	m
E	Energy employed to fill the buckets	J
$F_{B1}$	Force exerted by bucket 1	N
$F_{B1x}$	Resultant bucket force in the x direction	N
$F_{B1y}$	Resultant bucket force in the y direction	N
$F_{eff}$	Maximum force measured during preliminary experimentation	N
$F_{G1}$	Force exerted by the granular material on the bucket	N
$F_{L1}$	Force exerted by linkage 1	N
$F_{L2}$	Force exerted by linkage 2	N
$F_P$	Force exerted by the hydraulic cylinder	N
$F_R$	Reactive force of the sliding pin	N
$F_x$	Reactive force in the x direction	N
$F_y$	Vertical reactive force on the bucket pivotal pin	N
L	Length of linkage	m
$\ell$	Length of the bucket, from teeth to pivot point	m
R	Distance between pivotal pin and linkage pin	m
T	Torque required to close the bucket	Nm
x	Distance travelled by sliding pin	m
z	Vertical distance between hydraulic cylinder pin and initial position of sliding pin	m
$z_1$	Vertical distance between hydraulic cylinder pin and final position of sliding pin	m
$\alpha$	Angle between linkage and the vertical plane	deg
$\beta$	Angle between the bottom edge of the bucket and the horizontal	deg
$\gamma$	Measured angle of the buckets relative to the horizontal	deg
$\gamma_1$	Bucket angle, constant angular distance away from $\gamma$	deg
$\theta$	Angle between the hydraulic actuator and the vertical	deg
$\theta_1$	Initial hydraulic actuator angle	deg
$\Theta_{final}$	Final angular position of the Clamshell buckets	deg

# Chapter 1

## Introduction

### 1.1 Background

South Africa is one of the most important mining countries, both in terms of the variety and abundance of minerals produced. It has the world's largest reserves of chrome, gold, vanadium, manganese and platinum group metals and is also the leading producer of nearly all of Africa's metals and minerals production, apart from:- diamonds (Botswana and the DRC), uranium (Niger), copper and cobalt (Zambia and the DRC) and phosphates (Morocco) (MBendi, 2009). The mining industry is one of the most important in South Africa, contributing almost 8.8% to the Gross Domestic Product (GDP), and 19% indirectly through multipliers and secondary industries (*South African mining industry snapshot, 2009*). It is not only important in terms of the GDP, but the production of precious metals is also of critical importance for social stability through employment and sustainability of the economy.

Accordingly, it is necessary to continually improve the technologies employed in mining operations, to render mining processes more efficient, effective and safety-enhanced, potentially increasing production. Extensions of existing mines and new mining developments inevitably take place at increased depths and often at a reduction of ore grade; hence, more depth of shaft is required per kilogram of material produced. Within this environment, the science of shaft sinking has increasingly become a critical element on which the continued profit of this industry depends.

Shaft sinking represents a relatively short-term component of the activities involved in the life cycle



of a mine; because of this limited function, it has been neglected in terms of mechanization. It is a cyclical process, comprising a number of key processes and sub-processes. The main processes are drilling, blasting and lashing. Lashing is known to be the most time-consuming and dangerous of all these processes. It is the removal of the blasted rock (“muck”), from the bottom of the shaft to the surface. This is achieved by means of a lashing machine (or “mucker”). By way of process, the operator lowers the lashing machine into the muck and collects a load of rock, that is then swung into a large bucket called a “Kibble”. The kibble is then moved to surface where the rock is deposited. The cycle continues until all of the blasted rock has been moved to the surface. Typical shaft diameters in South Africa are between 6 and 11 m, and the advance per blast is roughly 3 m although this varies depending on the type of rock encountered and the accuracy of the drilling. The rock fragmentation size is dependent on drilling/blasting accuracy and ranges from 20 mm to 450 mm.

Although shaft lashing machines (muckers) were introduced more than 60 years ago, the first machines were low-capacity units (i.e. with small bucket volumes and relatively slow cycle times). Despite their advantages over manual labour, such machines did not gain wide acceptance by the mining industry until the late 1950's. However, the increasing depth of underground mines and the escalating costs of labour have amplified the benefits obtainable from high-speed shaft sinking - specifically, enhanced cycle times return better production rates. The result, therefore, has been a growing need for high-capacity shaft machines of all types (from drilling to lashing). Most of the machines available at the present time have been developed by altering existing equipment to increase the payload capacity and general performance. This implementation of change is however, slow and inefficient.

It is apparent that the evolution of mining equipment has been a sporadic process, because it is difficult to justify an investment in the change of major mining systems, especially when this is being done as in the past - through trial and error. This approach makes it extremely expensive and labour intensive and often does not, in the short term, give an immediate return on the investment. Furthermore, development costs are typically set off against a single project (rather than all projects that benefit as a result of the improvement); therefore, improvements are frequently considered non-viable, often hindering advances in mining technologies as a result. Therefore a more practical method for improving these systems is by initially deciding on operational requirements and capacities, and thereafter utilizing the various available computer packages to simulate the

operation of the various components included in the system. These allow the user to infer what effects (negative or positive) any physical changes make to the system's effectiveness. Accordingly, the performance of any operational component of the system may be improved, while minimizing development costs. This form of equipment optimization or improvement has been done extensively on large pieces of bulk moving equipment, such as dragline buckets. However, there is little evidence of research performed on smaller pieces of equipment such as lashing machines.

Murray & Roberts Cementation are embarking on a new direction in the context of shaft sinking, in the knowledge that one of the areas demanding improvement is the time intensive and dangerous lashing process. When the time taken to fill the kibbles is exceeded by the travel time to the surface, the main bottleneck eventually becomes the depth of the shaft. Hence, the efficiency of lashing is important until that inherent limit is reached. Furthermore, safety is of paramount importance throughout the entire shaft sinking life-cycle.

In order to improve the process (both in terms of production rates and more specifically safety), it has been proposed that M&R Cementation adopt the Canadian method for lashing, using a device known as the "Clamshell Mucker" mechanism. It comprises two opposed jaws at the end of a telescopic boom, with pneumatic cylinders for opening and closing the clamshell, as well as moving the telescopic boom in the horizontal plane. It uses pneumatic rather than gravitational energy to load the rock. Therefore it is much easier to control than current devices (see Section 1.2.1) and is capable of picking up the smaller fragmentation, rendering the process potentially less time consuming (particularly in the initial stages of the shaft sinking process). It is therefore a potentially safer and more productive method of lashing. However, like other pieces of mining equipment, its geometry is a consequence of trial and error rather than formal experimentation.

If the Clamshell Mucker mechanism is adopted as the preferred M&R lashing system it will form an important part of the shaft sinking cycle. Hence it is appropriate to investigate its operation and understand its behaviour, so that more informed decisions can be made regarding its use in this context. In the current investigation a scale model of the Clamshell Mucker will be built and tested. The mucking process will be simulated using Discrete Element Modeling (DEM) software and the modelled parameters correlated with the experimentation. This will lay the foundation for future work which could include the simulation and optimization of a full-scale system.

## 1.2 Literature Review

The current Literature Review involves two distinct parts relating to mining equipment (Section 1.2.1) and testing/modeling techniques (Sections 1.2.2 to 1.2.7). Mining equipment includes the various pieces of equipment available and specifically ways in which equipment has been optimized, within the context of mining.

### 1.2.1 Mining Equipment

Through the history of shaft sinking there have been numerous lashing methods. Initially it was performed manually; later, various machines were employed. In South Africa today the favoured machine for lashing is the Cactus-grab.

Increased safety standards and a drive for improved production rates make it necessary to ensure that the correct equipment is available for all tasks. The optimization and development of existing mining machinery has generally not been recorded properly and is often proprietary information. Hence, there is little information available on the alterations made to these machines and the effect it has on their capability. Therefore a basic outline is given in the following section on the development of three of the most pertinent lashing machines in the context of general shaft sinking - the so-called *Cactus-grab*, the *Boesman* (630 Loader) and the *Clamshell Mucker*.

#### **Cactus-grab**

The most popular mechanical cleaning units currently in use for lashing in South Africa are the pneumatically operated *Cactus-grabs*. It has been in use for about 60 years, and is perceived, by mining personnel, to be the most efficient mucker type. It is a turret mounted type of lashing unit with the cactus-grab attached for rock hauling. The basic system comprises a turret, or turntable, located on the underside of the shaft sinking stage. Attached to the turntable is a fixed length boom, approximately equal in length to the diameter of the shaft, so that it can rotate to position the grab at the desired hauling position. This rotation function is performed by a slewing pneumatic motor and gearbox. The grab itself is raised, lowered and moved radially by pneumatically powered and controlled winches. Thus the grab is radially and circumferentially traversed under the bottom

deck of the sinking stage, allowing the grab mechanism to be positioned at any point in the shaft bottom.

A schematic illustration of the Cactus-grab lashing unit is given in Figure 1.1 (Douglas and Pftzenreuter, 1989), while a machine in operation is illustrated in Figure 1.2.

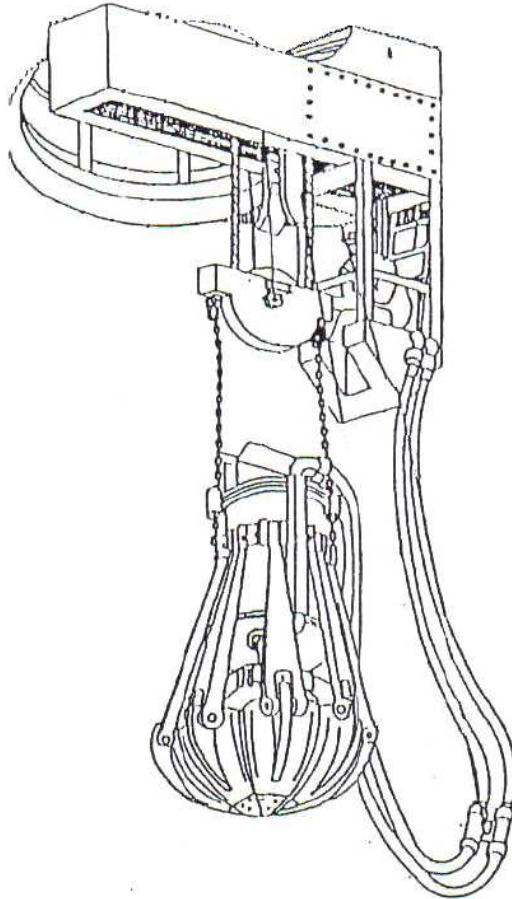


Figure 1.1: Schematic illustration of the cactus-grab lashing unit (Douglas and Pftzenreuter, 1989)

The machine was first introduced to South African shaft sinking in the 1960's and has several variations, with diverse energy types used to drive them. There are pneumatically operated units as described above, in addition to electrically or hydraulically operated devices. The primary reason for air operated units is the frequent presence of waste water in mining, which is hazardous in combination with electricity. Also, because the motion of the grab unit does not need to be inordinately accurate, it is possible to use air, because compressibility is thus not a serious issue. Despite its low efficiency (and potentially high life cycle costs), the capital cost of pneumatic equipment and control circuitry is considerably exceeded by its hydraulic counterparts.

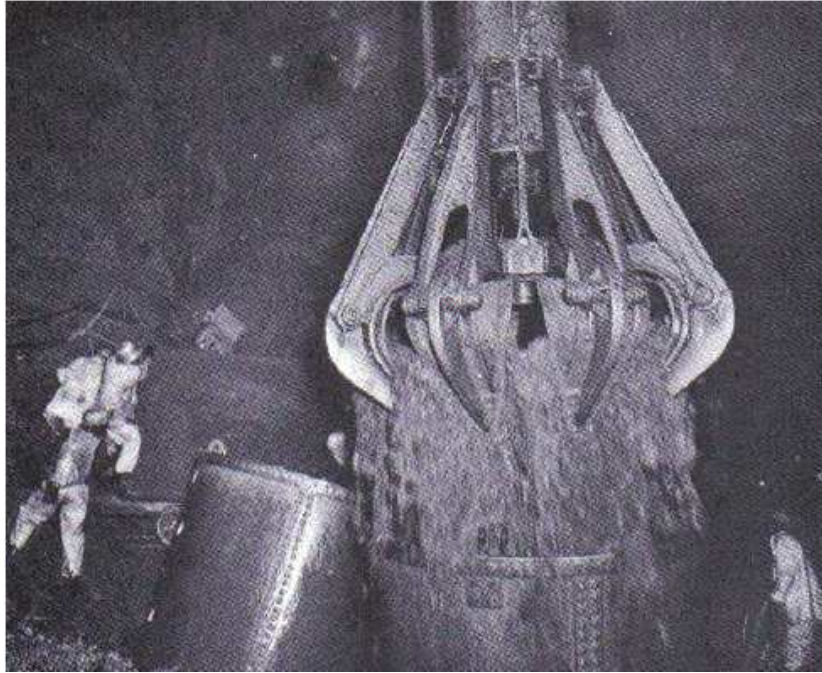


Figure 1.2: A cactus-grab lashing unit in operation (Yardley, 1970).

The Cactus-grab is an effective lashing unit, except for the following issues:

1. It is complex to operate and imparting the consequent skills require a minimum training period of about one year.
2. It is incapable of collecting very small fragments of rock, thus making it ineffective at the end of the lashing cycle when a shallow layer of loose rock remains.
3. It does not clean near the side-wall of the shaft very effectively. This is because the jaws/tines are open as it descends down, thus the closest it can get to the side wall is the length of an open tine away.

Improvements of this machine have been added in an *ad hoc* manner, with problems being identified and thereafter resolved in a production environment.

The advantages of using a Cactus-grab are as follows:

1. The position of the stage can remain constant, as the cactus grab descends towards the rock on a pulley system (unlike the clamshell mucker where the stage needs to be moved a number of times to enable the Clamshell to reach the muck at all times).

2. It is more capable of handling larger rocks than the 630 Loader or the Clamshell Mucker. This issue renders the process less time consuming, because larger rocks (mainly arising from poor drilling) do not need to be re-broken, or hauled separately using slings.

### **Crawler Mounted Rocker Shovel (630 Loader)**

In small diameter shafts (e.g. 6m) the predominant lashing machine is the crawler mounted rocker shovel (see Figure 1.3), affectionately known as the “Boesman” (630 Loader). The 630 Loader is a pneumatically operated loading machine, with three pneumatic motors, one driving each track and the third driving the shovelling mechanism. It is capable of operating in very restricted areas, because of its maneuverability (Wollers, 1989). This is reflected in its ability to spin about its own centroid (resulting in a zero turning circle). The third motor is independent of the others, enabling it to drive the shovel over the top of the machine so that the rock it contains lands behind the loader (in the kibble). This motion is illustrated in Figure 1.4.

The original loaders were built with a rounded digging lip and standard tracks. Based on intermittent modifications it became a more capable lashing unit. The development took place as follows (Taylor, 1981; Wollers, 1989):

1. Removal of a rounded lip that was replaced with a pointed tip, affording it added digging capabilities through better penetration abilities.
2. The bucket was reinforced, and iron added to the back plate to strengthen the machine structurally. This gave it better strength - leading to less frequent breakdowns and hence more convenient maintenance schedules.
3. An iron channel was added to the back plate to strengthen it.
4. Steel bars were welded onto the tracks, improving grip on the loose rubble - enabling the loader to spin about its centroid without slipping.

The nature of the 630 loader is such that it is primarily used for lashing in smaller diameter shafts, due to the fact that (a) in larger diameter shafts the lashing process is more conducive to standard lashing procedures, and (b) the 630 loader is known as being extremely dangerous. Hence, the use

of the 630 Loader is minimized where possible. Immediately after the blasting process has been completed, the 630 Loader is lowered to the shaft bottom, where the previous crew has flattened the blasted rock (this is to ensure that the 630 Loader does not topple over from loading the muck on an uneven surface). The loader is then positioned with its tail-end against the side wall. The loading bucket is lowered, and the loader moves forwards until the bucket is full. The bucket is then lifted out of the excavated rock. The loader positions itself with its back against the kibble; at this point the bucket is lifted over the loader and emptied into the kibble. The range of movement is described in Figure 1.4. The process is continued until the kibble is full. The kibble then ascends and the loader begins to fill the next kibble. This process continues until all of the blasted rock on the bottom of the shaft has been cleared (Yardley, 1970). There are a number of attributes which account for the popularity of the machine (MacChonachie, 1959); these include its simplicity of construction, compactness of design, robustness and relative affordability.

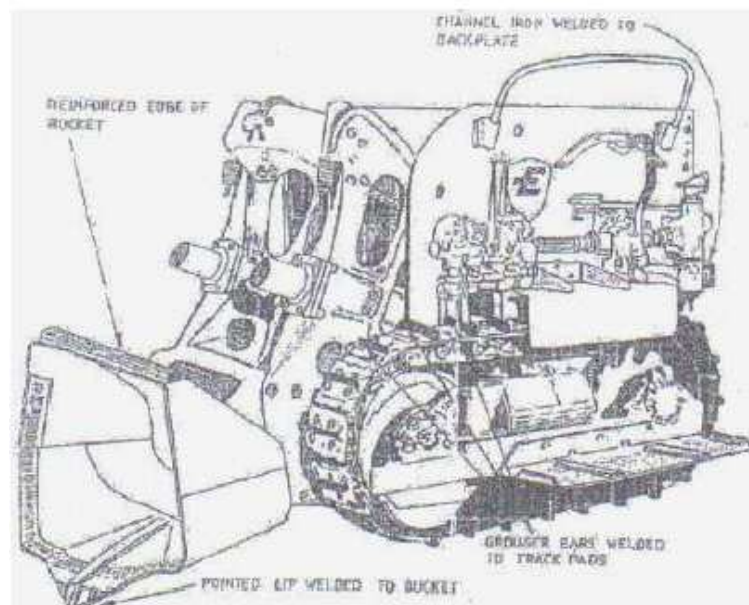


Figure 1.3: An illustration of the 630 Loader lashing unit (Taylor, 1981)

There are also factors which account for the reluctance to use this machine for lashing. These are as follows (Yardley, 1970; Taylor, 1981):

1. It has substantial acceleration and can lift very heavy loads for its size; therefore the momentum of the rock being thrown can cause the loader to tip under the control of an inexperienced operator.

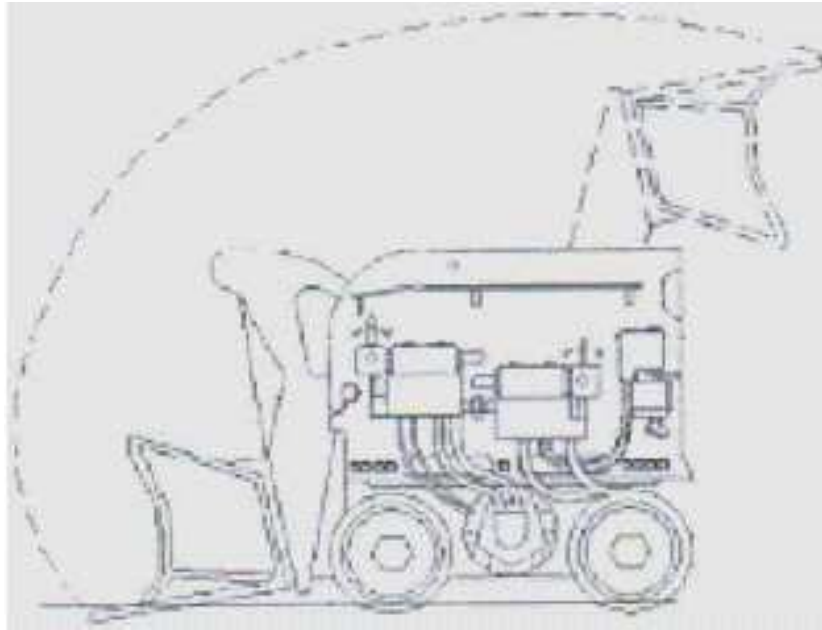


Figure 1.4: Operational motion of the 630 Loader lashing unit (Eimco, N.D.).

2. Being pneumatically operated it is very loud, and the ergonomics of the machine are such that it is difficult to see other humans in the periphery. This renders it extremely dangerous for other personnel in the shaft.
3. Time is lost in lowering the loader to the shaft bottom and returning it to surface for each cleaning cycle.
4. Cleaning speed is lost in the first hour, as manual labour is required to flatten the blasted rock pile before the 630 loader can be safely operated.
5. Cleaning speed is reduced due to the smaller kibble that needs to be used to compensate for the lower height that the 630 Loader's bucket can reach. This kibble is roughly half the size of a normal kibble used by a Cactus-grab, for example.

Elaborating specifically on item 1 above, accurate control of the 630 Loader is very difficult. The operator stands laterally on the machine, facing a control panel containing a number of levers - each one of which has a specific function. The controls are essentially pneumatic valves which, when opened, have a significant delay preceding activation of the pneumatic motors that they control (because of the air compressibility). Thus it takes a skilled operator to control the 630 Loader safely and accurately.



### Clamshell Mucker Lashing Unit

The Clamshell Mucker Lashing Unit is an arm-gathering lashing unit, mounted on the periphery of the shaft under the stage (see Cryderman, 1952). A steel cage above the unit is used as a mounting for the boom and is also the control point for the operator. It operates on the combined principles of a swingable, telescopic boom with a clam mounted on the free end, and an operator-actuated means for swinging, extending and retracting the boom and for opening and closing the clam (or bucket, depending on the loading capacity). The clamshell arrangement consists of two buckets controlled pneumatically. The telescopic boom is able to extend to any portion of the shaft bottom. Figure 1.5 is a representation of the lashing unit, while Figure 1.6 is a schematic of the equipment.

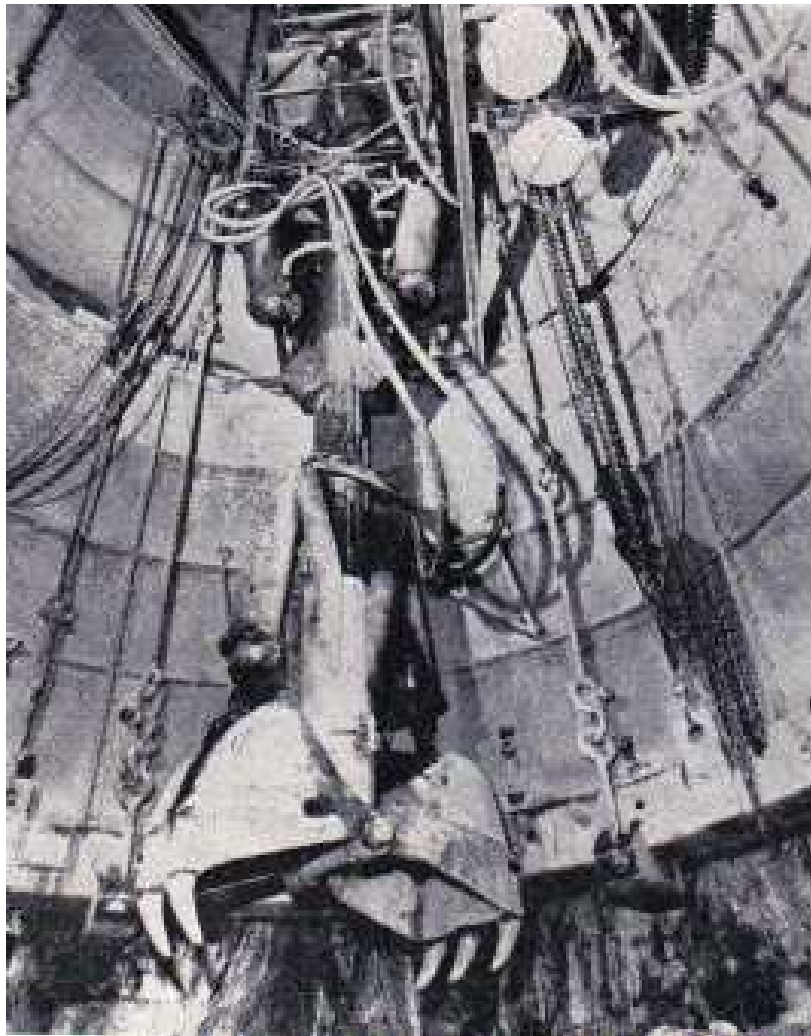


Figure 1.5: Clamshell Mucker unit in Operation (MacChonachie, 1959).

The Clamshell lashing unit is able to operate in many different environments - applicable in both vertical and inclined shaft sinking operations. As with other methods, the crew are required to

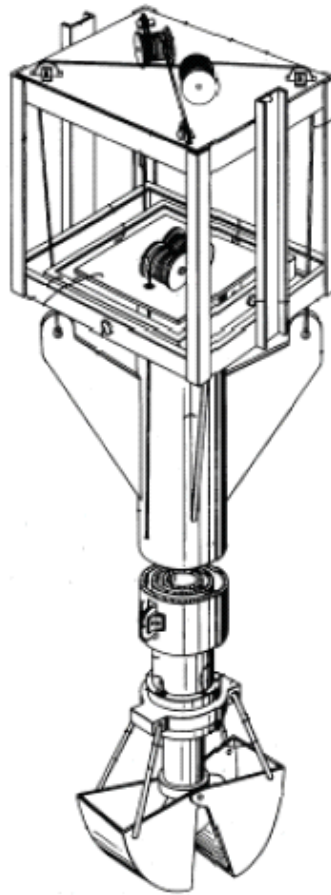


Figure 1.6: Schematic illustration of the Clamshell Mucker lashing unit (Cryderman, 1952).

position the kibble while the machine operates (MacChonachie, 1959). The original Clamshell mucking machine is operated in the way described above; however, since its advent there have been many variations of the same concept. In modern times it has become the chosen method for lashing in some mining countries (such as Canada and Australia), for the following main reasons:

1. It is capable of collecting smaller fragmentation, negating the need for a so-called *blow-over* where, in the context of Cactus-grab lashing, compressed air is used to move all the smaller fragments into a pile, which is thereafter manually deposited into a kibble.
2. It is capable of lashing in a small diameter shaft, its range of motion allowing it to be of use in both a larger (8 m to 11 m) or smaller ( $\leq 5$  m) diameter shafts.
3. It is able to collect fragments at the side-wall much more easily than other methods.

There are certain disadvantages associated with the use of the Clamshell Mucker, these include:

1. It not able to haul larger rocks. This issue renders the process time consuming, because larger rocks need to be re-broken, or hauled separately using slings (although this is a common problem to lashing in general, primarily due to poor drilling).
2. The stage needs to be continuously moved towards the rock fragmentation. The clamshell has a telescopic boom that does not extend as far as the depth of the blasted material.

The Clamshell Mucker unit has been altered throughout its history, in an attempt to improve its operational efficiency. The original Clamshell mucker had a relatively small loading capacity (about 0.143 m<sup>3</sup>) and boom reach (approximately 7.47 m); however these were altered to suit different mining scenarios. No formal testing has been performed on this type of a machine, hence design alterations have been based on experience and operational failures. This type of mucker is a subset of that which is to be considered in the current investigation. Modern capacities for the bucket are 0.573 m<sup>3</sup>, with a 10.97 m boom length.

## **1.2.2 Granular Flow**

There is a massive range of applications for which granular flow is a dominant component, for example:- separation and mixing in the pharmaceutical industry, grinding and crushing, blasting, stockpile construction, generic flows in and from hoppers, silos, bins, conveyer belts and many more (Coetzee, 2009). The processing of granular material within the context of these applications consumes roughly 10% of all the energy produced on the planet, and hence on the scale of priorities of human activity it ranks second, immediately behind the supplying of water (Rhodes, 1998). As such, any advance in understanding the physics of granular material is bound to have an economic impact. The understanding and subsequent optimization of machinery and equipment in this field is perceived to be limited, despite the fact that methods of transport, storage and mixing are important in all stages of the industrial processing of granules.

Granular materials, such as sand and clay, are complex materials exhibiting solid and fluid properties. There are three reasons for this: firstly geomechanic materials, such as soil, are three-phase

mixtures (i.e. of solid, liquid and gas). The second is that granular materials display discrete element rather than continuous flow characteristics at a microscopic level. The third is that natural soil is inhomogeneous. For these reasons, it is difficult to construct relevant theories for granular materials to analyse their behaviour. However, two common approaches have arisen towards formulating the behaviour of granular materials: a microscopic approach considering a completely discrete structure and a macroscopic approach based on continuum mechanics. A generic theory for granular materials has not yet been proposed, therefore granular behaviour is often analysed empirically.

Particulate systems consist of a large number of particles interacting in varying and intricate ways, leading to complex behaviour which is difficult to understand, predict and quantify at a macroscopic scale. At this stage no adequate analysis exists; therefore further development in the understanding of granular behaviour is required before an acceptable generic approach may be conceived (Zhu, 2008). Within the context of the current investigation it implies that numerical methods are necessary to analyse granular flow.

There are many phenomena in granular flow that are not well understood and not easily quantifiable. Three of these issues are discussed below, because they are important in the context of the current investigation.

### **Resistance in a Granular Medium**

The mechanics of drag in granular matter has not yet been fully characterized - and even simple cases, such as solid objects moving slowly through the granular matter, are not fully understood. The movement of an object through a granular bed is important in the context of the current investigation, so that the physical effects resulting from the bucket interacting with granular material may be explained.

The properties of drag are related to the complex nature of stress propagation in the granular bed. This is because drag is affected not only by the particles in direct contact with the object moving through the bed, but through successive layers of particles supporting the object in all planes. Thus, a complex stress “chain” is formed, whereby any force applied to a granular medium is resisted non-homogeneously and anisotropically (Pfeifer, 1999). These effects originate from a complex

interaction between factors such as surface friction, shape and size distribution. In order for an object to move through (or within) a granular medium, all of the grains impeding its motion must be displaced, requiring a large-scale reorganization of the material. This non-uniformity of the force propagation and the grain reorganization give the force a dynamic character, characterized by the fluctuating force between the grains resulting from the strain building and then being released by reorganization of the grains.

Pfeifer (1999) performed tests with cylindrical objects which were moved axially through a granular bed. The finding suggested that the penetrating force required to move the cylinder into and through the granular material is not dependent on velocity at lower velocities of penetration. However, this is not valid for higher penetration velocities that cause fluidization of the bed in the region ahead of the cylinder. Within the context of the current investigation different bucket closing velocities are important in understanding the mechanics of digging with the clamshell mucker.

### **Force Chains and Stress Propagation in Granular Media**

Granular media consist of many particles interacting through various contacts. Even uncomplicated, loosely packed uniform beds of granular materials (such as a bed of “identical” spheres) can display highly variable, non-uniform networks of contacts. Small imperfections on the surface of a “smooth” sphere, or slight deviations of particle sizes are sufficient to create a complicated contact network (Wambaugh, 2010). Stresses induced by an applied force are distributed to the rest of the medium through this contact network (seen in Figure 1.7, where  $\delta$  represents the penetration depth of an object). This distribution of contacts is termed a *force chain*. These force chains do not form along regular pathways, but rather radiate out randomly, originating from a certain area (da Silva, 2000). This is important in explaining the effects of congestion<sup>1</sup> and particle compaction on the torque required to close the clamshell bucket.

### **Boundary conditions**

While numerous attempts have been made to explain the effect of jamming or locking of particles in close proximity of a bottom (horizontal) boundary, little research on vertical boundary effects

---

<sup>1</sup>In this context *congestion* is the clumping together and consequent jamming of a collection of particles.

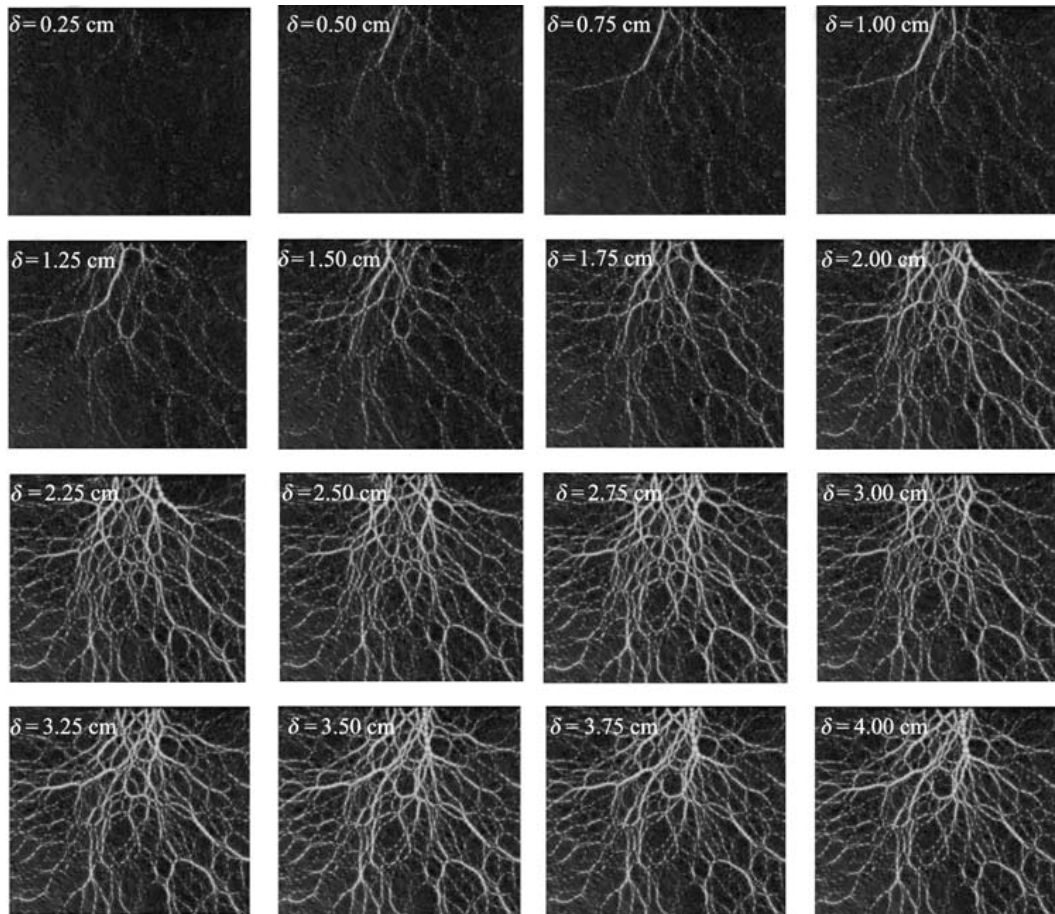


Figure 1.7: Force chains as visualised by using particles made from a photoelastic material (Liu, 2009).

has been found. Rather insights have been derived through experimentation, where vertical boundary effects were of a secondary focus.

Tests conducted by Stone et al (2004) have shown that the resistive force increases drastically as a penetrating object approaches a bottom boundary. This arises from the fact that rigid granular structures, known as *jammed states* are formed as the penetrating object approaches the bottom boundary. Due to the congestion of particles, arising from space constraints associated with a fixed boundary, the particles are unable to collapse and rearrange themselves.

Stone et al (2004) conducted basic tests wherein the vessel diameter was altered while the material size, penetration velocity and penetrating tool were kept constant. These tests indicate that the penetrating force is approximately constant beyond a specific magnitude of diameter (depending on the characteristics of the granular material) and thereafter it increases for smaller diameters. This is explicable by the fact that the space available for the particles to move has become insufficient,

leading to an increase in the potential for collections of particles to form jammed states (Sim, 2010).

### **1.2.3 Discrete Modelling Techniques**

In an effort to understand inter-particle behaviour, numerical modelling techniques similar to finite element analysis, known as Discrete Element Modelling, have been developed. There are various discrete modeling techniques available for use, namely: discrete element methods (DEM), numerical methods (e.g. finite element and finite difference methods) and continuum modeling. This investigation has adopted DEM as its primary method for investigating granular flow. Other methods, and the reasons for disregarding them, are discussed below.

#### **Numerical Methods**

Familiar numerical methods available to solve partial differential equations in the formulation of continuum effects are finite element modeling (FEM) and the finite difference (FD) method. The finite element method has evolved into the standard for solving a wide variety of solid mechanics problems, such as stress and fatigue problems in structures and mechanical components etc.

Granular assembly problems are not well suited to conventional FEM and FD methods. The fundamental basis of these methods, which has a reliance on a defined mesh, does not properly manage discontinuities, specifically when these deviate from the original mesh lines (Coetzee, 2008). A strategy for dealing with moving discontinuities (for example fracture lines) using these methods is to re-mesh at each time-step of the simulation. This has implications for computational time, which is negatively affected by a large number of re-meshings (Coetzee, 2008). The crack propagation through discrete materials is inherently discontinuous and unpredictable, because the material is non-uniform and anisotropic. Hence, this method of modelling granular flow was not considered.

#### **Continuum Modelling**

For some engineering applications, it is convenient to study the behaviour of a material body by assuming the matter to be continuous. Continuum systems can be thought of, microscopically, as

a collection of a large number of deformable particles that interact in such a way as to define the macroscopic behaviour of the body (Coetzee, 2008).

This simplifying assumption allows for the individual particle structure of the matter to be disregarded and to regard it as a single, continuous entity. This study of the behaviour of matter is accomplished by applying the classical laws of mechanics and thermodynamics and characterizing the properties of matter at a point. The theory describing the behaviour of such a material is called *continuum mechanics* (Coetzee, 2008). Granular material in continuous motion (e.g. on a conveyor-belt) can exhibit continuum properties; however when there are inconsistencies or interrupted flows (as in the case of excavation of granular materials) they do not. Therefore, this argument suggests that continuum mechanics is an inappropriate method of analysis in the context of the current investigation.

### **Discrete Element Methods**

The Discrete Element Methods (DEM) is equivalent to the molecular dynamic simulation used for gas, liquid and solid phases (i.e., computational fluid dynamics), illuminating the fundamental behaviour of granular matter. It considers material as discrete particles and simulates the interaction between particles by considering effects such as friction, force and momentum transfer etc. DEM has the ability to handle numerous problems with diverse foci, ultimately adding to its popularity and the reason it has been generally adopted for particulate/granular research. In the past two decades there has been rapid development and wide application of discrete particle simulation, in parallel with the development of computer technology (Cleary, 2003).

DEM has been used for the past 30 years, primarily for modelling various industrial applications. It was developed and used by Cundall and Strack (1979) in the field of rock mechanics and soil behaviour (Cleary, 2003). It originally comprised limited geometries in two dimensions, such as chute flows and, small hoppers. This led to small scale (100 to 1000 particles) with idealized assumptions in industrial applications, including basic systems such as ball mills and hoppers. Through the 1990's the problems became far more complicated, with greater numbers of particles, but models were still generally two-dimensional, or three dimensional with extremely simple geometries.



There are two types of DEM models, the *soft-particle* and *hard-particle* methods (Zhu, 2007). In the soft-particle method, minute deformations of the particle are allowed, and these deformations form the basis from which the elastic, plastic and frictional forces are calculated between particles. Soft-sphere models are capable of handling multiple particle contacts, which has merit when modelling quasi-static systems. In hard-sphere modelling a sequence of collisions is processed, one collision at a time - being instantaneous often the forces are not considered explicitly. Therefore, this is often more useful in rapid granular flows, while soft-sphere methods are more extensively used to study phenomena such as particle packing, transport properties, heaping/piling process, hopper flow, mixing and granulation (Zhu, 2007). DEM has been coupled with computational fluid dynamics to describe particle-fluid flows such as fluidization and pneumatic conveying.

DEM has currently progressed to the point where large scale industrial applications can be modelled with an appropriate qualitative comparison to reality (a deciding factor in choosing the modelling method). Large scale DEM models can be said to have the following attributes:

1. Models with at least 100 000 particles and often in excess of 1 million particles.
2. Very complex geometrical boundaries, sometimes requiring complex kinematic motion.
3. Non-ideal particle shapes - spherical particles are too idealized except for very limited applications.
4. Commonly used in conjunction with complex physics i.e. breakage, cohesion, particle deformation, etc.

#### **1.2.4 Modelling in DEM**

The DEM modelling process observes each particle's motion in the flow, while monitoring collisions, both between combinations of particles and between particles and their environment (e.g. the boundary walls of a chute, bucket etc). In order to solve a DEM problem, individual particles in the domain must be identified and tracked during simulations. The next step is to formulate and solve a system of equations of motion of the particle system. Finally, the change in contact between the particles is calculated and updated for use in the next iteration.(Ling, 2003). Effectively the particles are allowed to overlap and the amount of overlap  $\delta x$ , together with normal and tangential

velocities ( $v_n$  and  $v_t$  respectively) determine the collisional forces via a contact force law. Calculations performed during a DEM simulation cycle alternate between the application of Newton's second law (applied to the particles) and a force-displacement law (applied at the contacts between particles). Generally a linear spring-dashpot model is used, although there are numerous contact models available for use depending on the specific application (e.g. transportation of slurry versus crushing of dry rock).

### Contact Models

Contact models have been developed for use in DEM software - these models describe the physical relationship between particles moving relative to one another in a particulate bed. The most commonly used models are the Linear Spring and Hertz-Mindlin contact models. Cundall and Strack (1979) created the first model which works on the principle described in Figure 1.8, two particles interact by means of a spring-damper system. Using this approach (also known as the soft-particles approach), each particle contact is modelled as a linear spring in the contact normal direction (secant stiffness  $k_n$ ) and a linear spring in the contact tangential direction (tangent stiffness  $k_s$ ), while frictional slip is accounted for in the tangential direction with a friction coefficient  $\mu$ . The particles are allowed to overlap ( $U_n$ ) and the amount of overlap is used in combination with the spring stiffness to calculate the contact force components (the relationship is characterized by equation 1.1). The linear spring model can be improved through adding damper elements in parallel with the spring elements. With these enhancements, the model becomes known as the Hertz-Mindlin contact model (Coetzee, 2009). In the past, to improve computation time, simple discs or spheres were used in 2-Dimensional and 3-Dimensional problems respectively (using simple shapes helped make defining the overlap of particles much easier). With computer enhancements and better DEM software packages, particles can be modelled as complex arrangements of spheres (Coetzee, 2009).

$$F_n = k_n U_n \quad (1.1)$$

Contact models exist for a range of different applications, this is achieved by altering the model to include such features as cohesion and adhesion between the granular particles and boundaries. Furthermore, bonding between particles can also be simulated, useful for simulating side wall collapses (and other comparable situations). Within the context of the current investigation these

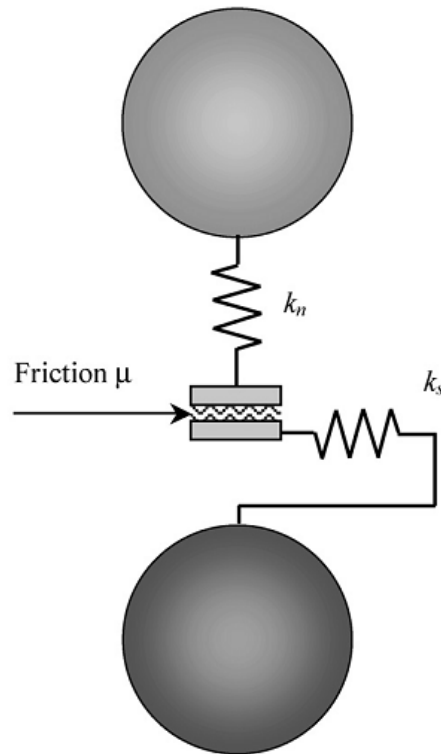


Figure 1.8: Fundamental basis for the linear spring contact model (Coetzee, 2009).

effects do not have any particular relevance since the particles in the experiment display neither bonding nor cohesion properties - primarily because the moisture content of the stone is so low that it will be assumed to be negligible. Future investigations, where a combination of mud and rock is used, will take consideration of the different contact models.

Presently the benefits of one model (e.g. the linear spring or Hertz-Mindlin model) over the other is not immediately obvious; nonetheless, each possess specific advantages. The linear spring is theoretically faster to compute (due to the simplicity of the model). However, optimization of the computer code and improvements in computer processor ability mean that it is common for the Hertz-Mindlin model to solve simulations almost as fast. The linear spring model allows for a larger time-step to be used during simulations, resulting in conservative force predictions when compared to that of the Hertz-Mindlin model. The linear spring stiffness is not based on physical laws, rather “the stiffness is calculated using maximum Hertzian strain energy and maximum existing contact energy..” (DEM training manual, 2010). Therefore it is better to use when requiring qualitative rather than quantitative results. The above arguments infer that the most appropriate contact model in the context of the current research would be the Hertz-Mindlin contact model.

## **Boundaries in a DEM Model**

Boundaries within the context of a DEM model, are generally represented in three ways: as fixed boundaries, applied traction boundaries or absorbing boundaries.

In fixed boundaries, displacement and rotation may be fixed in one or more of the coordinate directions. Modelling sometimes involves matter which are better represented as unbounded (i.e. large loosely packed beds). This is achieved by setting numerical boundaries at appropriate distances from the points of action. In typical confined laboratory penetration tests, the volume of the container is chosen such that the boundaries are sufficiently far afield so as to effectively replicate an infinitely large particle bed (Coetzee, 2009).

Applied traction boundaries are continuously moving boundaries exhibiting high surface friction coefficients. They are generally used in bulk handling problems, specifically in cases where conveyor belts or other continuously moving boundaries are used. In numerical simulations of wave propagations, it is sometimes important to eliminate effects such as the reflection of waves off fixed boundaries. Absorbing boundaries achieve this aim by essentially nullifying the effects of the wave at the boundary (Kosloff, 1985). Neither of these types of boundaries is relevant in the context of the current investigation.

## **Input Conditions**

Another fundamental concept of modelling granular flow is ensuring that initial conditions are correctly specified. These are needed to obtain specific solutions of the partial differential equations that describe the mechanics of granular flow. In many situations the precise initial stress field is unknown. In some straightforward cases one is able to calculate it analytically, but in most practical problems this is impossible to do accurately. Arising from the fact that it can have an influence on the results and the stability of the computation, it is important to specify realistic initial conditions. These specifically include parameters such as the correct contact model to be used (discussed in Section 1.2.4), the shape and size of the rock particles, the normal and shear stiffness (if necessary, depending on the contact model employed), the bulk density, size distribution, the static and rolling friction as well as the coefficient of restitution. These parameters may sometimes be obtained from literature, however in cases including uncommon materials the initial condition values for each of

the parameters must be obtained experimentally. These initial parameter values are expanded upon in Section 1.2.5.

### 1.2.5 DEM Input Parameters

It is necessary to prescribe the correct parameters for modelling granular material in DEM, so as to imitate as closely as possible the physical effects. The correct parameters include the geometrical characteristics (such as shape and size distribution) and physical characteristics (such as density, shear modulus, Poisson's ratio etc.). The effect of shape, blockiness<sup>2</sup>, aspect ratio and size on the flow of granular material is of great interest, from a practical and rock mechanics point of view, to gauge what either the positive or negative effects of these parameters is in terms of granular flow. These parameters should be modelled so that the inherent mechanical and geometric characteristics of the material used may be mimicked by the numerical model. Much research has been performed on imitating the rock properties - both physical and geometrical (Coetzee, 2009) - so that these rock parameters may be used to improve the correlation between physical and numerical measurements.

By way of example Wang et al (2004) used x-ray tomography to discern exact shapes of various particles and then simulated their physical properties and geometries in DEM using two different methods; the clustering method and the ellipsoidal method. The cluster method represents replicas of the real particles by combining a set of large or small spheres clumped together, while the ellipsoidal method incorporates a single idealized particle which has the same mass, momentum and principal axis directions as those of the real particle. The clustering method more accurately represents the exact particle shapes, however requires a larger number of spheres, thus extending the computing time for any simulation. The ellipsoidal method was found to be less accurate, but had the advantage of being more simple to achieve. The use of these methods in representing model particles was thought to return better simulation results (Wang, 2007). This work has been invaluable in developing an understanding of the effects of particle geometry on granular flow.

Within large DEM models particles are generally represented as spheres. There are a number of incentives for this. Most significant is that it reduces the computation time, by reducing the contact detection and contact force calculations. Using spherical particles means that the frictional prop-

---

<sup>2</sup>Blockiness is a description of how much the shape of a particle represents a block.

erties of the material are much lower than that of the physical material. Non-spherical particles are required to simulate the effect that interlocking has on granular flow; a potential solution is to make use of clustered particles (using spheres) to emulate exact particle shapes (as mentioned previously). Another solution is to increase the internal and static friction coefficients of the material within the DEM domain, to a point where the friction in the programme approximates the physical frictional properties. It then becomes unnecessary to create many unique particles (each individual, irregularly shaped particle). Hence, a simple particle geometry may be generated, in conjunction with accurate frictional properties, that mimics the effects of particle interlocking and other behaviour resulting from the non-standard particle shapes. In EDEM (the programme to be used to simulate the Clamshell Mucker), templates of the particles may be created; thereafter clumps of particles are used to simulate the actual particle. Within these clusters particles can overlap one another to any extent, but contact forces are not generated between these particles in the clusters.

The method to be adopted in the current investigation would be a simple representation of the clustering method (with simplified particles composed of only a few spheres, this is further explained in Section 3.2.1), in combination with frictional parameters (these are obtained either through experimentation or published literature). It is expected that the DEM results will return lower values for penetration forces and moments, as the interlocking effects will be less significant than when compared to physical testing (a result of the simplified particle shapes).

In addition to obtaining the correct particle geometry, it is necessary to match the simulated particle parameters as closely as possible to the physical properties of the rock. This usually requires testing the specific material concerned to determine the relevant parameters. However, physical tests require sample preparation which could alter the properties significantly (e.g. artificially creating spherical particles). This is particularly problematic where irregularly shaped particles are to be tested (e.g. sharp, angular particles of rock). In this context, experimental determination of these parameters is difficult and published data is often used, with the understanding that variations of the actual parameter values could have a potentially significant effect on the results. The results are therefore interpreted accordingly.

The most important physical parameters in terms of DEM numerical models are; static friction co-efficient, rolling friction and coefficient of restitution. The size and shape are also important, however these have been discussed previously (Coetzee, 2008). These pertinent parameters are

discussed below.

### **Coefficient of Static Friction**

Static friction is a resistive force counteracting the lateral movement of two objects touching each other. This results from the interlocking of irregularities between two surfaces. The force will increase to prevent any relative motion up until some limit thereafter the two surfaces move past one another (Nave, 2005). Within the context of the current investigation, static friction arises through two effects: particle interlocking (a result of shape and size distribution) and the contact friction between individual particles (arising from the surface finish).

The typical experimental method employed to determine the static friction is to tilt a plate made from one test material until a particle made from the second test material starts to slip. The angle made between the horizontal and the plate at the point of slip may then be used to evaluate the friction coefficient.

### **Coefficient of Rolling friction**

When a body rolls on a surface, both the body and the surface can deform to oppose this rolling motion. This is usually represented as a torque being applied to each of the bodies. The coefficient of rolling friction is a scalar value used to determine how much torque is needed to be applied to an object of a given material at rest on a flat surface to put it into motion (Simanek, 2010).

The simplest method for determining the coefficient of rolling friction is to roll a perfectly spherical sample of granular material down an incline from a known height. The distance it travels along a flat plate, composed of the second test material, before coming to a halt is recorded. The ratio of the ramp height and distance rolled can thereafter be used to calculate the rolling friction coefficient.

### **Coefficient of Restitution**

The coefficient of restitution is the ratio of speed of separation to speed of approach in a collision between two bodies and accounts for the energy lost in the collision (Baker, 2010). The stan-

dard testing procedure would embody a perfectly spherical sample of the granular material being dropped from a fixed height onto a large piece of the second test material. Thereafter the coefficient of restitution is then equivalent to the square root of the ratio between rebound height and drop height, that can be readily inferred by timing the successive contacts (decay rate) of a solid particle with the surface.

Section 3.1 discusses the methods by which these parameters are obtained.

### **1.2.6 Experimental Validation with DEM**

A granular medium consists of distinct particles which can displace independently from one another and interact only at contact points. The discrete character of the medium results in a complex behaviour under conditions of loading and unloading. To date no satisfactory constitutive relationships have been established to describe the fundamental behaviour of granular materials in this context. Interpreting the experimental data thereafter is difficult as stresses within the material are not easily measurable, hence are generally estimated from boundary conditions (such as force impingement on the boundaries etc).

Various papers have presented the validity of using DEM (and other methods) as an approximation of reality through modelling and computational experimentation:

Cundall and Strack (1979) looked specifically at the validity of using discrete modelling techniques to simulate the mechanical behaviour of discs and spheres. The distinct method used was that of a soft-particle DEM model in which the interaction of particles is monitored contact by contact, and the motion of the particles modelled particle by particle. To gain acceptable results it was crucial to properly define the boundary conditions as well as the input parameters, as split into two groups: geometrical data and physical properties data. The method was then validated by comparing force vector plots obtained from the computer program, with the corresponding evaluation derived from photoelastic analysis (applied to an assembly of discs by De Josselin et al (1969)). In this example, testing and discrete modelling were performed on a two-dimensional nine disc test, which comprises 9 loosely packed discs in a 3 x 3 matrix. The force vector diagrams obtained through the discrete modelling technique closely resembled those obtained photoelastically. It was concluded



that a discrete element method was a valid tool for research into granular assemblies.

The research undertaken by Cundall and Strack (and others at the time) has served as the inception to the development of using DEM for modelling various granular scenarios. These developments have led to the use of DEM to successfully simulate more complicated boundary and sphere configurations. Walton et al (1999) modelled the dry granular flow of non-spherical particles; for contact detection and contact force calculations, the non-spherical particles were represented as clusters of spheres. Simulation results of the chute flows of soybeans (naturally occurring as ellipsoidal particles) were then presented, after the physical properties of soybeans were obtained through experimentation. Simulation results of the velocity field were then compared to experimental results obtained from chute flow experiments with soybeans. Qualitative agreement was observed (Walton, 1999).

Holt et al (2005) did a comparison between controlled laboratory experiments and discrete particle simulations of the mechanical behaviour of rock. The main purpose of these experiments was to see how well the purely elastic behaviour (as measured by elastic wave velocities) of loaded, uncemented, spherical particles can be simulated by a DEM program (PFC<sup>3D</sup>)<sup>3</sup>. Stress dependent P- and S-wave velocities<sup>4</sup> in uncemented assemblies of glass beads were computed using a Hertzian contact law, and a satisfactory correspondence with laboratory data was obtained. The conclusions drawn from this research were that the test results and the DEM results were in accordance with one another, with the use of DEM leading to a more fundamental insight into rock mechanics.

It has been found that the results, generally, are sensitive to the input variables of the respective model; specifically the rock parameters and the contact model chosen need to replicate reality as closely as possible, with the consideration of sample preparation against the use of published data borne in mind.

### 1.2.7 Developments in DEM Modelling

Currently DEM simulation technology has advanced to a point where large industrial application models may be generated, the principal limiting factor being the computational resources available.

---

<sup>3</sup>PFC<sup>3D</sup> is a DEM package developed and marketed by ITASCA

<sup>4</sup>(P-waves (primary waves) are longitudinal or compressional waves, while S-waves (secondary waves) are transverse or shear waves)

An example of simulated industrial models includes excavators, agricultural equipment, ball mills, conveyor belts, screw conveyors and many other examples of industrial machinery.

Cleary (1999) used DEM to simulate three different particle flow cases; dragline excavators, mixing in tumblers and centrifugal mills. As the focus of the current investigation is rock penetration and excavation, the dragline excavator will be the focal point, although the other cases render it possible to see the range of applications of DEM.

A dragline excavator is a large earth moving machine, used to remove blasted overburden primarily in open cut coal mines. The bucket is suspended on the dragline arm and dragged towards the machine, by shortening the cables on which it is supported. Dragline excavators are extremely expensive to manufacture and maintain; hence it is important to design the machine correctly. Its efficiency depends on various factors - the bucket design, mode of operation, the attachment of cables and the material properties of the overburden. If one or a combination of these factors is not properly accounted for it drastically inhibits the efficacy of the machine. Cleary (1999) examined the variation of drag, load and stability of the bucket with a change in shape distributions of the rock being excavated. In a previous paper (Cleary, 1998), DEM simulations of dragline filling were used to show differences caused by the shape of the bucket. The particle micro-structure and the density of the particles were also shown to have a significant effect on bucket stability.

The above investigation used a standard bucket, as manufactured by ESCO, with irregular particles shapes to evaluate the effect of particles shapes on the bucket performance. The bucket was 5 m long and was dragged up a slope at a speed of 1.75m/s. Figure 1.9 illustrates the simulated model of the dragline.

The blasted overburden was modelled as super-quadric particles with diameters uniformly distributed between 10 cm and 30 cm. Two critical particle shape parameters were thought to have the most significant effect on particle microstructure and hence its ability to flow into the bucket - aspect ratio and blockiness. These were changed independently, and together to understand their effect both on particle microstructure and on the bucket filling process. It was discovered that the blockiness of the material was found to “significantly affect the shear strength of the particle microstructure and increasing blockiness caused the bucket fill rates and bucket stability to decrease” (Cleary, 1999). Whilst it was found that the effects of aspect ratio were slightly less obvious, very small deviations from symmetry improved the flow. However, increased elongation reduced its

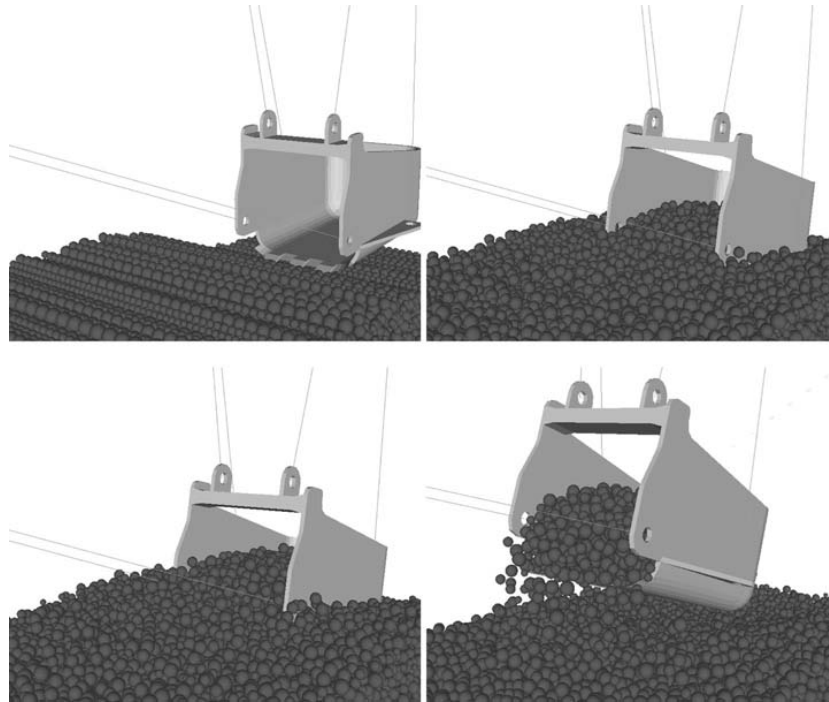


Figure 1.9: A dragline bucket (Cleary, 1999).

flowability and increased fill times. This investigation was a purely numerical study and did not take into account any test with life-size or scale models of dragline excavators. Although this is a significant step in understanding the effects of particle shape on dragline bucket efficiency it is necessary to validate numerical models with controlled laboratory experiments.

Coetzee (2009) produced a paper on discrete element parameter calibration and the modelling of dragline bucket filling. A scale model was produced in the lab and a numerical simulation was then performed, the results from both were then compared in order to validate the DEM results.

A 1:18 scale model of a 61 m<sup>3</sup> dragline bucket was produced. A ‘drag bed’ was designed with means of attaching sensors, and placing in an inclined position so that different drag angles could be observed. Various pieces of instrumentation were attached to the bucket, including a linear variable differential transducer (used to measure speed), and various load cells used to measure the drag force on each cable (there were three to mimic the motion of a full scale dragline). Each experiment was repeated three times (for repeatability), and bucket position, orientation and drag force were recorded for each test.

An exact replica of the scale rig was modelled in the software package PFC<sup>3D</sup>. In order to emulate true conditions, various material parameters including the coefficient of static and rolling friction

and coefficient of restitution were determined (as described in section 1.2.5). They did not take into account scaling, as the intent was to correlate a physical model with numerical results.

The results showed that DEM accurately predicted bucket orientation, and drag force during the first third of the drag distance, thereafter the results deviated slightly. This paper illustrates the usefulness of DEM in describing the effects of various parameters on excavation and that they can be modelled with relative accuracy in commercial DEM codes. The current investigation will be approached in the same way as Coetzee (2009), with a scale model of the Clamshell Mucker being produced, but corroborative modelling then being performed in EDEM<sup>5</sup> rather than PFC<sup>3D</sup>. The focus will be to obtain force correlations between the numerical and small-scale physical models, so that the numerical model could potentially thereafter be used to predict the behaviour of a full-scale Clamshell Mucker.

---

<sup>5</sup>EDEM is a commercial DEM package developed and marketed by DEM Solutions

## 1.3 Objectives

The aim of the research was to develop a scaled experimental replica of the *Clamshell Mucker* and compare its performance, over a range of operating parameters, with those yielded by numerical simulations. If successful this would validate simulation as a tool for optimizing the design and operation of full-scale machines. Four key components required to achieve these aims are as follows:

1. Develop a scaled experimental rig of the Clamshell Mucker to embody an appropriate range of geometrical and operating parameters.
2. Test the scale Clamshell Mucker with hard plastic balls and 13 mm gauge decomposed granite stone, measuring actuation force and position of the bucket jaws. Test parameters include:- initial distance from the surface, angular closing velocity of the buckets, angle of penetration and proximity to the boundaries.
3. Create DEM models of the experimental system to simulate penetration in hard plastic spheres and 13 mm gauge decomposed granite stone (irregularly shaped).
4. Compare outputs of the computer model with experimental measurements and analyze reasons for close correlation and large variations.

# Chapter 2

## Development of Test Facility

This part of the dissertation covers the development of the experimental facilities employed to obtain the required data.

### 2.1 Preliminary Design Considerations

The following sections illustrate the design process and the final design concept.

#### 2.1.1 Design Process

From the outset it was recognized that the broad purpose of laboratory scale testing would be to predict the performance of the full scale system. This can be achieved by one of two ways:

Firstly, data achieved at laboratory scale could be combined with a fundamental scaling analysis to predict full scale operational function. The alternative is to use laboratory modelling to validate a numerical (DEM) model, that could thereafter be used with confidence at a much larger scale. On the basis that there are no general scaling laws for granular flows (Cleary, 1998), it was decided that the latter approach was the most appropriate.

The conceptual design of the rig was carried out as a component of a 2009/2010 vacation work project, performed by Mr Nicolas Sim, a third year mechanical engineering student in the School

of Mechanical, Industrial and Aeronautical Engineering at the University of the Witwatersrand. The objective of the work was to establish an appropriate scale size based on the geometry of the full-scale Clamshell Mucker unit, as well as investigate and propose different conceptual ideas for the operating mechanism.

On the basis of practicality (size and cost constraints), a 1:6 laboratory model was deemed the largest that could be implemented.

Figure 2.1 shows this initial concept, upon which the final design was based. The design was based on the existing clamshell mucker lashing unit. It had clamshell jaws which could be opened and closed, as well as an ability to enter and exit the granular material, or slew to the side to enter the muck pile from an angle.

It was initially unclear to as what actuation system should be selected for the experimental rig. There were three choices; pneumatics, hydraulics or the use of power screws.

Pneumatics were considered initially, based on the fact that the full size Clamshell Mucker uses pneumatics as its method of actuation, and the relative cheapness of the various physical components. This option was eventually discounted because it was necessary to operate the system at selected constant actuation speeds. The compressibility of the flow medium would have required a complex and expensive measurement system and specialized control valves to achieve this.

A power-screw was also considered, as it would afford the operator a high level of control: however it was discarded as an option because of its high costs, the dirty environment it would be operating in and the poor resolution of force measurement that it offers.

The hydraulic actuation system was eventually selected as the most appropriate way to proceed. Such systems afford the operator good control of flow rate - and hence actuator velocity - while the hydraulic pressures provide a close correlation with forces exerted by the actuators.

### **2.1.2 Geometry of Test Facility; Force and Displacement Relationships**

Prior to selecting final geometric dimensions for the clamshell design it was necessary to establish the force and displacement relationships (during a typical work cycle). The force and displacement

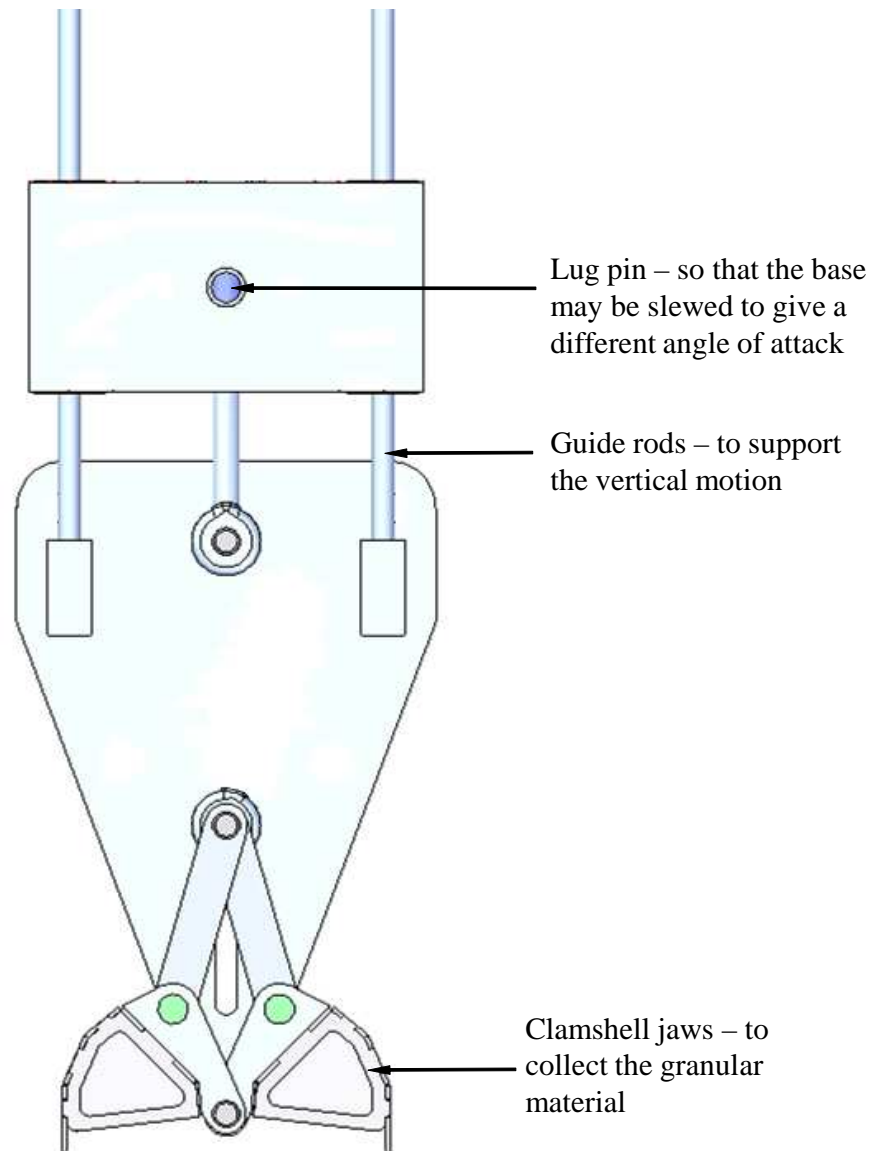


Figure 2.1: Design concept for testing facility.

relationships were resolved using static mechanics analysis.

The relationship between torque on the bucket about its pivotal point and the hydraulic pressure needed to be established. There were two reasons for this: firstly the hydraulic cylinders had to be sized; secondly during final experimentation it would be required to establish the magnitude of the torque about the pivot point, using pressures obtained from the hydraulic cylinder, so as to correlate with torques determined in DEM modelling.

In the former case, the torque is assumed to be  $F_{eff}\ell$ , where  $F_{eff}$  is conservatively assumed to be the maximum force measured during preliminary experimentation (see Section 2.1.3). For



the latter case torque is retained as the primary output, consistent with the outputs of the DEM program. In this instance, determination of torque requires inputs of both hydraulic pressure and actuator angle ( $\theta$ ), that is inferred from the measured bucket angle ( $\gamma$ ). The analysis that follows determines the relationship  $T = f(p, \theta)$ .

Figure 2.2 illustrates the primary external forces evident in the system.

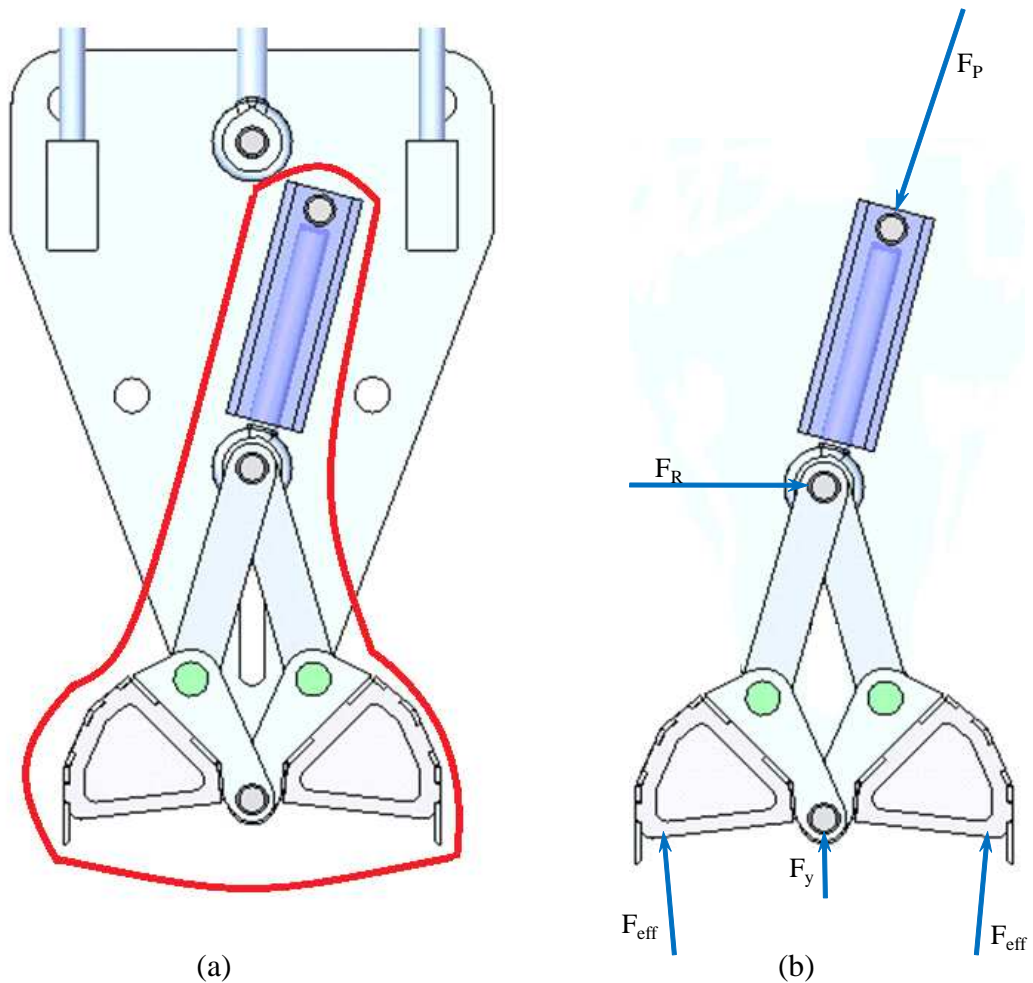


Figure 2.2: Free body diagram of forces in the bucket and hydraulic actuator.

Appendix A contains the formulated relationships used to determine the torque on the bucket as a function of actuator pressure and angle, and actuator angle as a function of bucket angle. This results in eight non-linear simultaneous equations which are solved in Engineering Equation Solver (EES)(the formatted equations may be found in Appendix A). The inputs are the pressure in the hydraulic cylinder and the bucket angle, and the output is the torque required to close the bucket.

### 2.1.3 Initial Experimentation - Hydraulic Cylinder Capacities

There are no standard ways of determining the forces required to penetrate irregular objects into granular material. Therefore it was difficult to estimate on an analytical basis the approximate hydraulic cylinder size required to ensure the buckets would penetrate the granular bed. Accordingly, it was deemed necessary to conduct preliminary experimentation for this purpose.

A brief description of the method for determining the various hydraulic cylinder parameters (separate from the main experimentation) is as follows (a comprehensive description of this method is provided in Appendix B):

A section of channel iron of dimension  $100 \text{ mm} \times 50 \text{ mm} \times 7 \text{ mm}$  was used to vertically penetrate a granular bed using a Schenk hydraulic press, during which the maximum force required to penetrate the material was recorded at various velocities for a constant depth of penetration. Thereafter, the maximum force was used in conjunction with the force relationships in Section 2.1.2 to calculate the required cylinder capacity. This test was conducted for four different descent velocities; 2 mm/s, 20 mm/s, 40 mm/s and 80 mm/s.

Table 2.1 show the maximum forces for each of the various descent speeds, while Appendix B gives all of the data that were recorded.

Table 2.1: Values of maximum force readings for various penetration velocities

Maximum Force Reading for individual Tests								
Descent Velocity (mm/s)	Test 1 (kN)	Test 2 (kN)	Test 3 (kN)	Test 4 (kN)	Test 5 (kN)	Test 6 (kN)	Test 7 (kN)	Average Maximum Value
2	3.779	4.120	4.426	4.800	4.719	2.556	3.109	3.930
20	4.476	3.505	2.825	1.947	3.268	2.412	3.004	3.007
40	2.319	2.960	2.508	3.161	2.900	2.988	2.781	2.806
80	2.020	2.781	1.952	4.334	2.215	2.018	2.514	2.553

It can be seen from Table 2.1 that the average maximum force decreases as the velocity of penetration increases. At 2 mm/s the average maximum penetration force is approximately 3.9 kN, decreasing in magnitude with increasing penetration speeds, to about 2.5 kN. The maximum penetration force recorded was 4.8 kN.

On the basis of this preliminary experimentation it was concluded that a maximum penetration force ( $F_{eff}$ ) of 4.8 kN was an appropriate basis for specifying actuator capacity. From equations (7.18) and (7.6) in Appendix A this corresponds to an actuator force of 9.2 kN. A standard cylinder size of diameter 50.8 mm was chosen in combination with a relatively low operating pressure of 6 MPa - giving a maximum force of 12.5 kN, and hence a factor of safety of 1.35. The actuators were specified and the hydraulic circuit subsequently designed using this maximum force value as a guideline.

## 2.2 Design of the Experimental Facility

It was deemed that the most appropriate mechanism for simulating the Clamshell Mucker operation was a four bar sliding mechanism, with a clamshell digging arrangement at its end. Both the sliding function and the operation of the clamshell arrangement would be operated and controlled by hydraulic cylinders. Figures 2.3 and 2.4 show a schematic of the scaled Clamshell Mucker rig and a photographic illustration respectively.

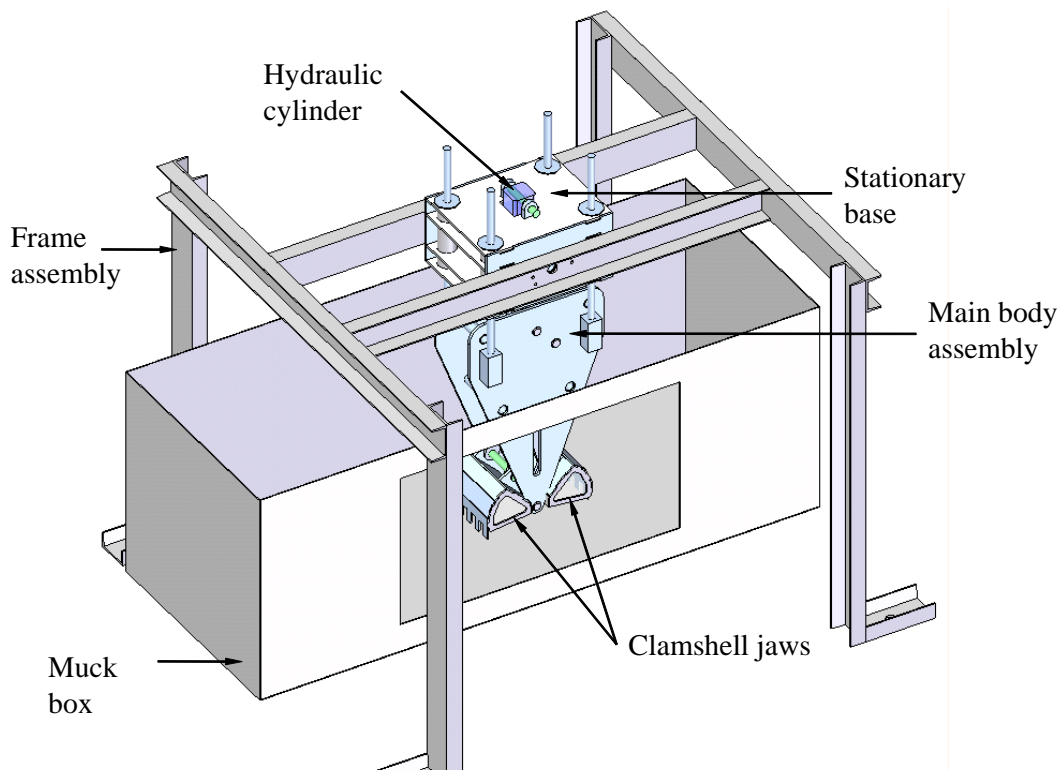


Figure 2.3: Schematic of experimental rig.

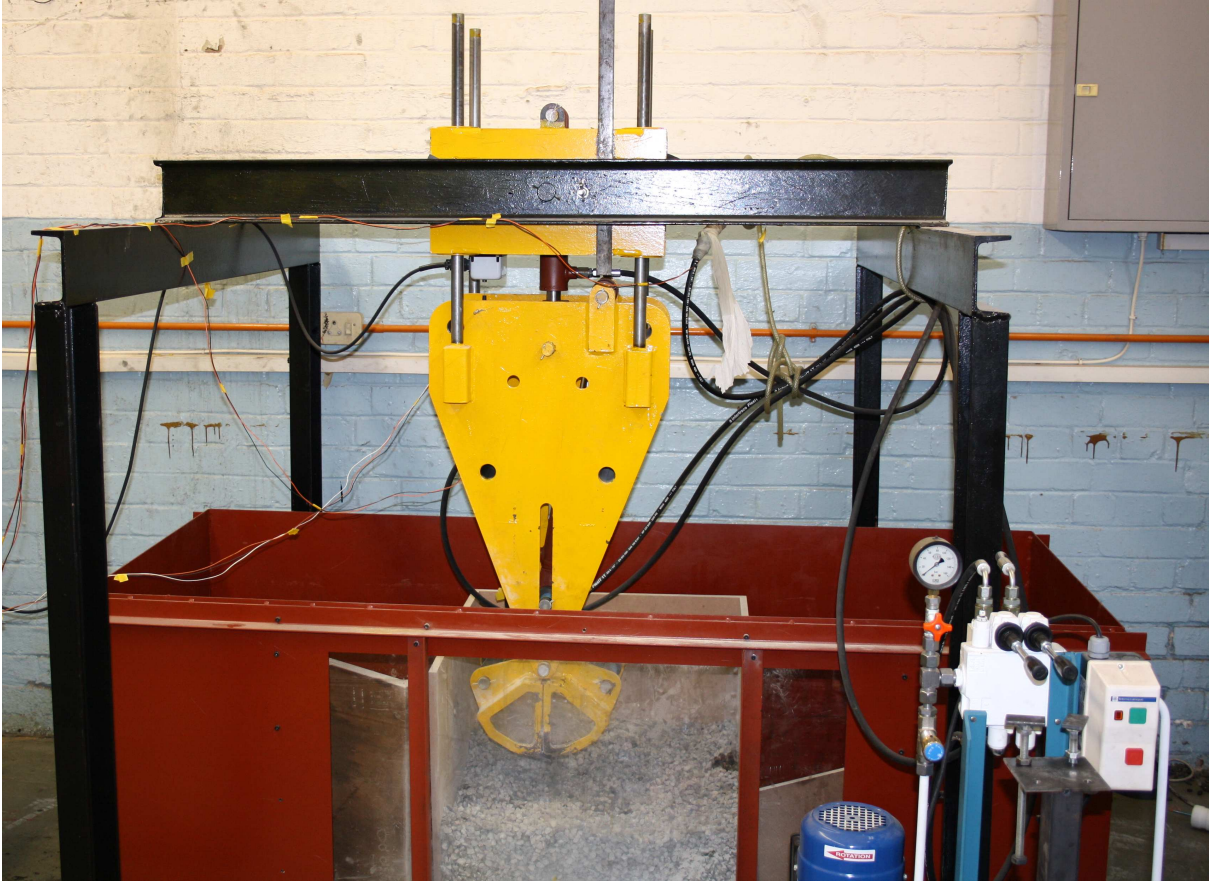


Figure 2.4: Photograph of experimental rig.

The rig comprises a frame which supports the primary assembly. The primary assembly consists of three parts; a stationary base, the main body assembly and the hydraulic actuation system. A muck box is positioned under the primary assembly, which forms the reservoir for the respective materials to be used during testing. All of these components are illustrated in Figure 2.3. A brief description of each of the rig components is given in the subsections below, while detailed explanations of each component may be found in Appendix C. Technical drawings for the individual components may be found in Appendix G.

### 2.2.1 Frame, Primary Assembly and Muck box

The stationary base (see Figure 7.10) forms the fixed foundation of the experimental rig, connected to the support frame (shown in Figure 7.15) by means of two lug pins. These allow the base to articulate to defined angular positions, providing different angles of attack.

The main body forms the base for the operational mechanisms of the rig; i.e. it contains the clamshell jaws and the attachment points for the hydraulic cylinders. Four guide rods, attached to the main body assembly, extended through the stationary base, keeping the bucket vertically aligned during the digging motion, and control its path. It is actuated vertically up and down by means of a hydraulic actuator connected to the stationary base (see Figure 7.12). Attached to the main body, by means of pins and linkages are the clamshell jaws. These are opened and closed by means of a second hydraulic actuator.

The muck box was designed taking two factors into consideration: firstly the digging action needed to be visible and secondly the box had to be large enough so that boundary effects did not adversely affect the results. The first consideration was achieved by installing a portal or window into the front of the muck box, which would allow for visual observations of particle flow. The size of the box was three times the width, height and length of the bucket, based on Coetzee (2009)

The frame of the rig was designed so that stability and maximizing the visibility were primary considerations (see Figure 7.15). It comprises twelve lengths of material, making up the legs, feet, cross members and the support structures, and was designed to be as simple and cost effective as possible.

### **2.2.2 Hydraulic Circuit**

The forces established in Section 2.1.3 were used as a basis for sizing the hydraulic actuators and the other components of the hydraulic circuit.

Hydraulics were purchased through Ernest Lowe Ltd and comprised the following: two push-pull hydraulic cylinders and a power pack (with its various attachments; an oil reservoir, oil gauge, a 0.75 kW electric motor, a positive displacement pump of capacity 5.5 l/min, a dual lever valve and a safety valve that can be set to 6 MPA). Appendix C contains a schematic of the hydraulic circuit (Figure 7.16) and the associated parts list (Table 7.2).

### **2.2.3 Instrumentation**

The various items of instrumentation were selected, based on the required output data and the requisite range of measurements. Figure 2.5 shows the experimental model and the various elements that required measurement.

It was recognized that actuator pressures and extensions were required as a function of time, from which forces on the bucket and position of the bucket could be inferred during the digging cycle. It was decided that an appropriate aim in terms of the current investigation would be to measure the forces and obtain the position at which the force is maximised during a typical digging cycle. Therefore the data that was required was a position versus force, so that it would be possible to identify where within the digging cycle the most strain is put on the system, and to understand how the peak force relates to the digging and filling of the bucket. Pressure transducers were used to determine the cylinder forces and infer digging forces.

A linear potentiometer was selected to measure the linear position (depth of penetration) of the bucket, while an angular potentiometer was used to measure the angle of the bucket during the digging motion. A Data Acquisition System (DAQ) was used to capture data during testing.

The wiring diagrams for the different pieces of instrumentation may be found in Appendix C.

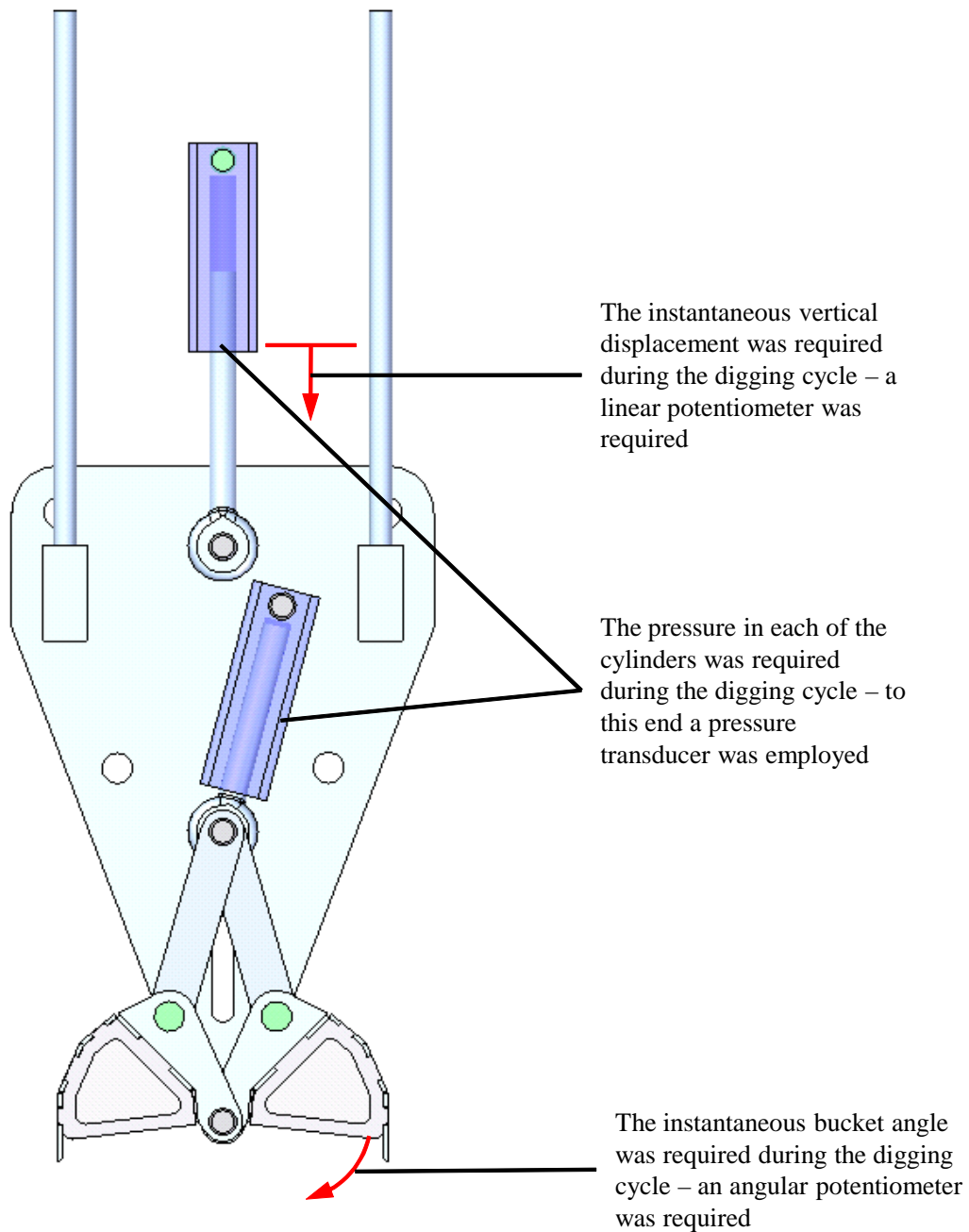


Figure 2.5: Schematic of experimental equipment and required instrumentation.

### 2.2.4 Velocity Control Mechanism

To control the angular velocity of the bucket a simple adjustable stop was added to the proportional control valve which controls the bucket actuator cylinder. This adjustable stop was preset between tests and the angular velocity of the bucket measured in free space.

# Chapter 3

## Numerical Modelling

The numerical modelling of the Clamshell Mucker in operation was conducted using the Discrete Element Methods (DEM) package EDEM v2.2.0.<sup>1</sup> As outlined in Sections 1.2.4 and 1.2.5 various physical parameters were required for the DEM model. These will be discussed in more detail here before the DEM modelling is explained.

DEM modelling was performed for both plastic balls and 13 mm gauge decomposed granite stone. The current section relates exclusively to the rock particle simulations.

### 3.1 Physical Parameters

As detailed in section 1.2.5 the DEM model requires accurate physical parameters, such as static and rolling friction, and coefficient of restitution. These need to be determined for all the particle and surface type combinations.

In order to determine these parameters suitable specimens are required. For rolling friction and the coefficient of restitution tests the ideal particle shape is spherical. However, no spherical particles of 13 mm decomposed granite were found, and attempts to grind a particle into a roughly spherical

---

<sup>1</sup>Each run for a specified set of parameters took approximately 10 to 12 days (of 24 hours per day) to complete on a personal computer with a state-of-the art Intel i7 processor with 8 Gb of memory. A total of 7 parametric combinations were explored, equating to about 70 to 80 days of final processing, excluding about 5 preliminary trial runs that amounted to a minimum of 50 to 60 days.



shape were not successful. This yielded variable results for the rolling friction and coefficient of restitution parameters. The average results for the 15 tests can be found in Table 3.1 and compared with comparative values obtained from the literature (the square brackets in the tables are representative of references). Details of the tests may be found in Appendix D.

For the static friction tests 15 tests were conducted as per the methodology given in Section 1.2.5, where decomposed granite particles were placed either on steel or polycarbonate plates, which were angled until the particles began to slide. The results of the test can be seen in Table 3.1, together with comparative values from literature, and more details of the tests can be found in Appendix D.

Table 3.1: Comparisons between measured physical parameters and published values.

Parameter	Interaction					
	granite-granite		granite-steel		granite-polycarbonate	
	Published	Experiment	Published	Experiment	Published	Experiment
Coefficient of restitution	0.835 (Durda, 2010)	0.32±0.12	0.81 (Imre, 2008)	0.55±0.21	0.65 (Constantinides, 2007)	0.42±0.15
Coefficient of rolling friction	0.04 (Beardmore, 2010)	0.6±0.1	0.0021 (Beardmore, 2010)	0.24±0.14	0.001 (Beardmore, 2010)	0.14±0.07
Coefficient of static friction	0.56 (Beardmore, 2010)	0.54±0.05	0.38 (Beardmore, 2010)	0.39±0.05	0.36 (Beardmore, 2010)	0.34±0.05

From Table 3.1 it is seen that in the cases of coefficient of rolling friction and restitution, the measured experimental values deviate significantly from those found in literature. In addition to this, individual test results were also highly variable - for these reasons published data results were used instead of measured experimental values. A sensitivity analysis was subsequently performed to evaluate the effect these input parameters have on DEM modelling, this can be seen in Section 3.1.1.

### 3.1.1 Sensitivity Analysis

The differences between the measured and published data values for the particle-particle and particle-boundary parameters in Table 3.1 rendered it necessary to perform a sensitivity analysis, that would assist in gauging the effects of these parameters on the DEM simulations. This was achieved by creating a simple DEM model consisting of a blunt steel object penetrating a bed of particles. In turn each of the parameters considered above (coefficients of static friction, rolling friction and restitution) were altered by +30%, ±50% and -17.3%<sup>2</sup> respectively, to ascer-

<sup>2</sup>The experimental value for the coefficient of static friction correlated well with values obtained from the literature; hence only one change was implemented. Large deviations were observed between the published and measured values

tain their effect on the total force experienced by the model. Only a single parameter was altered per simulation, a detailed description of the sensitivity analysis is provided in Appendix D.

Figure 3.1 shows the variation of force with time for each of the cases that were considered.

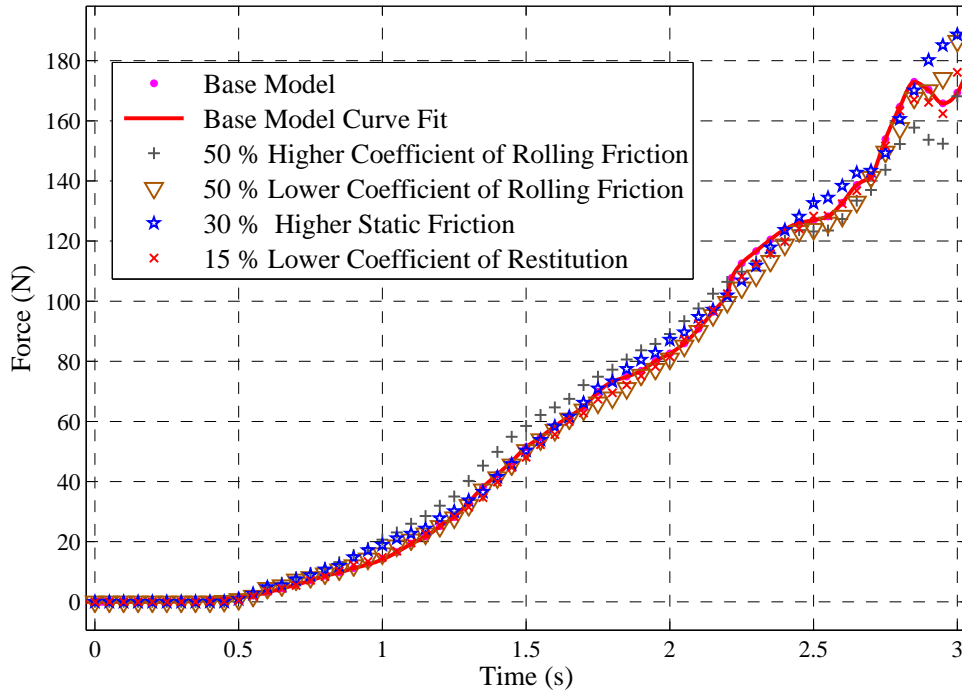


Figure 3.1: Sensitivity analysis: penetrating force as a function of varying physical parameters (coefficient of rolling friction and restitution and static friction)

It is seen that the percentage changes in all of the parameter values relative to the base system lead to percentage deviations of force of between 3 and 10 percent, especially at about 3 s. It is assumed that as the blunt object approaches this point the particles start to become congested, hence the stick-slip phenomenon of the material becomes more pronounced, increasing its random behaviour. These small percentage changes indicate that using published data will not lead to significant errors in the DEM simulations.

EDEM also requires the general mechanical properties which have been tabulated in Table 3.2. References are indicated in square brackets alongside each value.

of rolling friction coefficient. Hence a large span of  $\pm 50\%$  was explored. The original coefficient of restitution of 0.835 was adjudged to be at the high end of expected values and hence only a negative adjustment was made.

Table 3.2: Global Physics Settings of the testing materials.

Global Physics Settings			
General Properties			
Parameter	13mm Stone <small>(General Properties)</small>	Steel <small>[Engineering Toolbox (N.D. A&amp;B)]</small>	Polycarbonate <small>[Engineering Toolbox (N.D. A&amp;B)]</small>
Gravity (m.s <sup>-2</sup> )	-9.81	-9.81	-9.81
Poisson' s Ratio	0.25	0.3	0.36
Shear Modulus (GPa)	28	70	2.3
Density (kg.m <sup>-3</sup> )	2700	7800	1200

## 3.2 DEM Model Development

Within EDEM simulation, model development is broken up into four distinct stages: definition of global physics settings, development of the particle, construction of the model geometry and creation of the collection of particles or the *particle factory*. Each of these stages is described in the subsections which follow.

On the basis of the arguments in Section 1.2.4 relating to the contact models the Hertz-Mindlin contact model was selected.

Global Physics Settings entail the incorporation of the physical properties into the DEM modeller. The values used in the DEM model are tabulated in Table 3.1 for the contact model properties and in Table 3.2 for general physical parameters.

### 3.2.1 Development of the Particles

In order to represent typical decomposed granite particles which are not spherical, but more elongated with defined edges it was decided to develop a custom particle.

The development of the particle was a two part process: initially a Solid Edge model of a “standard” granular sample shape was generated as a template. Thereafter, spherical particles were used to fill the volume of the template and hence recreate the basic shape of the stone. This was done using two ‘common’ sample shapes of the decomposed granite, the templates of which are shown in Figure 3.2, with the resultant particle shapes in Figure 3.3. When considering the geometry of the particle it was essential to consider two issues; the first being obtaining a particle shape as closely as possible (although the nature of the particles is random and the particle selected would be a typical shape which would represent all the particles), the second is to achieve this using the minimum number of particles - to decrease computation time.

Within the context of the current investigation the shape of the particles is important, so as to attempt to meaningfully recreate interlocking, jamming and packing characteristics. However, the required accuracy is not such that exact replicas of the particle shapes are vital to success. While an exact replica could be produced by using many small spheres to make up each individual granite particle, such a measure would impracticably increase the computation time.

After the shapes of the rock have been defined and created, the physical properties of the rock are used (see Table 3.2) in combination with the geometry of the rock, to generate the mass of the individual rock particles (this is important later in the context of the time-step). The particles shown in Figures 3.2 and 3.3 represent the two different particles used in the simulations.

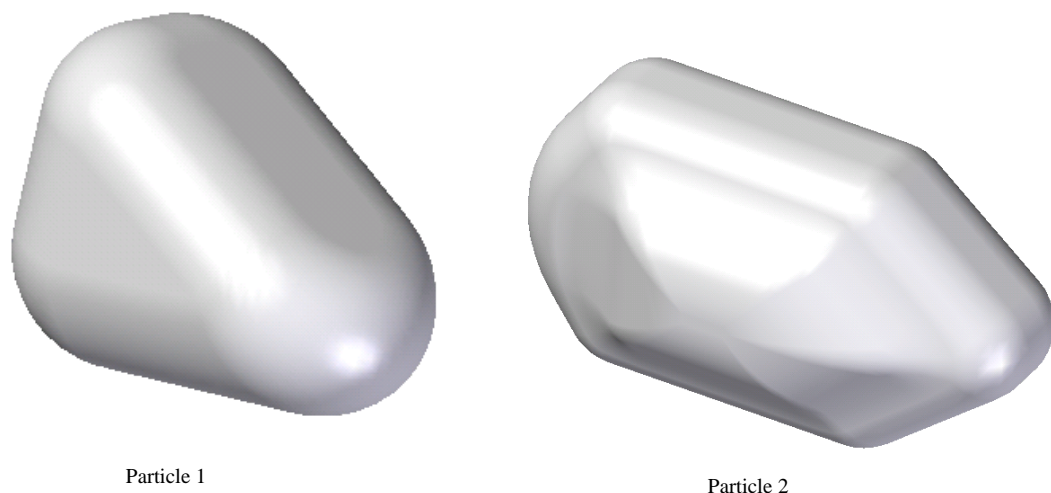


Figure 3.2: A Solid Edge template of the decomposed granite

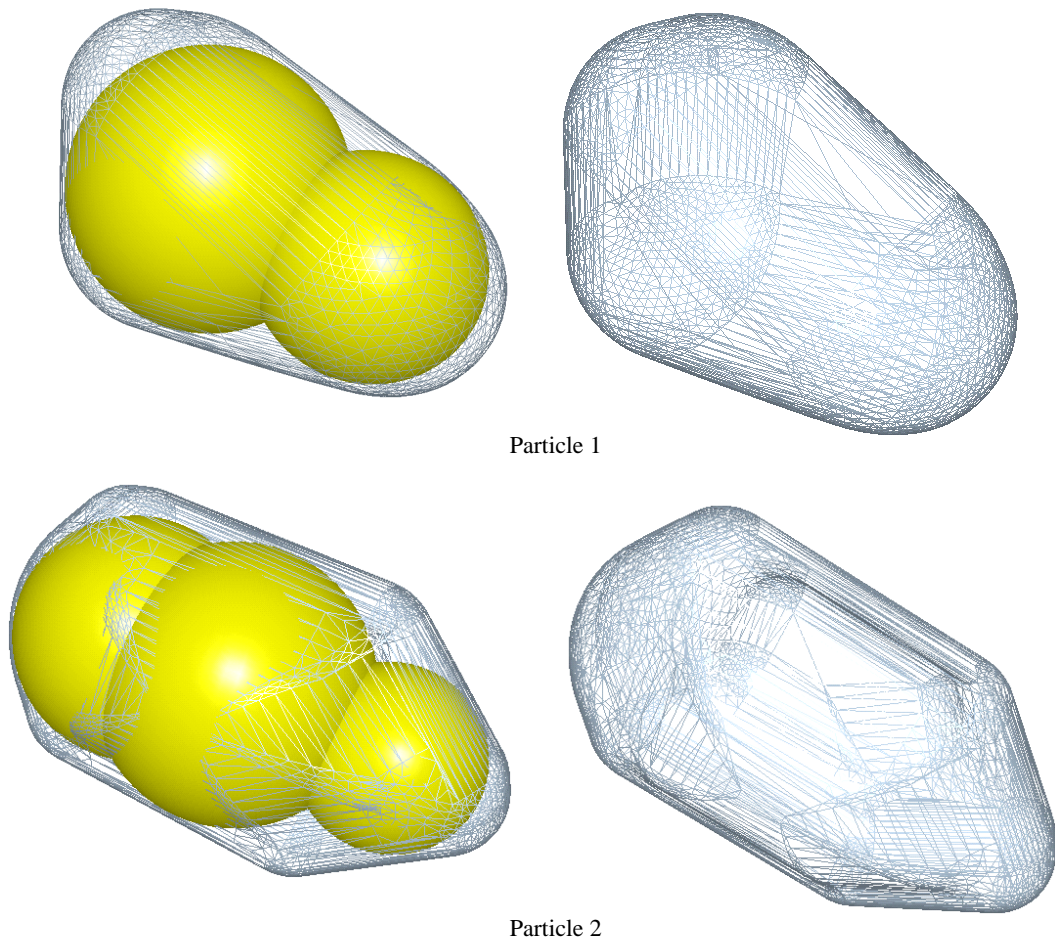


Figure 3.3: Resultant spherical particle configurations for final particle shapes

### 3.2.2 Model Geometry

The geometry employed in the computer model was a geometrical replica of the actual testing apparatus. However, only the clamshell jaws and reservoir were simulated in EDEM, rather than the entire experimental rig. The clamshell jaws and reservoir were created in Solid Edge and thereafter exported into EDEM as .stl files. The container material and the clamshell jaws were set to have the same properties as the steel, while the front window of the container was defined as having the same properties as polycarbonate.

Figure 3.4 illustrates the geometry as defined in the EDEM program. In order to improve simulation times, slightly simplified geometries were used relative to those existing in practice. Thus, the reservoir was defined as being a simple box with five sides, four of which were composed of steel and the last side (in front) being composed of polycarbonate. Each jaw was modelled as a single component rather than complex assemblies consisting of many different sections.

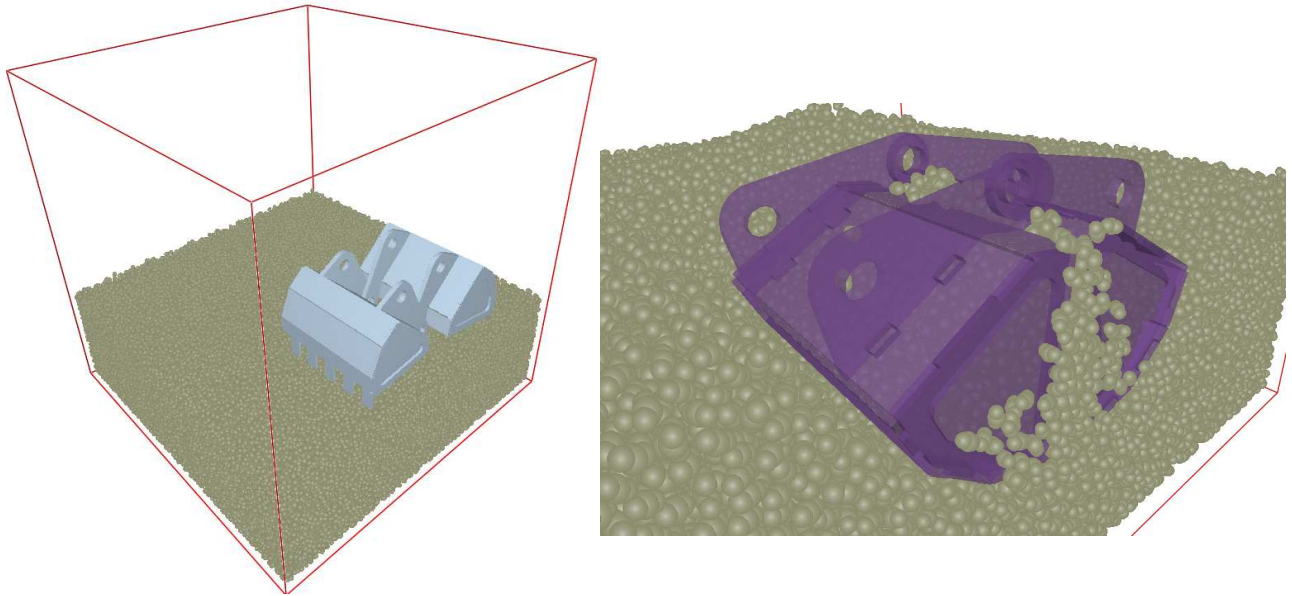


Figure 3.4: Geometry as defined in the EDEM programme

The kinematic motion and velocities of the clamshell jaws were also defined in this section. These were embodied in specific testing parameters such as pre-positioning of the buckets above the material and bucket closing velocities thereafter.

### 3.2.3 Particle factory Configuration

Granular material fields in EDEM models are generated through the use of a tool called a *particle factory*. The particle factory is essentially a virtual area defining a region in which the particles are created. A primary concern when generating a particle field is to create a particle stream that is representative of the system in reality, particularly in the context of the packing. Hence the user is able to define all of the factory characteristics, including:- particle generation [i.e. dynamic (particles are replenished at a specified rate) or static (a fixed number of particles to fill a volume) generation], the generation rate (mass or number generated per second) and the initial particle parameters (including their initial velocity, size distribution, etc).

For the current situation it was necessary to generate a contained bed of loosely, randomly packed rock. Particles are generated in one of two ways, either statically or dynamically. In static generation the volume of the reservoir is filled with particles, spaced randomly and inflated from their location until particles begin to touch or reach their defined size. This results in artificial voids

which collapse at the start of the simulation and do not accurately represent reality. The second method is dynamic generation, that allows generated particles to fall from a small height before coming to rest in a random, packed configuration (Thorensson, 2010). The method chosen to achieve this was to define the particle factory as a thin plate, with the same dimensions as the floor of the reservoir and situated 150 mm from the bottom. The factory was then defined to ascend at a rate of 250 mm/s whilst generating particles that fall under the action of gravity for a period of 1.5 s. This would allow particle generation (i.e. the position of the factory) to be slightly above the particle field at all times. The factory was defined to generate 500 kg in particle weight (roughly the same weight used during the experimentation), at a rate of 376 kg/s.

Thereafter the initial particle parameters are defined. The type of particle was described as binary, corresponding to which two particle shapes were randomly generated during the production of particles - see Section 3.2.1. The size distribution was set to a normal distribution with a standard deviation of 5%, corresponding approximately to the observed variability of the 13 mm gauge stone. Particle positions were set to random packing, as opposed to BCC or FCC packing. Initial velocities were set to zero (i.e. they would start from rest and accelerate downwards due to gravity). Particle orientation was also set to random. Lastly the initial angular velocity was set to zero.

### **3.2.4 Simulation Parameters**

The simulation parameters describe the setting of the model, that affect accuracy and duration during the running of the simulation. The program chooses a default time step (the Rayleigh time step) based on the size of the particles and their modulus of rigidity. The time step for each run was set to be 18% of the calculated Rayleigh time step - as large as possible to reduce computational time, whilst not causing solution instability. Additionally, the grid size was set to its lowest possible value without exceeding a grid cell number of 1 000 000. This limit was recommended to maintain solution accuracy without needlessly wasting computation time (Thorensson, 2010).

# Chapter 4

## Experimentation

The experimentation forming the basis of the current investigation was that performed with the scaled Clamshell Mucker rig. There were two phases of experimentation; the first conducted with hard plastic balls and the second was with 19 mm decomposed granite rock. The experimentation was performed in order to validate the results of the numerical modelling, and understand the behaviour of the rock/mucker interaction.

### 4.1 Calibration and Actuator Base Loading

Before the commencement of experimentation it was necessary to calibrate various components of the system, including the angular potentiometer and the control valve (the pressure transducers and linear potentiometer came pre-calibrated with manufacturer' data sheets). In addition it was necessary to determine the hydraulic pressures required to actuate the system in free air, as friction in the cylinder and sliding joints would result in some reactive forces (base loads) which would need to be taken into account. A full description of the calibration procedure and the method by which the base loads on the cylinder were obtained is discussed in Appendix E.



## 4.2 Experimental Method

Various experimental parameters were tested for two different materials: hard plastic balls and thereafter 13 mm decomposed granite stone. The hard plastic balls were to be used as a *qualitative* comparison between DEM and physical testing using video comparisons. The 13 mm decomposed granite stone was subsequently used to give a *quantitative* comparison between the torques required to physically penetrate the granular material and the data generated by the DEM programme.

### 4.2.1 Testing Procedure

#### Method

Below is a basic version of the testing procedure followed. It is not specific to any test (as mentioned previously). Figures 4.1 and 4.2 in Section 4.2.3 show a full list of the test parameters.

1. Start the hydraulic power pack and the instrument power packs.
2. Plug the USB DAQ into the computer and the instrument connector into the USB DAQ
3. Turn on the laptop and start the Signal Express©software.
4. While the program is sampling the data generated from the various instrumentation, check to ensure all of the initial readings are correct.
5. Ensure that the main body is fully retracted and the bucket is fully open.
6. Set up the video camera on a tripod in front of the forward boundary.
7. Push record in the software (save the first run of every step as “run 1” then “run 2” etc. As the testing progresses, move to the video camera and push the record button here.
8. Select the vertical cylinder motion control and open it fully in such a way that the entire body assembly moves vertically downwards towards the muck reservoir, until the body assembly no longer moves.

9. Select the control that operates the opening and closing of the bucket (bucket control); open this valve so that the bucket closes and continue until the bucket no longer changes position (the bucket closing velocity is altered by placing the valve stop under the control, limiting the amount the control lever can open the valve).
10. Open the vertical motion control in the opposite direction so as to initiate the retraction of the main body assembly; hold this fully open until it has reached its full extent.
11. Once again use the bucket control, opening it as fully as possible until the bucket has fully opened.
12. Stop the recording of the camera.
13. Select the Stop button in Signal Express.
14. Agitate the stone with a steel bar then level it out to ensure no packing occurs and that the depth for each run remains constant.
15. Repeat steps 6 to 14.

## **Precautions**

Given below are two lists of precautionary measures which were followed whilst performing the experiment. The first list mentions aspects which had implications for accuracy of data, whilst the second refers to points of concern regarding safety.

Operational precautions are as follows:

1. The stone in the muck reservoir must be agitated after each test run. This is done to effectively reset the random particle arrangements to remove any changes - in particular structuring -of the packing arrangements, as well as level out the stone, to ensure that a constant digging depth is maintained for similar setups.
2. Before the commencement of experimentation, all the instrumentation is tested to ensure the individual components are generating suitable readings.

Safety precautions are as follows:

1. Before the commencement of testing, the hydraulic pipes and hydraulic power pack are checked for leaks.
2. Due to the operating mechanism (i.e. the clamshell bucket closing) stone is often crushed, and at times segments of rock are fragmented and propelled in different directions; therefore appropriate eye protection is necessary.
3. The extractor needed to be kept on continuously, to ensure that humidity did not affect operating conditions, and to keep the operator safe from any ailments resulting from this type of environment, such as Legionnaires disease.
4. During experimentation at an altered angle, ensure that all of the bolts holding the apparatus in position are tightened.

#### **4.2.2 Testing Hard Plastic Balls**

Two different sizes of hard plastic balls were combined in a fixed volume ratio (2/3 of 25 mm diameter and 1/3 of 19 mm diameter balls), for which two sets of experiments were performed: a) testing with a 20 mm gap between the jaw tips and the granular material, and b) with the jaw tips making light contact with the surface of the granular material (see Figure 4.1 part (ii) a). For each of the initial jaw tip positions a constant bucket closing velocity of 20 deg/s was used, and the bucket was positioned at the forward wall to achieve good visibility.

#### **4.2.3 Testing 13 mm Decomposed Granite Stone**

A more complete testing regimen was formulated for the 13 mm decomposed granite stone than for the plastic balls. Figure 4.1 illustrates the different testing parameters that were conducted: testing at the different boundaries [Figure 4.1 part (i)], testing at different distances from the surface [Figure 4.1 part (ii) a], testing at different angles of attack [Figure 4.1 part (ii) b] and testing at different bucket closing velocities. The hierarchy of experimentation is described in Figure 4.2. The highest level in the hierarchy is distance from the surface, thereafter the boundary at which

testing occurs and finally, bucket closing velocity. A single boundary (the middle), bucket closing velocity (20 deg/s) and distance from the surface were used for various different angles of attack, where the primary factor was ensuring that a full bucket load was collected for each case. The primary motivation for the testing was a comparison between the torques obtained from physical data and those from the numerical model.

The procedure for each individual test adhered to the same basic pattern, with altered experimental parameters. These parameters are shown in Figure 4.1.

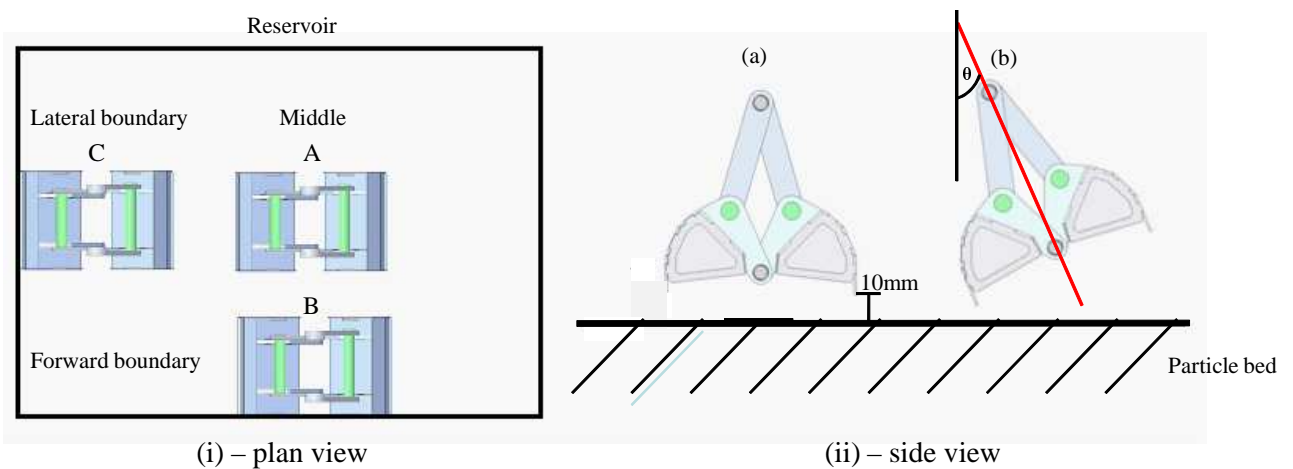


Figure 4.1: Visual illustration of the different testing parameters.

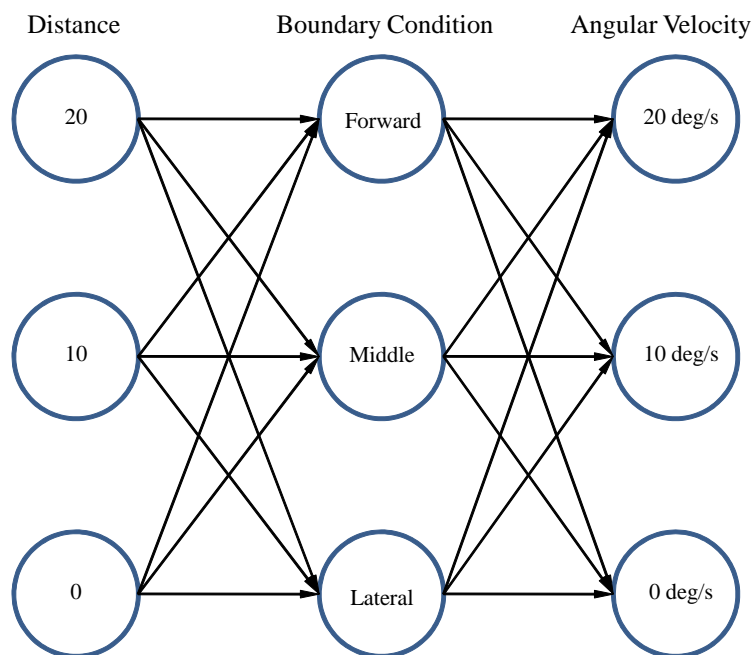


Figure 4.2: Matrix describing the experimental parameter hierarchy.

## 4.3 Observations

### 4.3.1 Hard Plastic Balls

The initial distance of the teeth from the surface was the only parameter changed during the different tests conducted with hard plastic balls, since the resistance of the balls was low and the additional cylinder pressure indistinguishable. Testing was performed at two depths; 30 mm and 0 mm above the granular field respectively. A constant bucket closing velocity of  $20^\circ$  was used for both sets of tests. This was considered to be an appropriate amount of testing to obtain qualitative comparisons between computer predictions and the physical system. Video images of the experiment and DEM comparisons can be seen in Section 5.1.

### 4.3.2 Decomposed Granite Stone

Experiments for the 13 mm decomposed granite stone were conducted with various testing parameters (described in Section 4.2.3). The primary parameter was the starting distance from the surface of the material. At each starting distance (i.e. 20 mm and 10 mm above, and touching the muck pile respectively) the clamshell bucket was operated at the three different boundaries (the forward boundary, the lateral boundary and in the middle of the granular field respectively). Three different bucket closing velocities (20 deg/s, 15 deg/s and 10 deg/s) were tested at each boundary. Thereafter, four different angles of attack of the bucket ( $0^\circ$ ,  $5^\circ$ ,  $15^\circ$  and  $30^\circ$ ) were explored at a constant closing velocity of 20 deg/s in the middle of the material.

For repeatability, tests were performed a number of times. In all cases for a bucket closing velocity of 20 deg/s, the test was repeated ten times, while all the other tests were repeated a minimum of five times. Sample illustrations of raw data are given Figure 4.3. This represents the variation in voltage with time for a bucket closing velocity of 20 deg/s operating in the middle of the granular field, having an initial distance to the surface of 20 mm. The voltages in Figure 4.3 represent the angular position of the bucket and the pressure in the hydraulic cylinder controlling the bucket. A sample table of data and a CD of the rest of the raw data may be found in Appendix F.

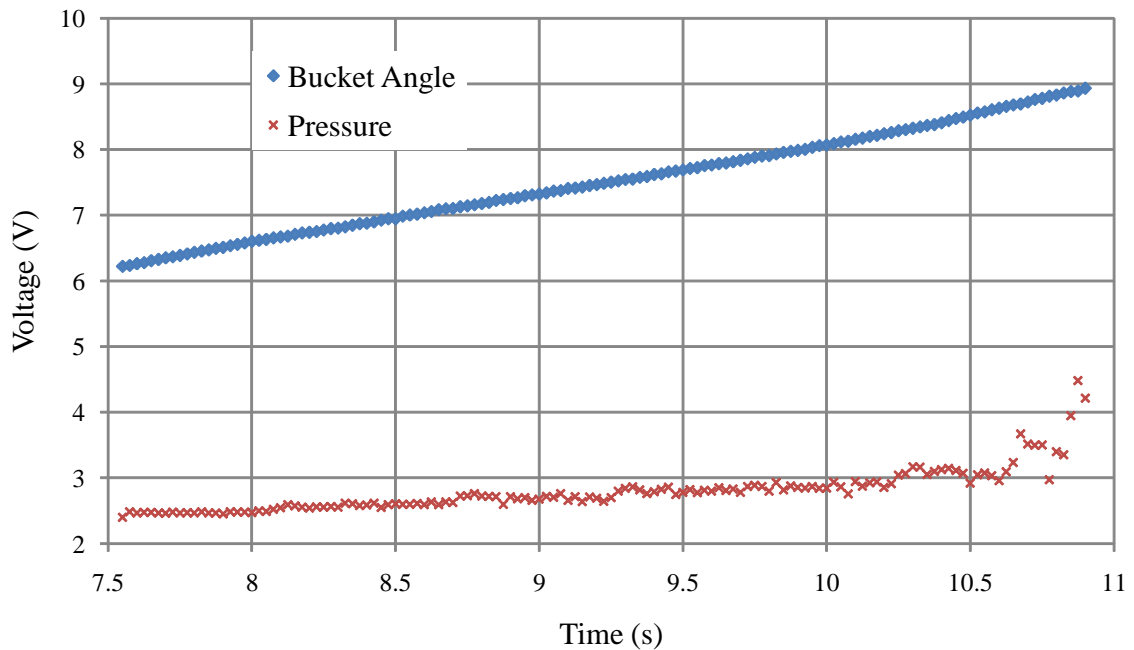


Figure 4.3: Typical variation of voltage with time representing the pressure in the hydraulic cylinder and the angle of the bucket respectively.

During the physical testing a number of general observations were made:

1. At an initial starting distance of 20 mm above the muck, only approximately 80% of the clamshell bucket capacity is reached when the jaws are fully closed.
2. With the teeth starting off touching the muck, the volume of material collected is more than the capacity of the jaws; therefore the jaws cannot close and a proportion of the material falls out as the spike in pressure indicates.
3. When the teeth start off 10 mm above the muck pile the jaws collect approximately the correct amount of material - the buckets are completely filled.
4. At the polycarbonate (forward) boundary the jaws close initially with less impedance. As the process continues the material visibly collects together to form a clump, constrained by the forward boundary.
5. At the lower bucket closing velocities the clumping effects mentioned in the previous point are amplified.
6. At a bucket closing velocity of 10 deg/s the jaws do not fully close, which is instigated by the interlocking and subsequent jamming of the granular material.

## **4.4 Data Processing**

### **4.4.1 Hard Plastic Balls**

An image processing program was written in Matlab, that was used to compare images from the DEM model with video images of the physical model. The DEM and physical videos, showing the flow of the balls, were compared side-to-side on a common screen.

### **4.4.2 Decomposed Granite Stone**

The context of the data analysis that follows was to convert hydraulic pressures to bucket torques and to relate the bucket angles to actuator angles.

A number of steps were required to arrange the data so that meaningful information could be obtained. These are outlined as follows:

The calibration curves for each item of instrumentation were created. For the linear potentiometer and pressure transducers this was done using manufacturers' data sheets, while the angular potentiometer was analyzed (as described in Section 7). Thereafter equations were generated from the linear curves. These provided specific displacements, angular positions and pressure values corresponding to the voltages recorded during testing.

The closing of the bucket during testing was the primary area of focus; therefore the range of readings corresponding to the closing of the bucket (measured using the angular potentiometer) were isolated. Thereafter, the torque required to close the bucket during the motion was ascertained, using equations 7.18 and 7.2 to 7.7 in Appendix A. The Data was smoothed using an un-weighted 5 point moving average.

#### **Calibration Curve Equations**

The raw data extracted during experimentation took the form illustrated in Section 4.3.2. The voltage values are resolved into bucket/vertical actuator pressures, and linear/angular displacements using the following equations respectively:

$$P_1 = 11.315x - 25.246 \quad (4.1)$$

$$P_2 = 11.292x - 25.219 \quad (4.2)$$

$$y = 26.825x - 2.2507 \quad (4.3)$$

$$\gamma = 26.15x - 160.9 \quad (4.4)$$

For the first two equations  $P_1$  and  $P_2$  represent the bucket and vertical actuator pressure (in Pa) respectively; for the latter two,  $y$  and  $\gamma$  represent the linear and angular displacements respectively, and  $x$  represents voltage in all four cases. Sample tables of raw data converted from voltage to pressure and voltage to bucket angle are given in Tables 7.4 and 7.5 respectively, in Appendix F.

### **Inferred Forces and Moments**

The relationships between the moments and angles in the system were established in Section 2.1.2 (with more detailed descriptions in Appendix A). The forces and moments acting on the bucket in the system are calculated using the pressure in the cylinder. A representation of the conversion of pressure into torque is shown in Figure 4.4

Figure 4.4 shows a variation of torque with bucket angle for a bucket closing velocity of 20 deg/s operating in the middle of the granular field, having an initial distance to the surface of 20 mm. Figure 4.4 is representative of all of the data (encapsulating all 10 runs) for this test condition. The red and green lines represent the upper and lower limits for all of the test runs. It is shown that the average variation for all of the test runs was between 5 and 15%, inferring that the tests were reasonably repeatable. Further evidence of this may be found in Appendix F where the upper and lower limits for all other test conditions are shown to have similar variability.



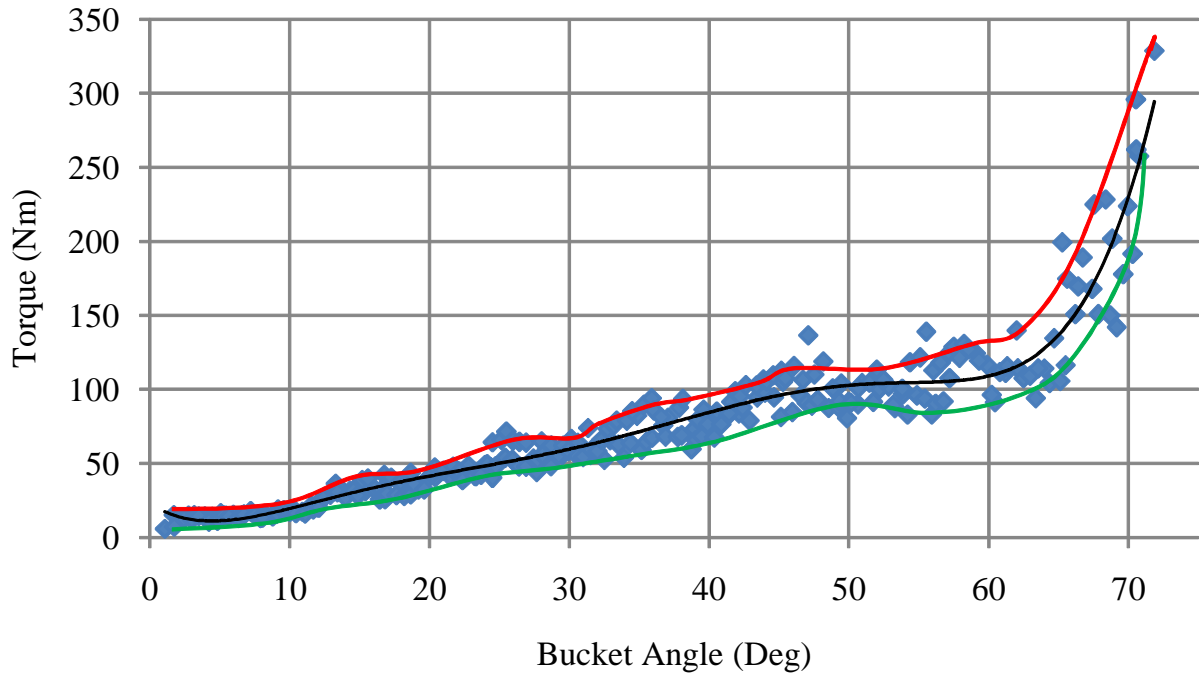


Figure 4.4: Typical variation of torque with bucket angle for a bucket closing velocity of 20 deg/s, in the middle, starting at 20 mm from the surface of the material.

#### 4.4.3 Estimates of Energy Levels

The relative energy levels required to fill the buckets under a variety of operating conditions are of fundamental interest. It was specifically decided to establish the manner in which the required digging energy changes with angle of penetration, because this has a potential impact on the strategy that might be adopted in clearing a muck pile.

For this purpose it is an elementary exercise to show that the energy  $E$  employed to fill the buckets is given by

$$E = \frac{\pi}{180} \int_0^{\Theta_{final}} T d\theta \quad (4.5)$$

where  $\Theta_{final}$  is the angle  $\theta$  at which the buckets have just filled. This is synonymous with the angle at which the bucket stops closing, clearly visible when the voltage output of the angular potentiometer has reached its maximum. For each case a full bucket load was considered.

Energy levels for ten tests were averaged for each angle of penetration.

# Chapter 5

## Results

The current section involves three parts - qualitative results (hard plastic balls), physical testing results (13 mm stone) and their comparison with data generated by the DEM software.

### 5.1 Qualitative Data - Flow Visualization

A visual comparison between material flow in the physical bucket and DEM simulations formed the qualitative component of the study. Figures 5.1 to 5.4 are visual comparisons between video images generated by physical testing and numerical modelling respectively, which show good correlation. These qualitative results will be discussed in more detail in Section 6.1.

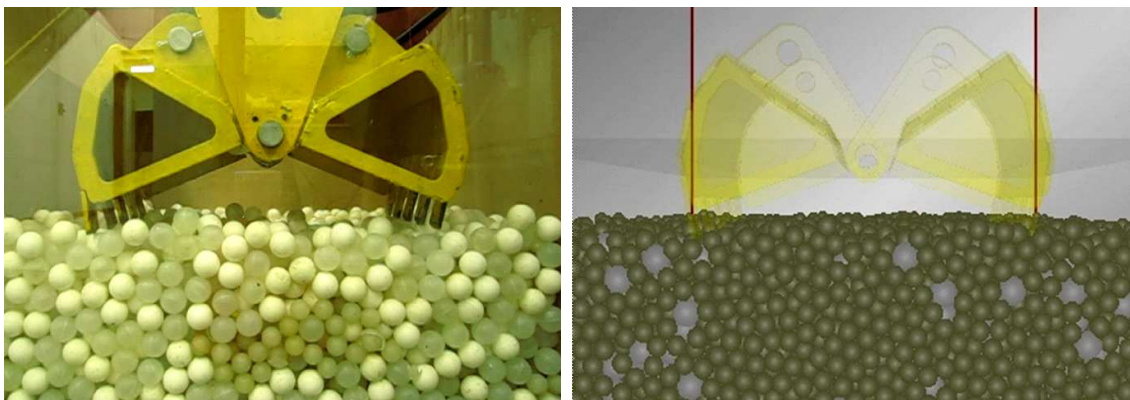


Figure 5.1: Motion comparison of the bucket part 1.

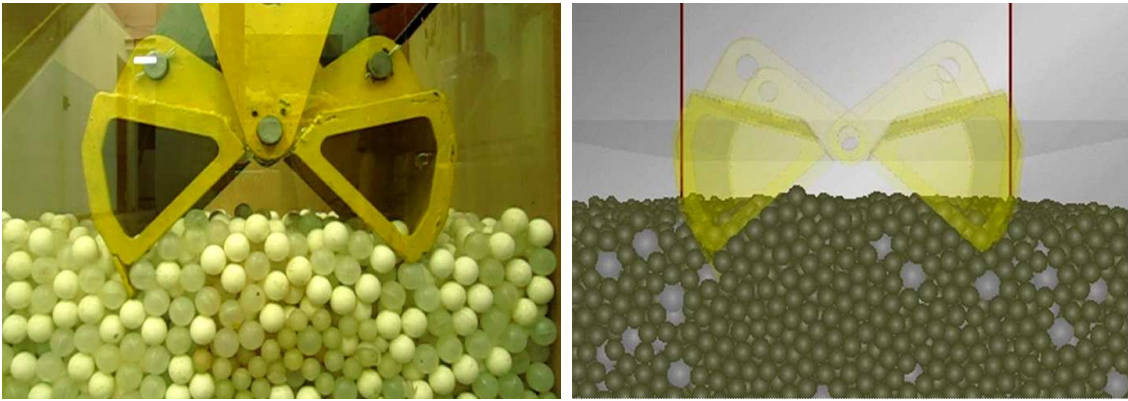


Figure 5.2: Motion comparison of the bucket part 2.

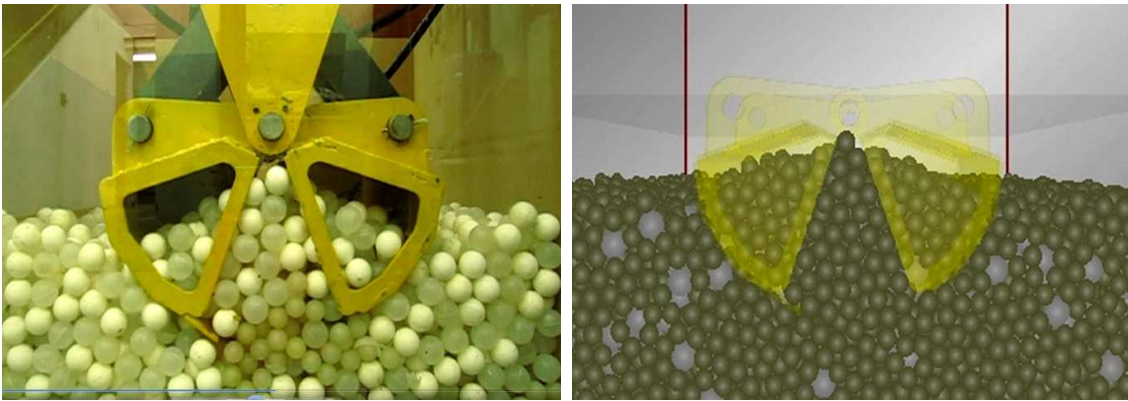


Figure 5.3: Motion comparison of the bucket part 3.

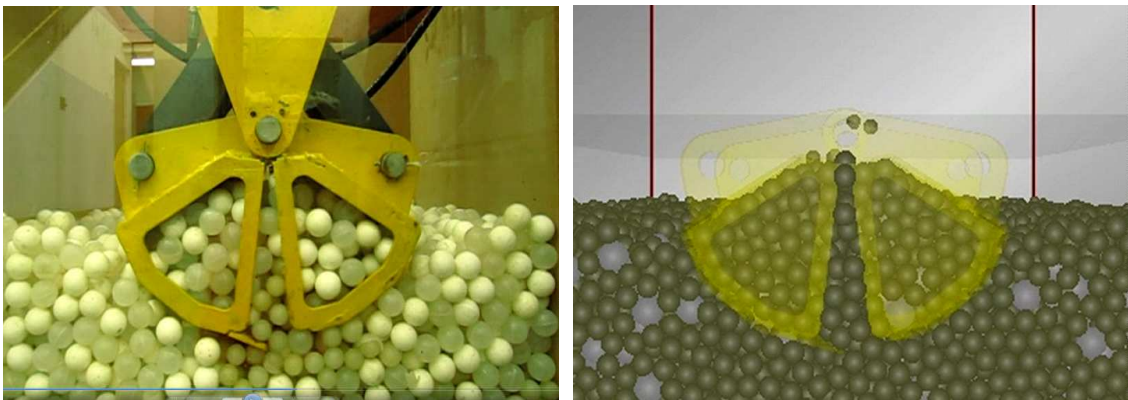


Figure 5.4: Motion comparison of the bucket part 4.

## 5.2 Experimental Data

Experimentation was conducted for various testing conditions as described in Section 4.2. The various sets of results are compared with one another, and in some cases with a representative numerical model as well. It should be noted that the resulting curve in each case is representative of all of the data points for that specific testing condition, these curves were then smoothed using an un-weighted 5 point moving average smoothing function in Matlab.

Figure 5.5 shows the variation of torque with bucket angle for various initial distances from the surface for a constant bucket closing velocity of 20 deg/s while Figures 5.6 to 5.8 show the variation of torque with bucket angle for various different bucket closing velocities at initial distances to surface of of 20 mm, 10 mm and 0 mm respectively.

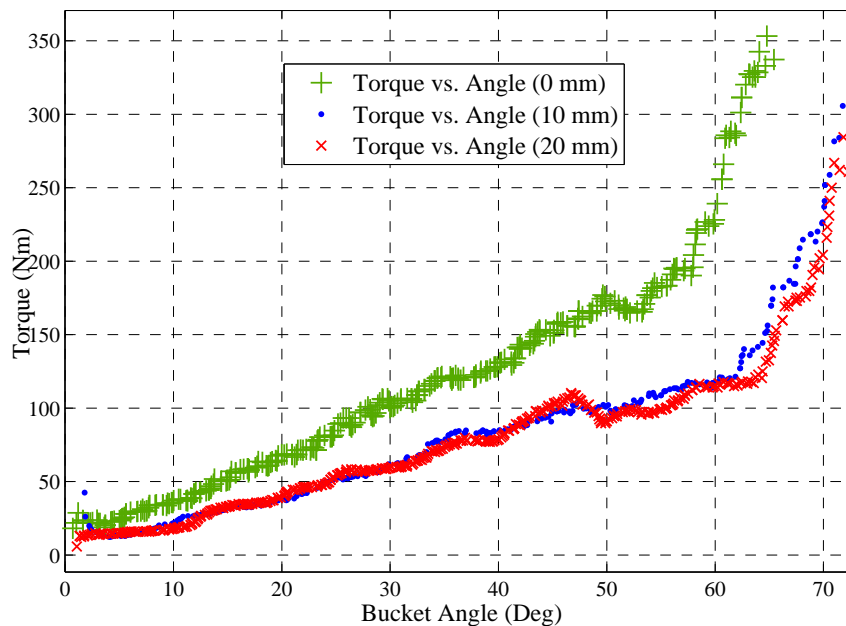


Figure 5.5: Variation of torque with bucket angle for various initial distances from the surface, at a constant velocity (20 deg/s) and a constant boundary position (middle).

Figures 5.9 to 5.11 show the variation of torque with bucket angle while positioned at different boundaries for initial distances to surface of of 20 mm, 10 mm and 0 mm respectively, while Figure 5.12 shows the variation of torque with bucket angle for various different angles of attack for a constant bucket closing velocity of 20 deg/s.

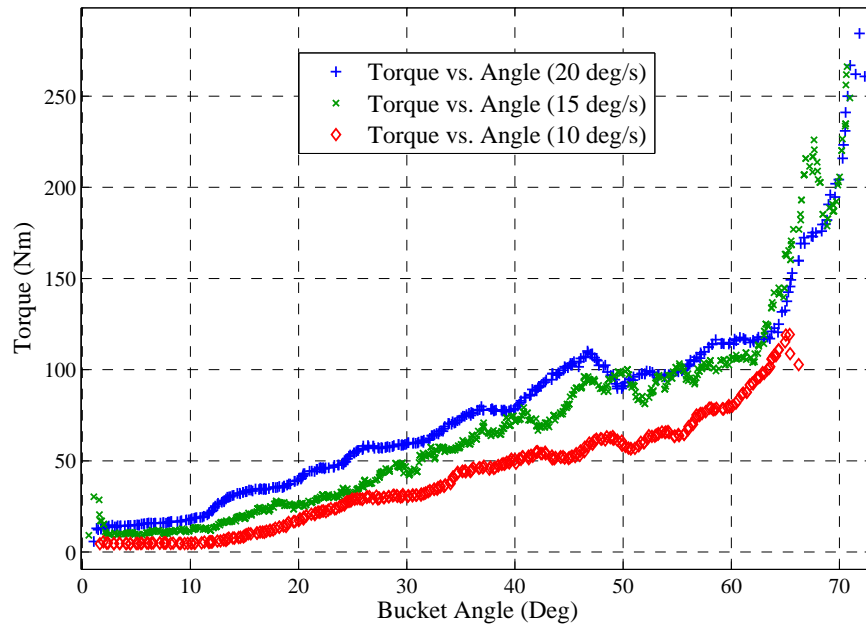


Figure 5.6: Variation of torque with bucket angle for various bucket closing velocities at an initial distance to surface of 20 mm.

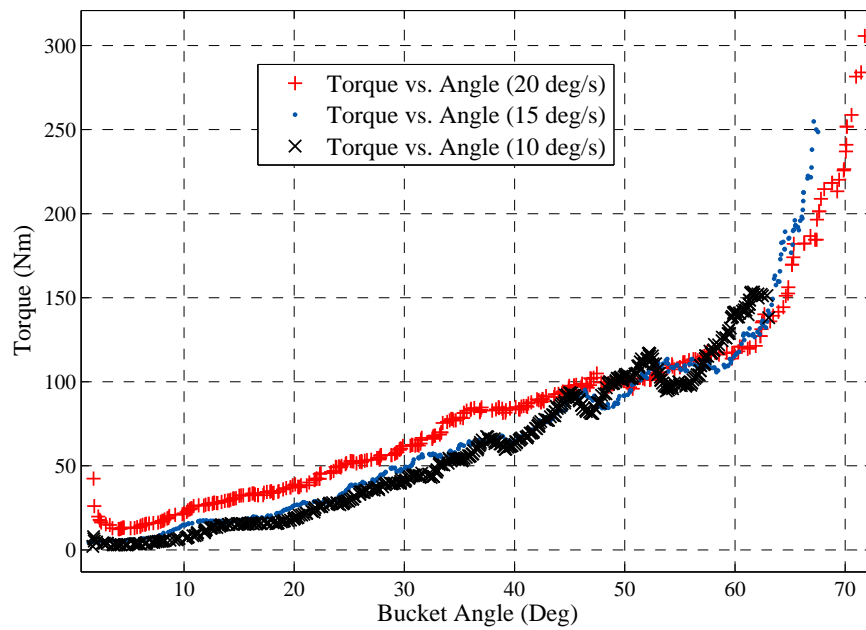


Figure 5.7: Variation of torque with bucket angle for various bucket closing velocities at an initial distance to surface of 10 mm.

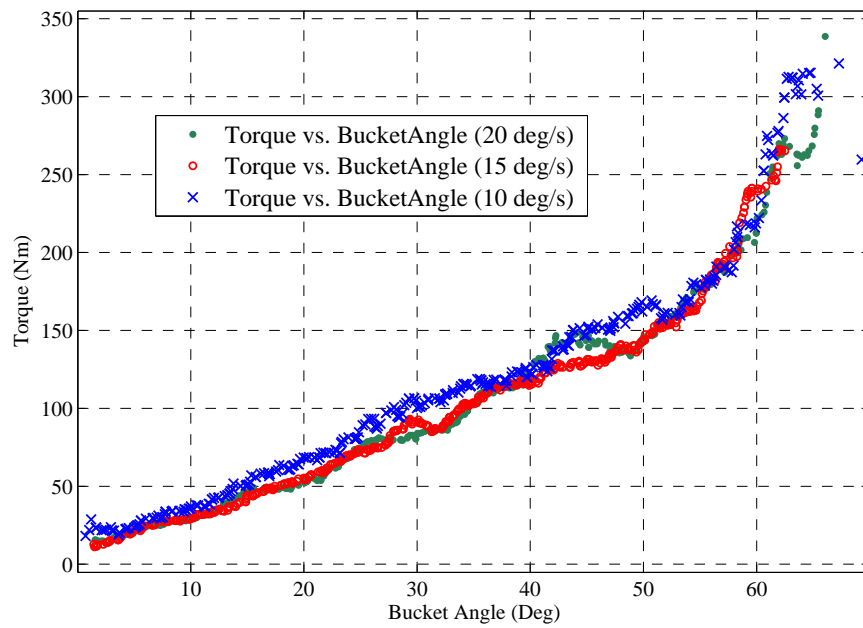


Figure 5.8: Variation of torque with bucket angle for various bucket closing velocities at an initial distance to surface of 0 mm.

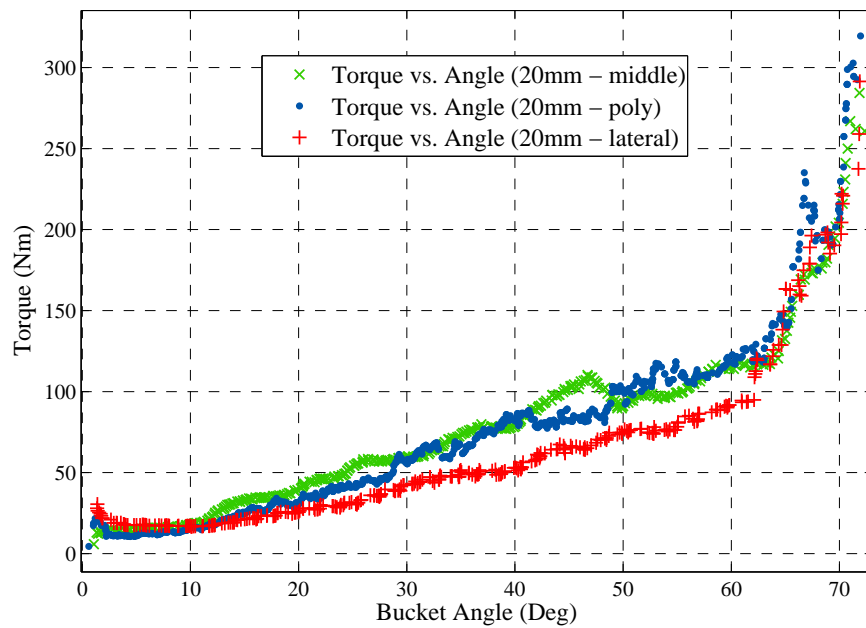


Figure 5.9: Variation of torque with bucket angle for various boundary conditions at an initial distance to surface of 20 mm.

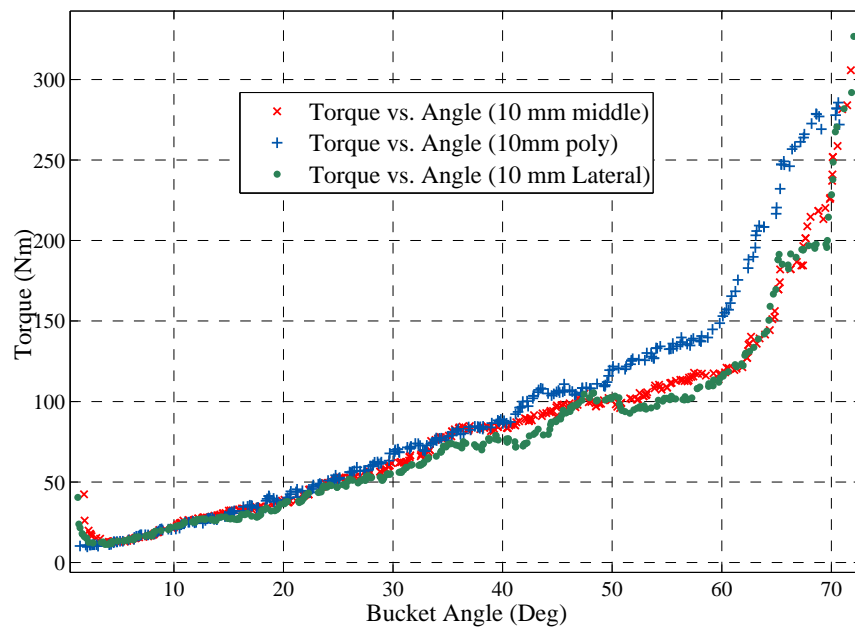


Figure 5.10: Variation of torque with bucket angle for various boundary conditions at an initial distance to surface of 10 mm.

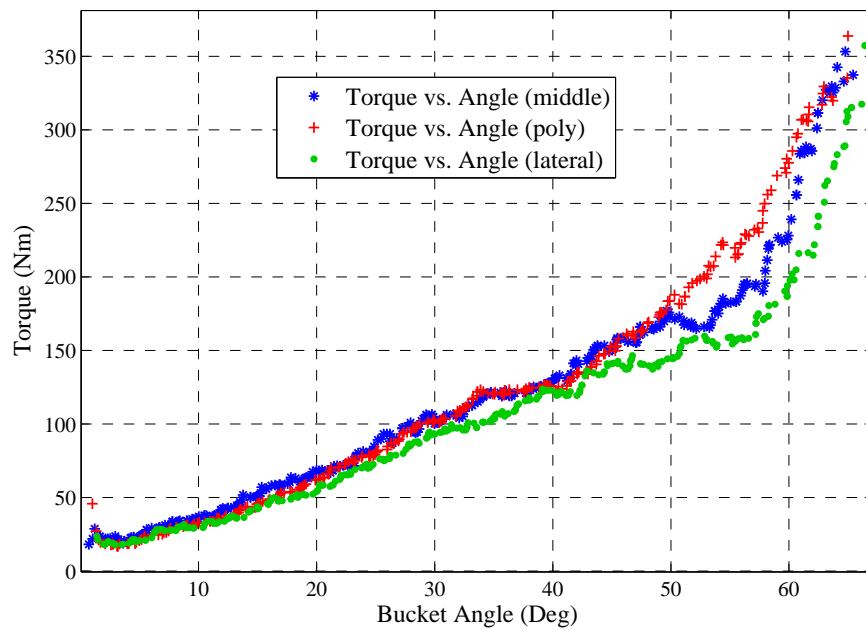


Figure 5.11: Variation of torque with bucket angle for various boundary conditions at an initial distance to surface of 0 mm.

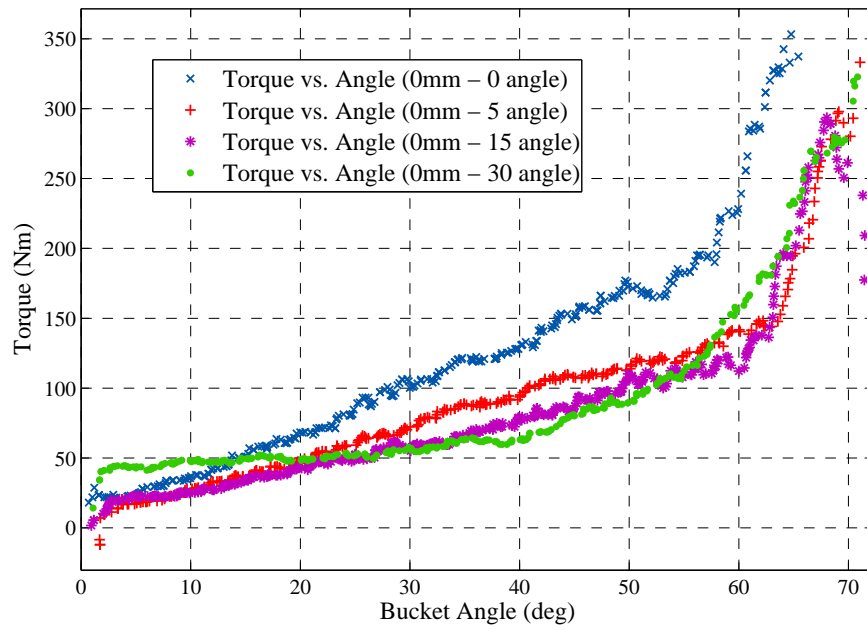


Figure 5.12: Variation of torque with bucket angle for various angles of attack, at a constant velocity (20 deg/s) and a constant boundary position (middle).



### 5.3 DEM Results

The DEM simulation output was represented by a torque about the center of mass of the individual buckets. This needed to be transferred to the point about which both buckets pivot. The coordinates and forces acting through the center of mass were known at each time step. Therefore the total moment about the pivotal point could be calculated for each bucket angular position.

Simulations were conducted for selected physical testing conditions; the various sets of DEM results are compared with one another on common sets of axes.

Figure 5.13 is the simulated variation of torque with bucket angle for bucket closing velocities of 10 deg/s and 20 deg/s at an initial distance to surface of 0 mm, while positioned in the middle of the bed. Figure 5.14 is the simulated variation of torque with bucket angle for different bucket closing velocities at an initial distance to surface of 10 mm, while positioned in the middle of the bed. Figure 5.15 is the simulated variation of torque with bucket angle for bucket closing velocities of 10 deg/s and 20 deg/s at an initial distance to surface of 20 mm, while positioned in the middle of the bed. Figure 5.16 shows the simulated variation of torque with bucket angle for various different initial distances from the surface for a constant bucket closing velocity of 20 deg/s.

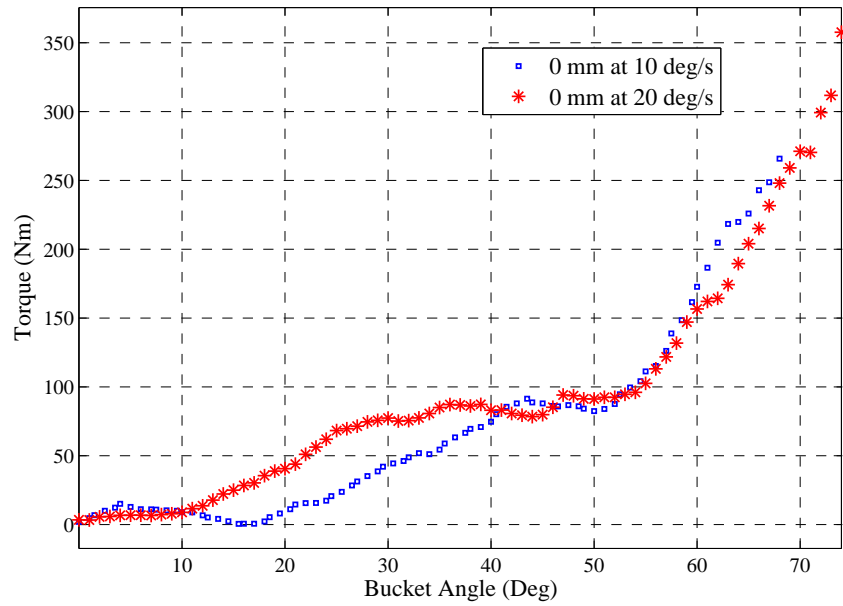


Figure 5.13: Variation of torque with bucket angle for bucket closing velocities of 10 deg/s and 20 deg/s at an initial distance to surface of 0 mm.

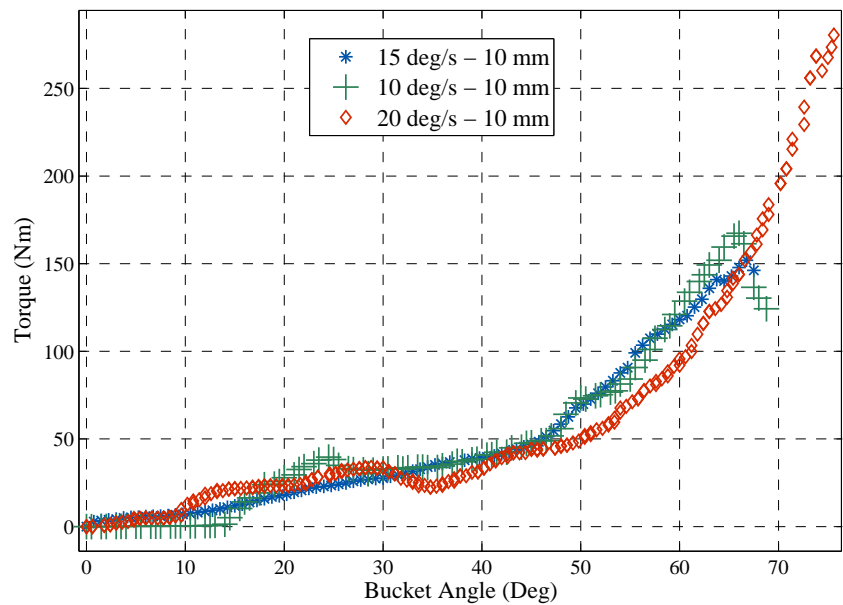


Figure 5.14: Variation of torque with bucket angle for various bucket closing velocities at an initial distance to surface of 10 mm.

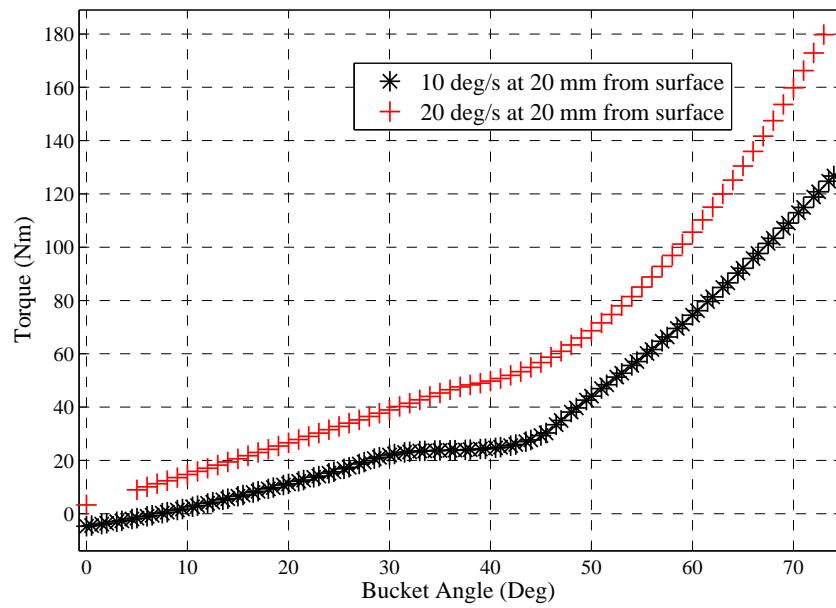


Figure 5.15: Variation of torque with bucket angle for bucket closing velocities of 10 deg/s and 20 deg/s at an initial distance to surface of 20 mm.

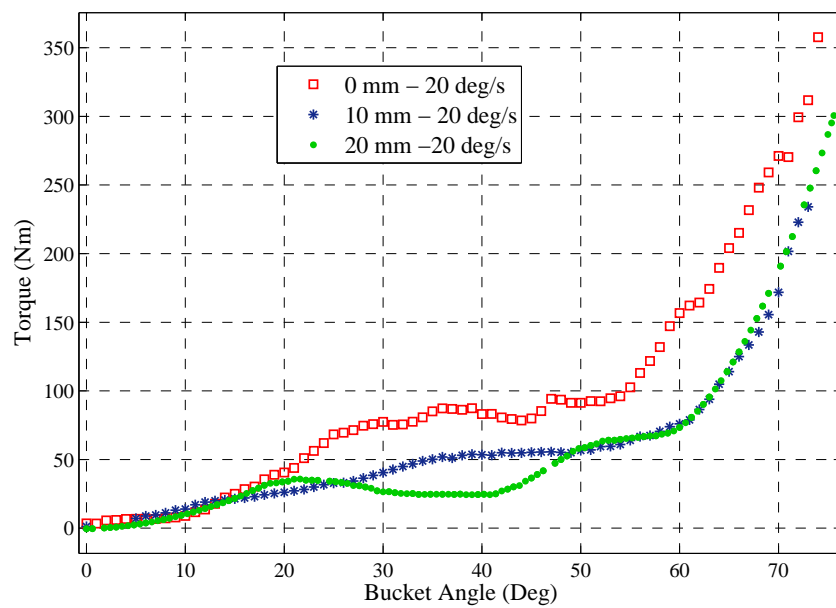


Figure 5.16: Variation of torque with bucket angle for various initial distances from the surface, at a constant velocity (20 deg/s) and a constant boundary position (middle).

## 5.4 Comparison Between DEM and Experimental Results

The DEM results were compared to their corresponding experimental results. These comparisons are illustrated in Figures 5.17 to 5.22. All of the results are for the bucket positioned in the middle of the granular bed, as this would be the most common digging position for the Clamshell Mucker. The experimental data results consist of the data for all of the runs for each test condition combined, and thereafter smoothed using an un-weighted smoothing function in Matlab.

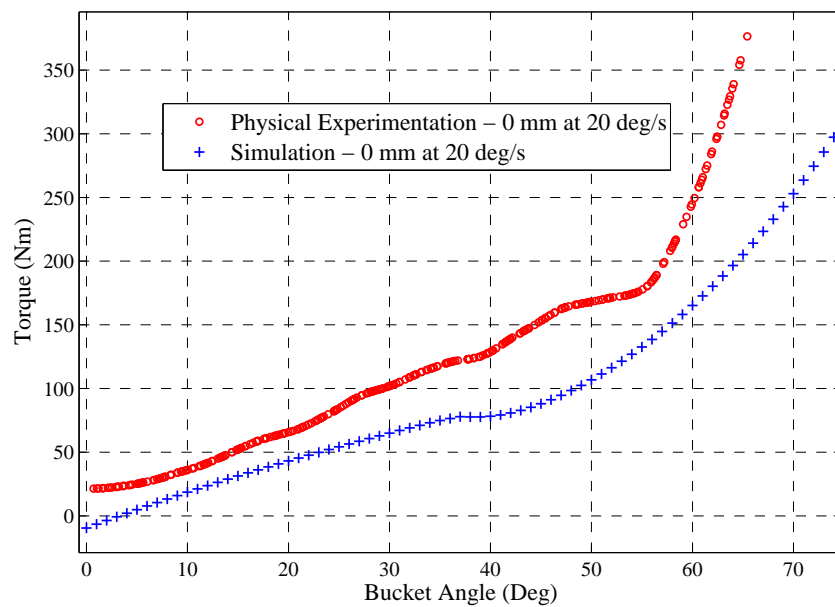


Figure 5.17: Variation of torque with bucket angle for an initial distance from the surface of 0mm and a bucket closing velocity of 20 deg/s for simulated and physical cases.

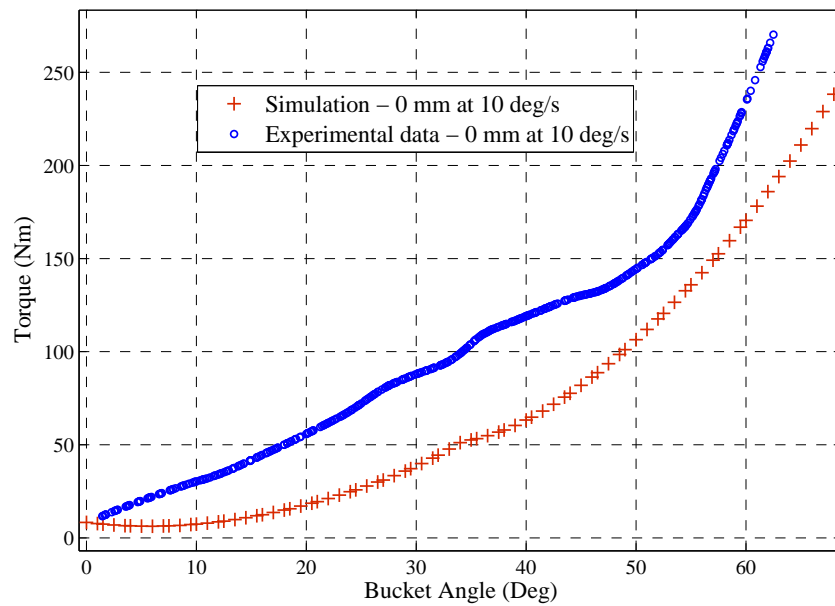


Figure 5.18: Variation of torque with bucket angle for an initial distance from the surface of 0mm and a bucket closing velocity of 10 deg/s for simulated and physical cases.

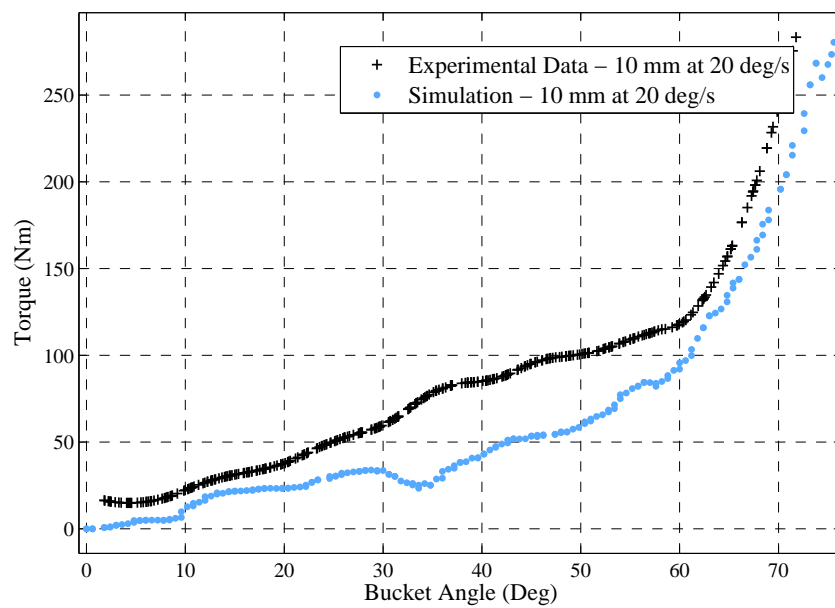


Figure 5.19: Variation of torque with bucket angle for an initial distance from the surface of 10mm and a bucket closing velocity of 20 deg/s for simulated and physical cases.

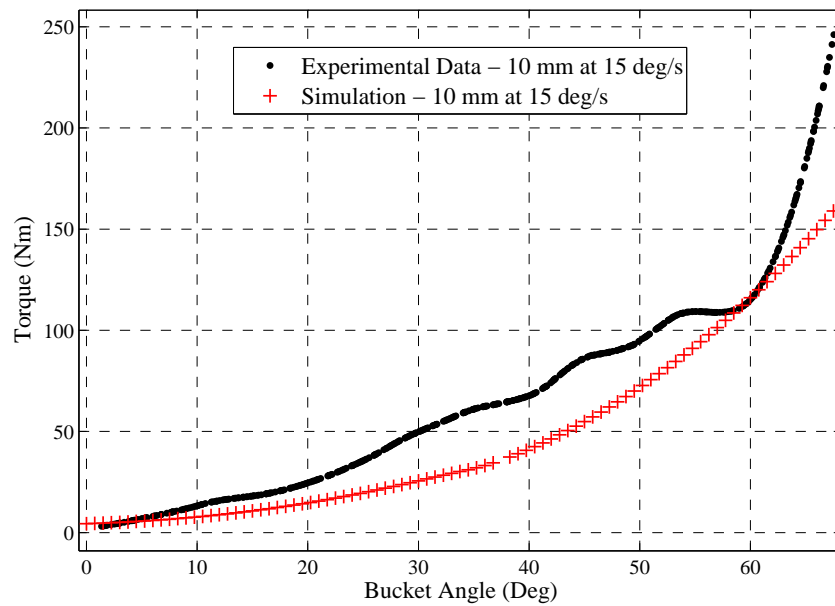


Figure 5.20: Variation of torque with bucket angle for an initial distance from the surface of 10mm and a bucket closing velocity of 15 deg/s for simulated and physical cases.

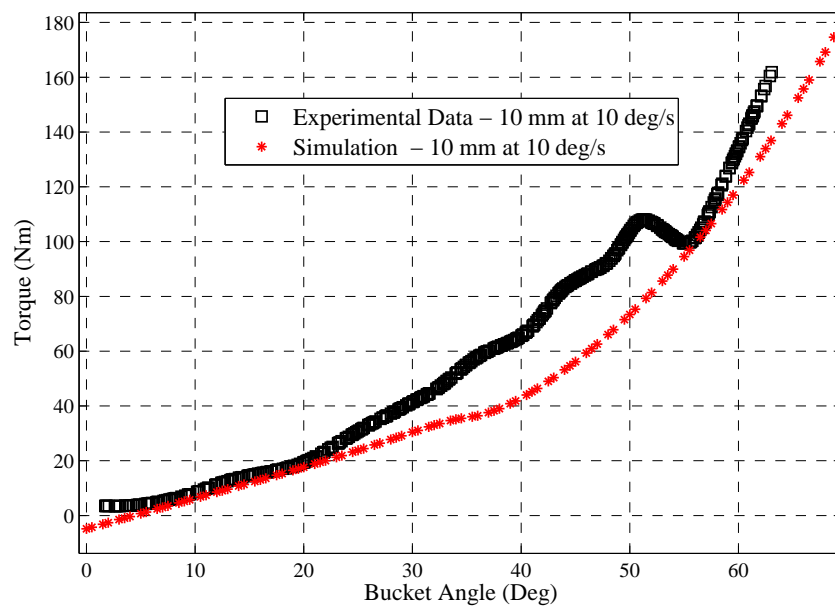


Figure 5.21: Variation of torque with bucket angle for an initial distance from the surface of 10mm and a bucket closing velocity of 10 deg/s for simulated and physical cases.

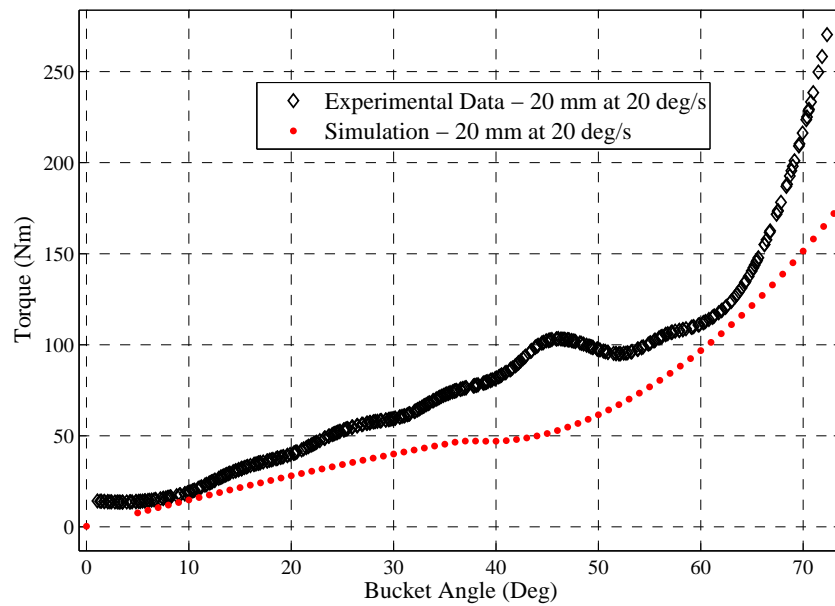


Figure 5.22: Variation of torque with bucket angle for an initial distance from the surface of 20mm and a bucket closing velocity of 20 deg/s for simulated and physical cases.

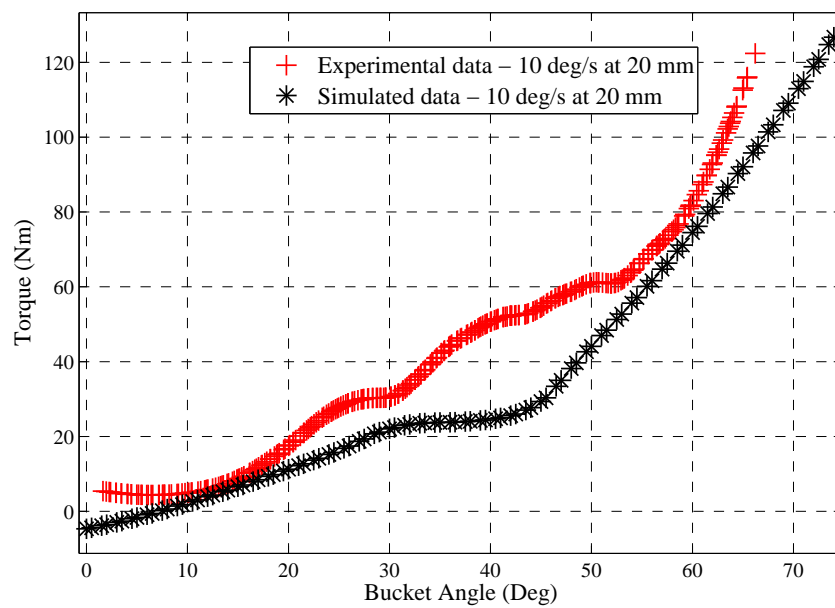


Figure 5.23: Variation of torque with bucket angle for an initial distance from the surface of 20mm and a bucket closing velocity of 10 deg/s for simulated and physical cases.

## 5.5 Energy Levels

Equation 4.5 in Section 4.4.3 was used to produce the variations of energy with angle of penetration shown in Figure 5.24.

The specific energies corresponding to  $0^\circ$ ,  $5^\circ$ ,  $15^\circ$  and  $30^\circ$  for a bucket load of  $0.005 \text{ m}^3$  are given respectively by  $25 \text{ kJ/m}^3$ ,  $21 \text{ kJ/m}^3$ ,  $19.2 \text{ kJ/m}^3$  and  $20.6 \text{ kJ/m}^3$ . Speculatively, if this same specific energy was applicable to a full-scale system, for a 6 m diameter shaft with a 5 m depth of muck pile to be cleared, a maximum saving of up to  $5.8 \text{ kJ/m}^3$  could be achieved, corresponding to about 814.3 kJ in total.

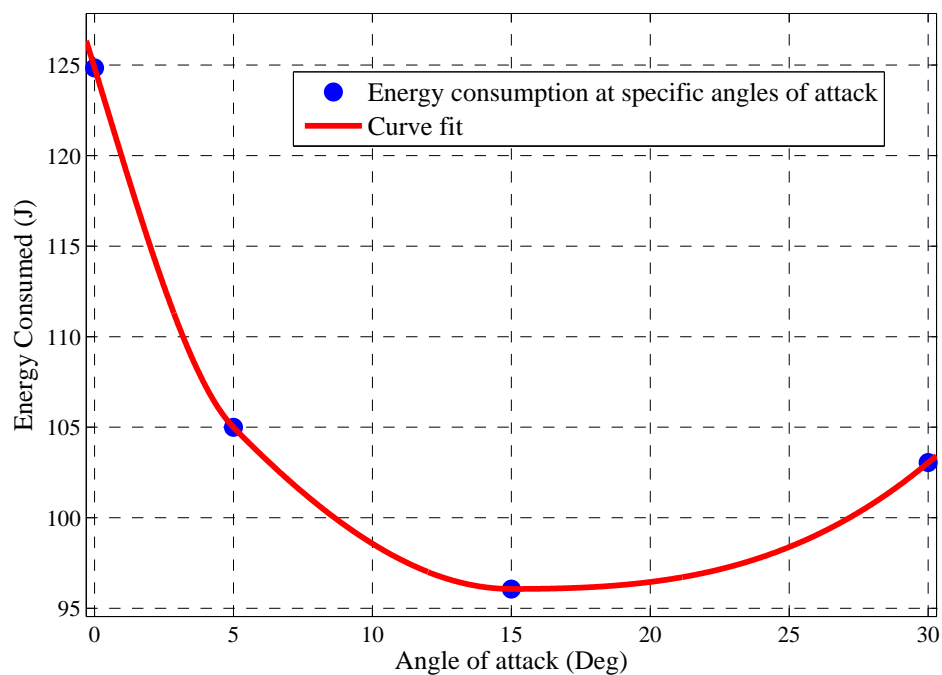


Figure 5.24: Variation of energy required to fill the buckets with angle of attack.



# Chapter 6

## Closure

### 6.1 Discussion

The context of the project embodied an understanding of the mechanisms that occur during the digging motion of a model clamshell mucker unit. The focus of the discussion is interpretation of the experimental data using physically based arguments, followed by reconciliation with data yielded by a Discrete Element Modelling (DEM) code.

The broad experimentation had two primary focal points - qualitative and quantitative comparisons. Qualitative results were derived from images taken during physical testing, which were compared to images captured during the simulations. The quantitative component was a consequence of testing with 13 mm decomposed granite stone, which data was compared to that derived from simulations. The two parts will be discussed individually.

#### 6.1.1 Qualitative Data - Flow Visualization

A visual comparison between material flow in the physical bucket and simulations formed the qualitative component of the study. Figures 5.1 to 5.4 have been repeated here for convenience.

Figures 6.1 to 6.3 display visual comparisons between the physical testing and the simulation for different stages in the digging motion, corresponding to the teeth initially touching the surface

(0 mm) with a bucket closing velocity of 20 deg/s. The primary purpose of the experimentation was to monitor the granular flow in both the physical and numerical systems, and ensure that they displayed similar traits. While corroboration between the static figures at several times can be partly inferred via a comparison between the surface geometries of the balls in each instance (experimental and DEM predictions), a more convincing comparison was obtained using a video analysis, on a CD (forming a part of Appendix F), that should be observed in conjunction with the comments that follow below.

Figure 6.1 represents the start of the digging motion - the jaws of the physical and simulated models start in identical positions and have just entered the bed of plastic balls. The balls are initially being displaced in the direction of the jaw motion, that has a radial and a vertical component. If the video is observed in conjunction with Figure 5.1, it may be seen that the flow of plastic balls is similar in both cases. Figure 6.1 shows the first stage in the motion with additional arrows indicating the direction that the balls are moving.

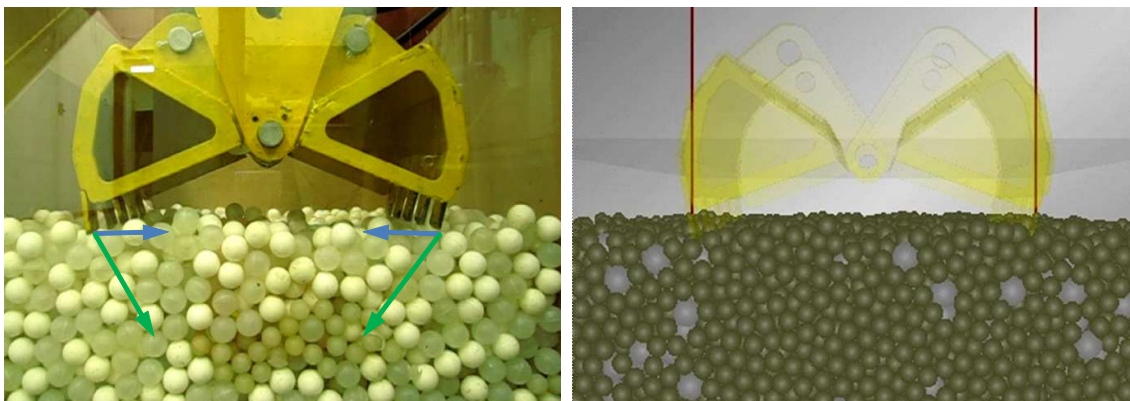


Figure 6.1: Motion comparison of the bucket part 1.

Figure 6.2 shows the physical and simulated jaws at an angular displacement of approximately  $25^\circ$ . In this case the balls have been compacted inwards by the jaws moving towards one another and are thus starting to move vertically upwards, causing the surface to protrude accordingly. This is a result of the jaws closing towards one another forcing the balls to move inwards.

Figure 6.3 portrays images of the respective jaws at an angular displacement of  $45^\circ$ . The protrusion described above has become more pronounced. The balls are being pushed in towards the centre line between the two buckets, the space constraints in the bucket cause them to move upwards. Simultaneously the balls move parallel to the inner surface of the bucket, ultimately causing the particles to move into the corners. The slope of the protrusion eventually becomes too steep to

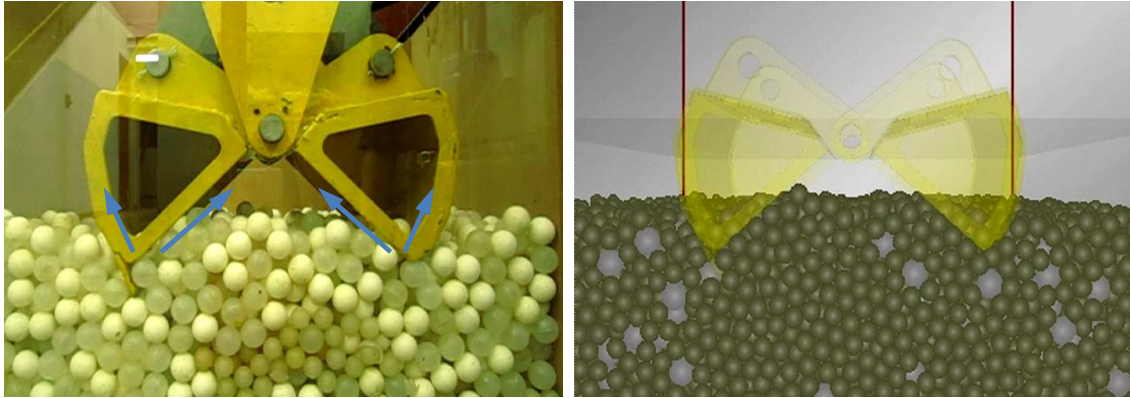


Figure 6.2: Motion comparison of the bucket part 2.

sustain itself and the balls begin to roll down back towards the inner surface of the bucket. The blue arrows in Figure 6.3 represent the upward motion of the particles and the green arrows represent the downward motion of the particles. The flow of particles in the physical and simulated cases are similar. In both cases there is a protrusion with a steep incline and a space between the top of the pile of balls in the bucket and the ceiling of the bucket itself.

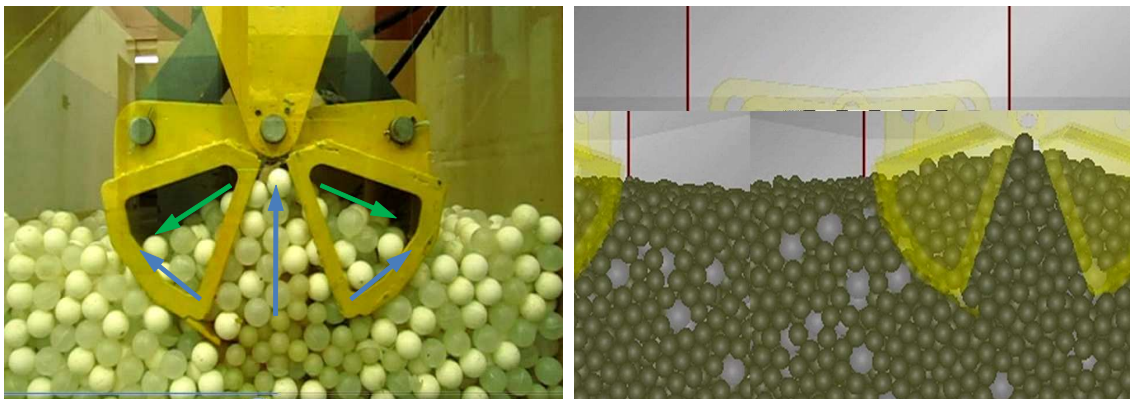


Figure 6.3: Motion comparison of the bucket part 3.

Finally, Figure 6.4 is a representation of the buckets at the most extreme angular position, where they are fully closed and no longer moving. It can be seen that the buckets in both cases are full and the balls occupy the entire volumes of the respective buckets. In the simulated example, balls are ejected from the confines of the bucket, because the volume of the balls exceeded the volume of the buckets and caused crushing of some balls. This same phenomenon was observed during the physical testing. The simulated and physical buckets are both full at the same angular displacement. In general, the qualitative flow characteristics of the simulated and physical models correspond well with one another.

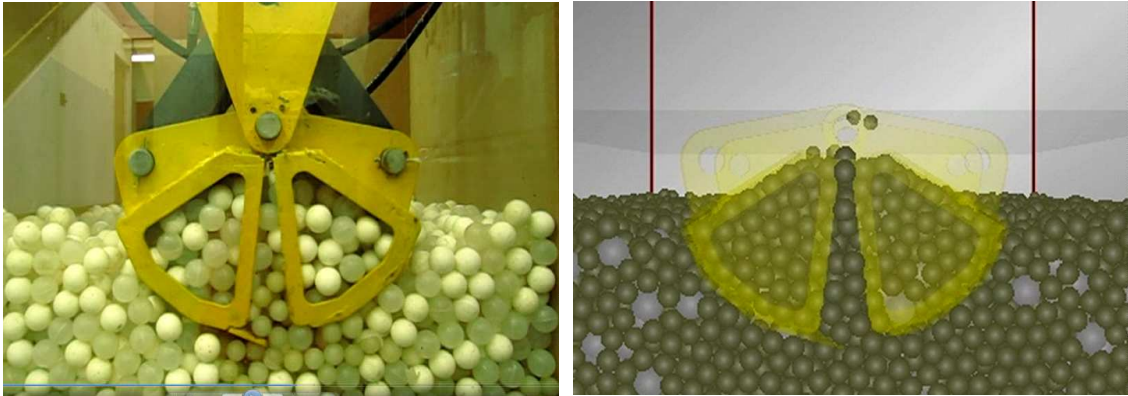


Figure 6.4: Motion comparison of the bucket part 4.

### 6.1.2 Quantitative Data

The quantitative results comprise data acquired from physical testing and simulations. Data are discussed in the context of various combinations of testing parameters; thereafter selected test results are reconciled with simulated results.

From the outset it must be understood that the torque required to rotate the buckets depends primarily on three issues (see Pfeifer, 1999; Wambaugh, 2010; Da Silva 2000 referred to in Section 1.2.2, for a contextual corroboration):

1. The level of fluidization between the particles in the bed, which increases with bucket closing velocity, will result in a reduced torque.
2. The particulate congestion, increasing as the initial distance from the surface of the granular material decreases, will result in an increased torque. In effect this is the inverse of fluidization.
3. The momentum required to move the particles and change their direction, increasing with bucket velocity, will result in an increased torque.

It is the interplay between these issues that leads to the trends that have been observed.

## Repeatability

It is shown in Figure 4.4 that the variation in experimental data is not significant, ranging between 5 and 15 %. Figures 7.32 to 7.34 (in Appendix F) show similar variability in the experimental results. The variability between test runs is thought to occur because of the random shape and size distribution of the particles in the test material.

## Variation of Initial Distances from the Surface

Three different initial distances from the surface to the starting position of the bucket teeth were investigated; namely, 0 mm, 20 mm and 10 mm respectively.

Figure 5.5 shows the variation of torque with angular position for the different initial distances of the teeth from the surface. The penetration velocity (i.e. the rate of angular displacement of the bucket) was kept constant at 20 deg/s and the bucket was positioned in the middle of the granular bed.

It was noticed that starting at an initial distance of 20 mm from the surface of the material, approximately 80% of the volumetric capacity of the bucket was achieved at the end of the travel. It was also found that the jaws moved through the full range of motion, i.e. they were able to close fully unrestricted. Figure 5.5 shows that the case corresponding to a 20 mm starting distance displays an average instantaneous torque at each of the angular bucket positions that is always significantly lower than that at 0 mm. The 20 mm and 10 mm cases display similar average torque readings up to the point  $\beta \simeq 50^\circ$  - thereafter the 10 mm case appears to have a marginally higher average torque through the motion.

When the teeth start 10 mm above the surface of the material it was observed experimentally that the clamshell jaws were filled to capacity at the end of the motion. However at the start, unlike for the 0 mm case, the particles were able to move freely relative to one another, perhaps even leading to a level of bed fluidization. It is only towards the end of the motion that congestion occurs, leading to an abrupt increase in the rate of change of torque with angular position. By comparison, the 0 mm case was congested from the start, leading to a higher rate of change of torque with angular position, arising from friction and interlocking between the particles. The 20 mm case

is similar to the 10 mm one, with congestion occurring somewhat later and with a commensurate delay in the increase.

The average torque required to close the bucket at all angular positions is higher when the teeth start by touching the surface than in the other cases, because through the entire motion a greater volume of material is progressively collected than at the same point for the other cases. In granular materials, the stresses induced by an applied force are distributed to the rest of the medium through a discrete network of grains in contact with one another. The bucket motion is impeded because of these force chains. As the bucket closes, these particles become increasingly compacted, as deduced from an abrupt steepening of the torque curve. In the cases where space is abundant these particles are able to move out of the force chains laterally. However, when there is limited space, as in the case of the teeth starting out at 0 mm, the particles remain linked in these chains, until they are forcefully broken. This impedes the motion of the bucket and increases the torque required to close it.

In the case of the teeth being 20 mm above the surface of the material there is always enough space so that the force chains are not in as stressed a state (i.e. less particle compaction). Therefore particles can move to areas of lower stress with greater ease. In the case of the teeth being 10 mm above the surface of the material there is initially enough space so it requires the same amount of torque as the 20 mm distance above the surface. As it then approaches  $\beta \simeq 52^\circ$  the greater volume of material means that the closing of the bucket is marginally affected. In the case of the teeth being 0 mm, there is a much greater volume of material in the bucket from the outset. At a point the entire volume of the bucket is full and the material becomes a compact clump which inhibits the jaws from closing further.

### **Variation of Penetration Velocities**

Testing at three different velocities (20 deg/s, 15 deg/s and 10 deg/s) was performed to observe the effects of velocity on the clamshell bucket torque. Testing for all three of these velocities was performed at each of the three starting distances from the surface (20 mm, 10 mm and 0 mm).

Figure 5.6 shows the variation of torque with bucket angular position for the three different bucket closing velocities, corresponding to an initial distance of 20 mm above the surface. In this instance

it is clear that the levels of torque increase with increasing angular velocity, from which it is deduced that momentum effects are dominant, as outlined in item 3 above.

The above pattern changes fundamentally when the initial distance from the surface reduces to 10 mm (see Figure 5.7). Here it is seen that the torques for the 20 deg/s case are still significantly higher than for the others. However, the 10 deg/s and 15 deg/s cases are now virtually indistinguishable from one another, suggesting that while momentum is playing a dominant role, congestion (item 2 above) is becoming important.

The trend outlined above continues when the initial distance from the surface is reduced to 0 mm (see Figure 5.8). In this instance the lowest angular velocity (10 deg/s) yields the highest torques, while the 15 deg/s and 20 deg/s cases are similar to each other and at a lower level than the 10 deg/s case. This is indicative of the probability that congestion has now become the dominant factor, consistent with the fact that the two larger angular velocities lead to higher levels of fluidization, as explained in item 1 above.

### **Variation of Boundary Restrictions**

Experimentation was carried out close to various boundaries, in an attempt to simulate the proximity effects that would be encountered in practice - for example, digging close to a side wall.

The three boundary conditions were:- in the middle of the bed, at the forward (polycarbonate) boundary and one of the lateral boundaries (steel). The purpose was to ascertain the effects of the proximity of various boundaries on the torque required to close the bucket. Testing for all three of these bucket placements was performed at each of the three starting distances from the surface (20 mm, 10 mm and 0 mm) at a single bucket closing velocity of 20 deg/s.

As a general comment, particle to boundary interactions in these experiments have lower friction than particle to particle interactions; however, the forward boundary case is more constraining, while the lateral boundary case is not. Therefore, for all three of the starting distances from the surface, it is found that the torque near the respective boundaries is initially lower than for the middle case, until the bucket angle progresses to a point where congestion may occur. This affects the forward case only and not the lateral one. Beyond that point the forward bounded case requires more torque, while the lateral bounded case remains at a lower level.

In the above context, Figure 5.9 shows the variation of torque with bucket angle for various boundary positions, at an initial distance of 20 mm from the surface of the material. The variation of torque with bucket angle while placed at the respective boundaries appears to be indistinguishable initially. Through the middle stages of the motion (from an angular position of about  $10^\circ$  to  $50^\circ$ ) the highest torque observed is when the bucket is positioned in the middle of the reservoir. After the  $50^\circ$  point the forward boundary position exhibits the highest torque characteristics. At all angles the lateral boundary case has the lowest torques.

The lower torques measured at the lateral boundary are attributed to the fact that, as the bucket closes, one side of the jaw interacts with its side wall boundary and the granular material rather than just the granular material. The boundary has a much lower coefficient of friction than the granular material - therefore along this boundary there is less particle interlocking and jamming. In an actual shaft cleaning scenario, side wall roughness would negate this advantage.

The congestion for the forward boundary case justifies further description on the basis of what was visually observed. As noted before, until an angular position of approximately  $50^\circ$  is reached, friction and hence torques are lower than when the jaws are positioned in the middle. Beyond that point when the buckets are full, particles are forced in the direction of the forward boundary and become more constrained than if it did not exist. Thus, they become increasingly compacted, forming a clump, that impedes the motion of the bucket. Therefore after  $50^\circ$  the torque requirements to close the bucket at this boundary are exacerbated.

The same fundamental trend is noticed for the other initial distances from the surface (see Figures 5.10 and 5.11 for 10 mm and 0 mm respectively).

It is important to note that the actual shaft cleaning case would correspond to the experimentation that was conducted adjacent to the front wall, because the lateral case would not effectively clean the shaft.

### **Variation of Angles of Penetration**

The purpose of the testing was to establish the effects on torque of four different angles of attack (see Figure 4.1 part (ii) b), namely  $0^\circ$ ,  $5^\circ$ ,  $15^\circ$  and  $30^\circ$ . In all four cases testing was performed at a constant bucket closing velocity of 20 deg/s, with the closest portion of the bucket initially at 0



mm.

From Figure 5.12 the angle of penetration displaying the highest torque at the lower bucket angular positions (up to about  $14^\circ$ ) is  $30^\circ$ , attributable to the fact that a greater volume of material (relative to the other angles of attack) flows into the bucket.

Beyond a bucket angular position of  $14^\circ$ , the  $0^\circ$  angle of penetration displays the highest torque requirement. This is explained by the fact that the teeth from both sets of jaws touch the muck from the outset of the motion (unlike the other cases where only one jaw initially makes contact with the muck). As the motion commences and the jaws enter the muck, the volume encompassed in the buckets for a given bucket angular position is initially less than the volume of material for the  $30^\circ$  case, with commensurately less torque than for that case. At about  $14^\circ$  it is thought that the particles approaching one another from the two bucket sides come into contact with one another at the centre line between the two buckets. Thereafter, as discussed previously, congestion becomes progressively more dominant with increasing bucket angle. In all other cases only one jaw initially enters the material, with the second following at a later stage. Therefore the particles are not initially being forced together from the buckets moving towards one another. Unlike the  $0^\circ$  angle of penetration case, they are escaping into a free surface, thus delaying the bucket angular position at which congestion takes place. Clearly, it would be expected that the delay of congestion increases with increasing angle of penetration. This is roughly confirmed by the juxtaposition of the data for the  $5^\circ$ ,  $15^\circ$  and  $30^\circ$  cases, in which the torques are generally higher for the smaller angles of attack and increase later for the larger ones.

### **DEM Data**

Figure 5.13 shows a comparison between two velocities with an initial distance to the surface of 0 mm. It can be seen that the beginning and end stages of the motion show indistinguishable differences; however the middle stages of the motion show that the torques for the 20 deg/s closing velocity are higher than the 10 deg/s case. This is dissimilar from the physical trends observed in Figure 5.8, where the 10 deg/s velocity displays higher torque characteristics through the motion. Figure 5.14 shows that the torques for the three velocities are in a narrow range throughout the variation of bucket angles, while the physical measurements (see Figure 5.7) show three lines that are distinct from one another, with the 20 deg/s case having the highest torque characteristics.

Figure 5.15 shows a comparison between two velocities with an initial distance to the surface of 20 mm. The torques for the velocities are distinct from one another throughout the motion, with the 10 deg/s trend being lower than 20 deg/s. This is indicative of the fact that momentum is constant, and similar to the trends observed for the physical measurements (see Figure 5.6). These results imply that the DEM program does not follow the trends in terms of congestion (because of the simplified particle shape); however it appears to model momentum effects appropriately.

Figure 5.16 shows the bucket at different initial distances from the surface, with a constant closing velocity of 20 deg/s. It is shown here that the highest torque required to close the bucket is when it is at 0 mm. The other two cases (i.e. 10 mm and 20 mm from the surface) display similar torque trends, except through the middle range, where the 20 mm separation yields appreciably lower torques. This same general trend is seen with the physical testing (see Figure 5.5), where an initial distance of 0 mm requires the highest torque to close the bucket.

### **Comparison between Physical and Numerical Results**

This part of the discussion embodies a reconciliation between the DEM data and the physical results, using a limited range of the parameters that were used in the experiments.

Figures 5.17 to 5.23 are comparisons between DEM and experimental data for various testing parameters. In all of the above-mentioned figures it can be seen that the simulated and physical results show similar trends towards the beginning and end of the digging motion. However, in the middle of the motion the DEM torque predictions are conservative (low). This is thought to arise from two deficiencies in the DEM modelling:

1. Particle geometries were inherently limited by practical considerations of computational resources. In this context it was mentioned previously that exact particle shapes could not be replicated and only simplified versions of these shapes were created (see Section 3.2.1); therefore it was anticipated that the DEM results would be conservative. This is explained by the fact that the real granular particles have sharp edges and are blocky, while the simulated particles are smooth and do not readily interlock. These sharp edges and blockiness increase particle interlocking effects, and hence the congestion exhibited in the physical model.
2. A second possible effect was errors in the evaluation of the input parameters for the model.

As discussed in Section 3.1, these include:- static friction coefficient, coefficient of rolling friction and coefficient of restitution. While the static friction was obtained experimentally, the coefficients of restitution and rolling friction could not be obtained in this manner (the reasons for this are explained in Section 3.1) and published data were used instead. Hence a sensitivity analysis was performed to determine the overall effects of all of these parameters on the force characteristics of the model (see Section 3.1). In turn each of the parameters considered above (coefficients of static friction, rolling friction and restitution) were altered by +30%,  $\pm 50\%$  and  $-17.3\%$  respectively, to ascertain their effect on the total force experienced by the DEM model. Percentage changes in all of the parameter values relative to the base system lead to force deviations of 3 to 10 percent, implying that any deficiencies in evaluating these parameters did not contribute appreciably to the deviations that were observed.

### **Energy Levels Required for Mucking**

It is not possible to be generally categorical regarding the direct manner in which the current experiments and DEM modelling relate to the real mucking process. However, it is worthwhile noting the trends in Figure 5.24 in Section 5.5 yielded by the exercise described in Section 4.4.3, where estimates were made of the energy levels required to fill a bucket, as a function of angle of penetration.

It is clear that the maximum energy is required for zero angle of penetration, diminishing sharply to an angle of about  $15^\circ$  and then increasing once again. These trends are attributed to the fact that the  $0^\circ$  case is most affected by congestion, whereas it is possible for the larger angles of attack (beyond about  $20^\circ$ ) that the weight of the material has a significant effect on the energy required to close the buckets.

It was considered possible that similar trends would be observed in practice that could potentially reflect in improved operational guidelines for the mucking process. In this context the specific energies corresponding to  $0^\circ$ ,  $5^\circ$ ,  $15^\circ$  and  $30^\circ$  for a bucket load of  $0.005 \text{ m}^3$  are given respectively by  $24.5 \text{ kJ/m}^3$ ,  $21 \text{ kJ/m}^3$ ,  $19.2 \text{ kJ/m}^3$  and  $20.6 \text{ kJ/m}^3$ . Speculatively, if this same specific energy was approximately applicable to a full-scale system, for a 6 m diameter shaft with a 5 m depth of muck pile to be cleared, a maximum saving of up to  $5.8 \text{ kJ/m}^3$  could be achieved, corresponding

to about 814.3 kJ in total.

In the broader context this appears to be inconsequential, but should be subjected to a more comprehensive investigation. Furthermore, alternate cleaning strategies might be adopted to improve the speed and energy characteristics of the mucking cycle. An example of an alternative cleaning strategy would be to initially remove material from the middle of a granular bed and create a depression, thus allowing the Clamshell Mucker to clean at an altered angle of penetration. The operator would continue cleaning in an expanding spiral pattern so that the Clamshell Mucker always makes contact with the material at an appropriate angle of penetration. Furthermore, cleaning by this method would encourage material to fall away from the walls, where it is assumed (from previous arguments) that the torque required to collect a load would increase.

This type of exercise might also be pursued to embrace the manner in which specific energy is affected by bucket closing velocities, as influencing digging rate. While it is likely that the total energy to clear a given muck pile increases with bucket closing velocities, this detrimental effect would be offset by the improved cycle time of the process and hence an economical optimization would be conducted, properly taking cognisance of these effects.

## 6.2 Conclusions

1. A scaled experimental rig of a clamshell mucker was developed to embody an appropriate range of geometrical and operating parameters. Various experimental parameters were tested for two different materials: hard plastic balls and thereafter 13 mm decomposed granite stone.
2. The hard plastic balls were used as a *qualitative* comparison between DEM and physical testing, using both video and still photography comparisons, corresponding to the teeth initially touching the surface with a bucket closing velocity of 20 deg/s. The correlations obtained by this means were generally favourable, within the limitations of a heuristic reconciliation.
3. Quantitative testing was conducted by measuring the bucket closing torque variation with bucket angle for various combinations of the following parameters: (a) bucket closing velocity, (b) initial distance of bucket from muck pile, (c) proximity of bucket to side and front walls and (d) angle at which bucket assembly enters the muck pile.

4. The first and main set of tests (Case I) took place with the bucket entering vertically and positioned in the middle of the bed (i.e. away from the walls). Three different initial distances from the surface to the starting position of the bucket teeth were investigated - 20 mm, 10 mm and 0 mm respectively, for each of which for each of which bucket angular velocities of 10 deg/s, 15 deg/s and 20 deg/s were explored.

Thereafter (Case II), testing was conducted with the bucket in the middle of the bed, at the forward (polycarbonate) boundary and one of the lateral boundaries (steel), with each placement for a single bucket velocity of 20 deg/s and successively covering the three starting distances from the surface (20 mm, 10 mm and 0 mm), in an attempt to simulate the proximity effects that would be encountered in practice - for example, digging close to a side wall.

Finally (Case III), torque variations with bucket angle were established at four different angles of attack ( $0^\circ$ ,  $5^\circ$ ,  $15^\circ$  and  $30^\circ$ ), at a constant bucket closing velocity of 20 deg/s, with the closest portion of the bucket initially touching the surface (at 0 mm).

5. General interpretation of the data suggests that the torque required to rotate the buckets appears to depend on an interplay between the following issues: (a) the level of fluidization between particles in the bed, increasing with bucket closing velocity, results in a reduced torque; (b) particulate congestion, increasing as the initial distance from the surface of the granular material decreases, results in an increased torque; and (c) the momentum required to move the particles and change their direction, increasing with bucket velocity, results in an increased torque. Within this context the following physical inferences may be drawn from the various testing combinations in item 4 above:

- (a) *Case I.* Starting with an initial distance of 20 mm, torques increase with angular velocity, implying that momentum effects are dominant. At an initial distance of 10 mm the highest velocity (20 deg/s) gives the largest torques; however, there is virtually no distinction between the other two cases, suggesting that congestion is becoming important. This trend continues when the initial distance is reduced to 0 mm, whereupon the lowest angular velocity (10 deg/s) yields the highest torques, while the 15 deg/s and 20 deg/s cases are similar to each other and at a lower level than the 10 deg/s case. This is consistent with congestion becoming the dominant factor, where the higher velocities lead to higher levels of fluidization.

- (b) *Case II.* Generally speaking, particle to boundary interactions have lower friction than particle to particle interactions, counterbalanced by the possible constraining effects of boundaries. In this instance the forward boundary case is more constraining, while the lateral boundary case is not. Therefore, for all three of the starting distances from the surface, it was found that the torque near the respective boundaries is initially lower than for the middle case, until the bucket angle progresses to a point where congestion occurs, affecting the forward case only. Beyond that point this bounded case requires more torque, while the lateral bounded case remains at a lower level.
- (c) *Case III.* For bucket angles up to about  $14^\circ$  the largest angle of attack ( $30^\circ$ ) yields the highest torque, because a greater volume of material (relative to the other angles of attack) flows into the bucket. Thereafter, the  $0^\circ$  angle of penetration displays the highest torque requirement, because the teeth from both sets of jaws touch the muck from the outset of the motion and it is thought that the particles approaching one another from the two bucket sides come into contact with one another at the centre line between the two buckets. Thereafter, congestion becomes progressively more dominant with increasing bucket angle. In all other cases only one jaw initially enters the material, with the second following at a later stage. Therefore the particles are not initially being forced together from the buckets moving towards one another: they are escaping into a free surface, thus delaying the bucket angular position at which congestion takes place. Because the delay of congestion increases with increasing angle of penetration, torques are generally higher for the smaller angles of attack, increasing later for the larger ones.
6. Comparisons between DEM data and measurements for various testing parameters showed that the simulated and physical results display similar values of torque towards the beginning and end of the digging motion, but DEM predictions are low in the middle of the range. This is thought to arise primarily from the fact that simplified particle geometries (smooth, with no sharp edges) were chosen in the DEM model because of computational resource limitations, whereas the real granular particles have sharp edges and are blocky, thus increasing particle interlocking effects and the higher level of congestion exhibited in the physical experimentation. This effect was generally reflected by poor comparisons between DEM data and experimentation in the context of torque variations with velocity in the middle range of angular positions.

Because the coefficients of rolling friction and restitution were obtained from published data, additional simplified simulations were run to determine the sensitivity of these parameters (in addition to static friction coefficient, for comparative purposes) on the force characteristics of the model. Specifically chosen percentage deviations in all of the parameter values relative to the base system led to percentages of force deviation that were at least 3 to 5 times smaller. Therefore, it was decided that deficiencies in accurately specifying coefficients of static friction, rolling friction and restitution contributed negligibly to the deviations that were observed, reinforcing the inference that particle interlocking effects were dominant.

7. The maximum energy to fill the buckets occurs for the zero angle of penetration case, diminishing sharply to an angle of about  $15^\circ$  and then increasing once again. This trend is attributed to the fact that the  $0^\circ$  is most affected by congestion, whereas for the larger angles of attack (beyond about  $20^\circ$ ) the weight of the material significantly affects the energy required to close the buckets.

While it was considered possible that similar trends would be observed in practice, that could potentially reflect in improved operational guidelines for the mucking process, further analysis suggested that an energy saving of less than 814.3 kJ might be attainable for clearing a 6 m diameter shaft during a single cycle.

### 6.3 Recommendations

1. The test facility should be modified so that tests can be conducted over a larger range of bucket angular velocities.
2. Testing should be conducted with a broader range of particle sizes.
3. Research into the interlocking and frictional effects of rock should be pursued, to create representative particulate shapes as input to the DEM model, while maintaining computational efficiency. All such work should be corroborated experimentally.
4. DEM modelling using the current computational resources should include the introduction of higher friction coefficients as a means of artificially compensating for interlocking effects, that are impractical to achieve because of computer resource limitations.

5. Testing should be conducted with a range of different bucket shapes and sizes for the purpose of optimizing the design in terms of minimizing structural stresses and the specific energies required to collect individual loads.



## 6.4 References

- Baker, M. (2010) Physics - Collisions in 1 dimension. Last accessed: November 2010  
<http://www.euclideanspace.com/physics/dynamics/collision/oned/index.htm>
- Beardmore, R. (2010) Coefficients of Friction. Retrieved September 9, 2010, from RoyMech Web site: <http://www.roymech.co.uk/Useful-Tables/Tribology/co-of-frict.htm>
- Burke, K. (2010) Private communication, School of Geosciences, University of the Witwatersrand, Johannesburg.
- Cleary, P. W. (2003) Large scale industrial DEM modelling. *Engineering Computations*, vol 21. Emerald Group Publishing.
- Cleary, P.W. (1998) The filling of dragline buckets. *Math. Eng. Ind.* 7 (1-24)
- Coetzee, C. (2009) The Modelling of Bulk Materials Handling using the Discrete Element Method. *1st African Conference on Computational Mechanics - An International Conference, AfriCOMP 2009*
- Coetzee, C.J. et al. (2008) Calibration of discrete element parameters and the modelling of silo discharge and bucket filling. *Computers and Electronics in Agriculture*. V65 198-212. Elsevier.
- Coetzee, C.J. et al. (2009) Discrete element parameter calibration and the modeling of dragline bucket filling. *Journal of Terramechanics*, Elsevier.
- Constantinides, G. et al. (2007) Quantifying deformation and energy dissipation of polymeric surfaces under localized impact. *Materials Science and Engineering: A*, Elsevier Volume 489, Issues 1-2.
- Cryderman. W.L. (1952) Apparatus for use in Shaft Sinking. United States Patent Office, Patent Number 2, 606, 670.
- Cundall, P.A. & Strack, O.D.L. (1979) A discrete numerical model for granular assemblies. *Geotechnique*, Vol 29, No. 1, 47-65.

Da Silva, M. & Rajchenbach, J. (2000) Stress transmission through a model system of cohesionless elastic grains. *Nature* - Vol. 406 , pp. 708-710.

DEM Solutions. EDEM Training Manual. Revision 2.

Douglas, A.A.B and Pftzenreuter, F.R.B. (1989) Overview of current South African vertical circular shaft construction practice. *Shaft Engineering, Institution of Mining and Metallurgy*.

Durda, D. et al. (2010) Experimental determination of the coefficient of restitution for meter-scale granite spheres. *Icarus* Volume 211, Issue 1 Pg 849-855.

Eimco, N.D. <http://www.tridentsa.co.za/eimcoload.php>.

Engineering Toolbox. A. (n.d.). Modulus of Rigidity. Retrieved May 3, 2010, from Engineering Toolbox website: <http://www.engineeringtoolbox.com/modulus-rigidity-d-946.html>

Engineering Toolbox. B (n.d.). Poisson's Ratio. Retrieved May 3, 2010, from Engineering Toolbox website: <http://www.engineeringtoolbox.com/poissons-ratio-d-1224.html>.

General properties - Some Useful Numbers on the Engineering Properties of Materials (Geologic and Otherwise) GEOL 615 <http://www.stanford.edu/~tyzhu/Documents/Some%20Useful%20Numbers.pdf>

South African mining industry snapshot 2009. Viewed October 9, 2010 <http://www.bullion.org.za/Publication/F%20&%20F%202010%20Final.pdf>

Hill, K.M. et al (1999) Segregation- driven organization in chaotic granular flows. *Proc. National Academy of Science of USA* 96, 11701-11706.

Holt R.M. et al, (2005) Comparison between controlled laboratory experiments and discrete particle simulations of the mechanical behaviour of rock. *International journal of Rock Mechanics and Mining Sciences*, V42 985-995 Elsevier.

Imre, B. et al. (2008) A coefficient of restitution of rock materials. *Computers & Geosciences archive* Volume 34 Issue 4 Pergamon Press.

Kosloff, R., Kosloff, D. (1985) Absorbing Boundaries for Wave Propagation Problems. *Journal of computational physics*

- Ling, L. (2003). A review of techniques, advances and outstanding issues in numerical modeling for rock mechanics and rock engineering. *International Journal of Rock Mechanics & Mining Sciences*, Vol 40, 283-353.
- Liu, J. et al, (2009) Visualization of force networks in 2D dense granular. *Frontiers of Architecture and Civil Engineering in China*, Higher Education Press and Springer-Verlag Volume 4, Number 1, 109-115.
- MacChonachie. H. (1959) Shaft Sinking practice in South Africa. *Symposium on shaft sinking and tunneling. The Institute of Mining Engineers*, pp 14-19.
- MBendi. (2009) *Mining in South Africa - An Overview* last accessed: 05/10/2009  
<http://www.mbendi.com/indy/ming/af/sa/p0005.htm>
- Nave, R. (2005) Hyperphysics. <http://hyperphysics.phy-astr.gsu.edu/hbase/frict2.html>: last accessed 10/02/2011
- Peng, Z.et al. (2009) Depth dependence of vertical plunging force in granular medium. *Physical Review E* - Vol 80 , 021301.
- Pfeifer, M.A. et al. (1999) Slow drag in a granular medium. *Physical Review Letters* - Vol 82 , pp. 205-208.
- Puglisi, A, (2001) Janssen effect and the distribution of internal stresses. Retrieved September 9, 2010, from TNT Group: <http://denali.phys.uniroma1.it/puglisi/thesis/node5.html>
- Seguin, A., Bertho, Y. & Gondret, P, (2008) Influence of confinement on granular penetration by impact. *Physical Review E* - Vol 78 , 010301.
- Sim, N, (2010) Investigation into boundary effects on penetration of granular materials. Research Project pg 7.
- Simanek, D. (2010) <http://www.lhup.edu/dsimanek/scenario/rolling.htm> Last accessed: November 2010.
- Stone, M. B. et al, (2004) Local jamming via penetration of a granular medium. *Physical Review E* - Vol 70.

- Taylor, R.N.M. (1981) The mechanical cleaning of a small diameter shaft. *Association of Mine Managers*, 1/81.
- Thorensson, M. (2010). How to correctly generate a loosely-packed particle field. (S. Moss, Interviewer). Private communication, Esteq.
- Walton, O.R. et al. (1999) A 3-D discrete-element method for dry granular flows of ellipsoidal particles. *Computer methods in applied mechanics and engineering*, Elsevier.
- Wambugh, J. F. (2010) Simple models for granular force networks. *Physica D*, Elsevier.
- Wang, L. et al. (2005) Representation of real particles for DEM simulation using X-ray tomography. *Construction and Building Materials*. V21, p 338-346. Elsevier
- Yardley, D.H. (1970) Rapid excavation problems and progress. *American Institute of Mining, Metallurgical, and Petroleum Engineers*, pp 195-207.
- Zhu, H.P et al. (2007) Discrete particle simulation of particulate systems: Theoretical developments. *Chemical Engineering Science*, Elsevier.
- Zhu, H.P. et al. (2008) Discrete particle simulation of particulate systems: A review of major applications and findings. Lab for Simulation and Modelling of Particulate Systems, *Chemical Engineering Science*. Elsevier.
- Zhu, H.P. et al. (2006) Discrete particle simulation of particulate systems: Theoretical developments. Centre for Simulation and Modelling of Particulate Systems. *Chemical Engineering Science*. Elsevier

# Chapter 7

## Appendices

### Appendix A - Bucket Torques

#### Force and Angle Relationships

The purpose of this exercise was to relate the pressure in the hydraulic cylinder to the torque required to close the clamshell bucket. Figures 7.1 to 7.3 show the external forces ( $F_{G1}$ ,  $F_y$ ,  $F_R$  and  $F_p$ ) and successive internal forces ( $F_{L1}$ ,  $F_{L2}$ ,  $F_{B1}$  and  $F_x$ ) acting on the system.

Under the assumptions

1. The force exerted by the sliding pin on each of the linkages is identical in magnitude.
2. The force exerted by each of the bucket edges on the muck is therefore the same.
3. There is no resultant force in the horizontal direction on the bucket pin.

static equilibrium of forces and moments yield

$$\sum F_x = 0 = -F_P \sin(\theta) + F_R + F_{L1} \sin(\alpha) - F_{L2} \sin(\alpha) \quad (7.1)$$

$$\sum F_y = 0 = -F_P \cos(\theta) + F_{L1} \cos(\alpha) + F_{L2} \cos(\alpha) \quad (7.2)$$

$$F_{L1} = F_{B1} \quad (7.3)$$

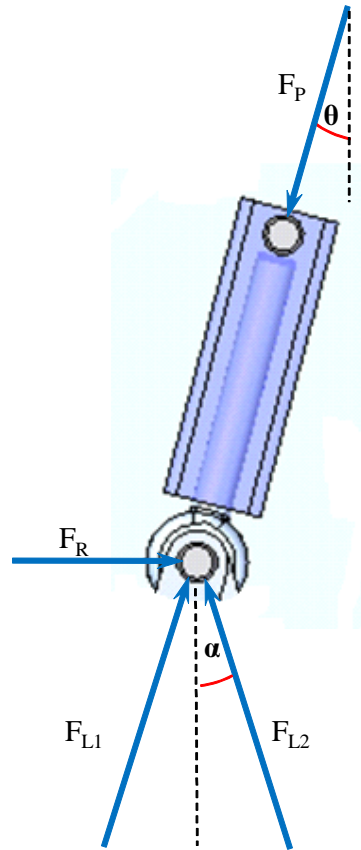


Figure 7.1: Forces exerted by the cylinder on pin joints.

$$0 = -F_{B1} \sin(\alpha) - F_{G1} \sin(\beta) + F_x \quad (7.4)$$

$$0 = F_y - F_{B1} \cos(\alpha) + F_{G1} \cos(\beta) \quad (7.5)$$

$$0 = -F_{G1} \ell + F_{B1} \cos(\alpha) R \sin(\gamma_1) + F_{B1} \sin(\alpha) R \cos(\gamma_1) \quad (7.6)$$

and

$$F_{B1y} = F_{B1} \cos(\alpha) \quad (7.7)$$

$$F_{B1x} = F_{B1} \sin(\alpha) \quad (7.8)$$

$$T = F_{B1y} R \cos(90 - \gamma_1) + F_{B1x} R \sin(90 - \gamma_1), \quad (7.9)$$

thus defining an implicit relationship between  $F_p$  and  $T$ .

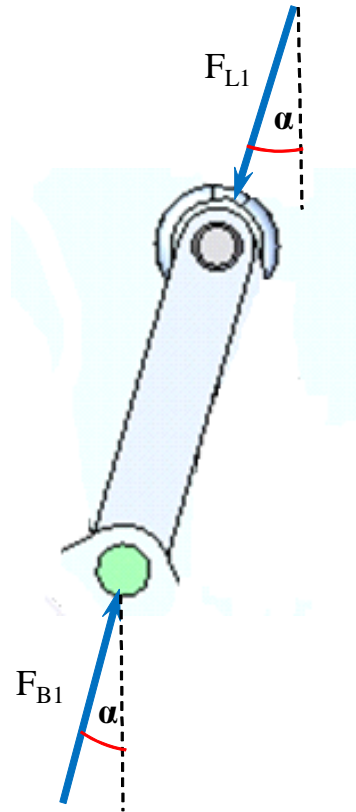


Figure 7.2: Forces exerted on a linkage.

The relationship between the actuator angle  $\theta$  and bucket angle  $\gamma$  was obtained from the implicit groups of relationships

$$x = z - z_1 \quad (7.10)$$

$$z = c \cot \theta \quad (7.11)$$

$$z_1 = c \cot \theta_1 \quad (7.12)$$

$$x = c(\cot \theta - \cot \theta_1) \quad (7.13)$$

$$c = A \sin \theta_1 \quad (7.14)$$

$$x = A \sin \theta_1 (\cot \theta - \cot \theta_1) \quad (7.15)$$

$$x = R - R \cos \gamma_1 + L - L \cos \alpha \quad (7.16)$$

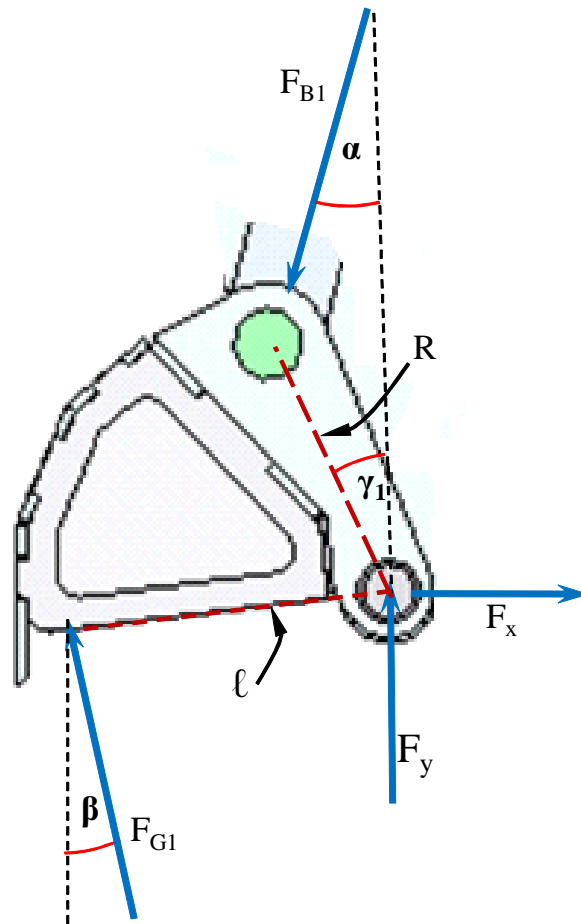


Figure 7.3: Forces exerted on the bucket.

$$\gamma_1 = 79.98^\circ - \gamma \quad (7.17)$$

and

$$R - R \cos \gamma_1 + L - L \cos \alpha = A \sin \theta_1 (\cot \theta - \cot \theta_1) \quad (7.18)$$

where the various parameters are defined in Figures 7.4 and 7.5, and the geometrical constants for the system are given in Table 7.1. Figure 7.4 represents the hydraulic actuator and sliding pin, where the line between Pin 1 and Pin 2a represents the hydraulic cylinder fully retracted, and the line between Pin 1 and Pin 2b symbolizes it fully protracted.



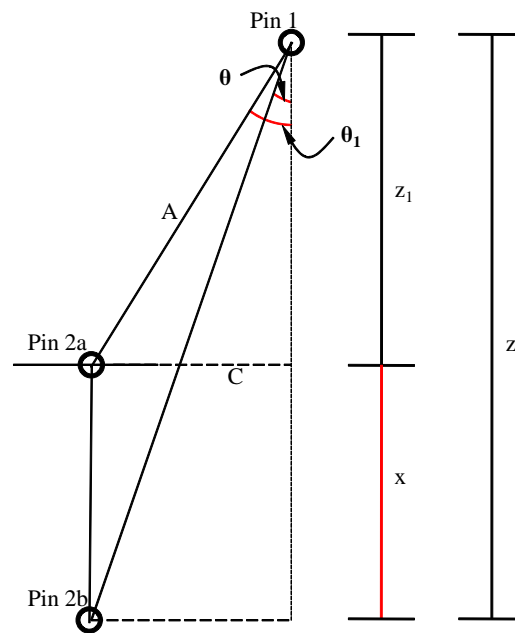


Figure 7.4: A schematic of the angular position of the cylinder relative to the linear position of the sliding pin.

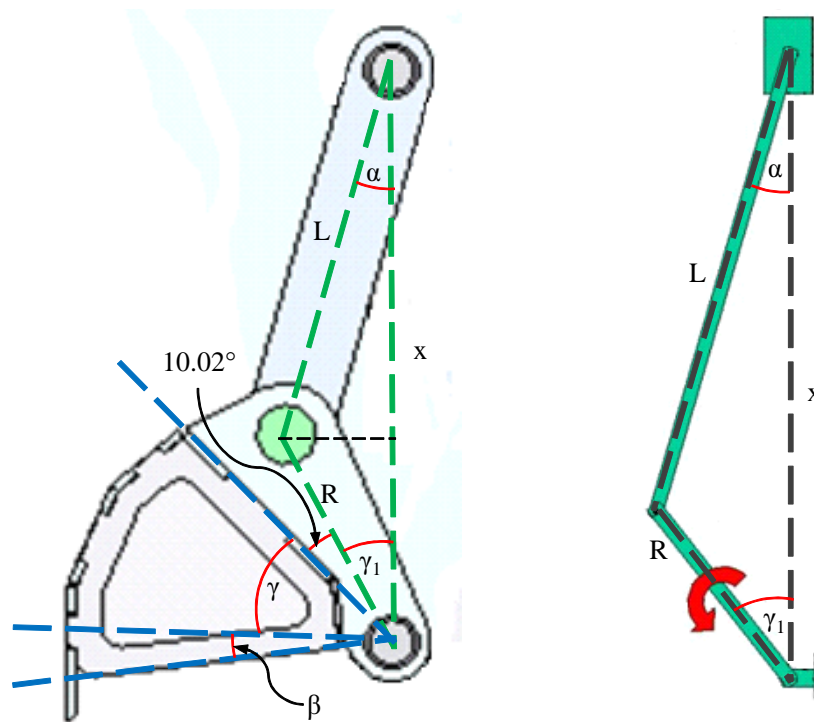
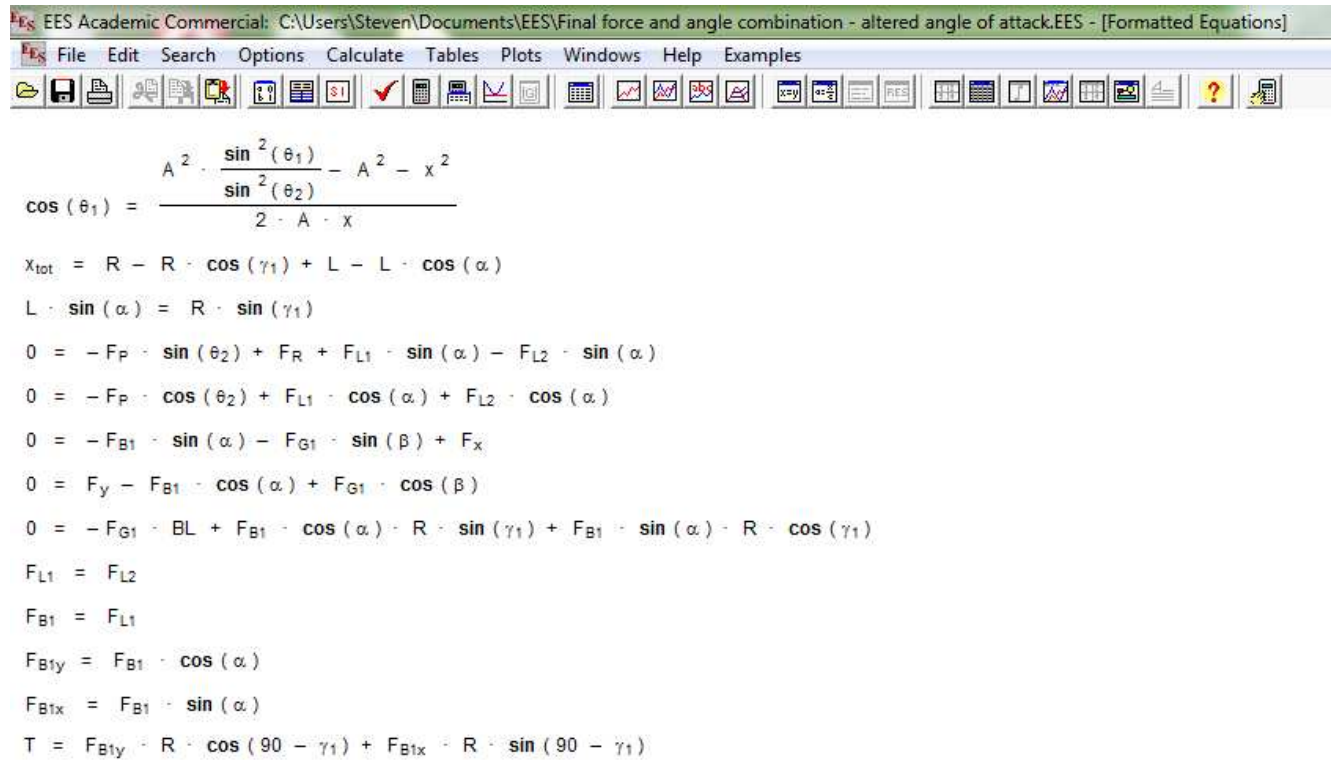


Figure 7.5: The relationship between  $x$  and the bucket angle.

Table 7.1: Systems constants

Constant	Value	Unit
L	0.220	m
R	0.135	m
A	0.465	m
$\ell$	0.190	m
$\theta_1$	13.0	deg
$\beta_{ini}$	16.0	deg
$\gamma_{ini}$	36.7	deg

## Formatted EES Equations



EES Academic Commercial: C:\Users\Steven\Documents\EES\Final force and angle combination - altered angle of attack.EES - [Formatted Equations]

File Edit Search Options Calculate Tables Plots Windows Help Examples

$$\cos(\theta_1) = \frac{A^2 \cdot \frac{\sin^2(\theta_1)}{\sin^2(\theta_2)} - A^2 - x^2}{2 \cdot A \cdot x}$$

$$x_{\text{tot}} = R - R \cdot \cos(\gamma_1) + L - L \cdot \cos(\alpha)$$

$$L \cdot \sin(\alpha) = R \cdot \sin(\gamma_1)$$

$$0 = -F_P \cdot \sin(\theta_2) + F_R + F_{L1} \cdot \sin(\alpha) - F_{L2} \cdot \sin(\alpha)$$

$$0 = -F_P \cdot \cos(\theta_2) + F_{L1} \cdot \cos(\alpha) + F_{L2} \cdot \cos(\alpha)$$

$$0 = -F_{B1} \cdot \sin(\alpha) - F_{G1} \cdot \sin(\beta) + F_x$$

$$0 = F_y - F_{B1} \cdot \cos(\alpha) + F_{G1} \cdot \cos(\beta)$$

$$0 = -F_{G1} \cdot BL + F_{B1} \cdot \cos(\alpha) - R \cdot \sin(\gamma_1) + F_{B1} \cdot \sin(\alpha) - R \cdot \cos(\gamma_1)$$

$$F_{L1} = F_{L2}$$

$$F_{B1} = F_{L1}$$

$$F_{B1y} = F_{B1} \cdot \cos(\alpha)$$

$$F_{B1x} = F_{B1} \cdot \sin(\alpha)$$

$$T = F_{B1y} \cdot R \cdot \cos(90 - \gamma_1) + F_{B1x} \cdot R \cdot \sin(90 - \gamma_1)$$

Figure 7.6: Formatted EES equations.

## Appendix B - Hydraulic Cylinder Parameters

There are no constitutive relationships describing the forces required to penetrate a granular bed with an irregularly shaped object. Hence, it was difficult to estimate hydraulic cylinder capacities required to ensure that the buckets would be able to penetrate the material. To circumnavigate this problem the cylinder capacities were inferred using experimentation. This comprised using a blunt object (a section of channel iron) to penetrate a reservoir of material using a Schenck servo-hydraulic testing machine, located in the laboratory of the School of Mechanical, Aeronautical and Industrial Engineering.

An actuation system, a control and monitoring system, a section of channel iron of dimension  $100 \text{ mm} \times 60 \text{ mm} \times 5 \text{ mm}$ , a reservoir to hold the material and the material itself formed the experimental apparatus. The material reservoir and material comprised a halved oil drum and 13 mm gauge building stone respectively. The Schenck hydraulic press and Moog control system were used to produce the penetrating force and control the kinematics of the digging tool respectively. The latter item also served to capture the data during experimentation.

Figure 7.7 illustrates the set-up for the experimentation.

The penetrating object had a constant stroke of 95 mm for all penetrating velocities. The general methodology for testing took place in the following sequence:

1. The Schenck Hydraulic press was activated, and the control program initiated. The control software was set to measure force with respect to displacement.
2. The penetrating tool was clamped to the hydraulic press by means of hydraulic gripping jaws on the Schenck machine.
3. The reservoir was placed on the Schenck stand.
4. The Schenck control software was set up with the correct input parameters, i.e the desired velocity profile, the acceleration and deceleration of the penetrating object. All parameters except for the penetrating speed were identical for all the tests.
5. The blunt tool was moved into the material at a speed of 2mm/s. The object was accelerated to full speed before it entered the material. It was then withdrawn from the material.

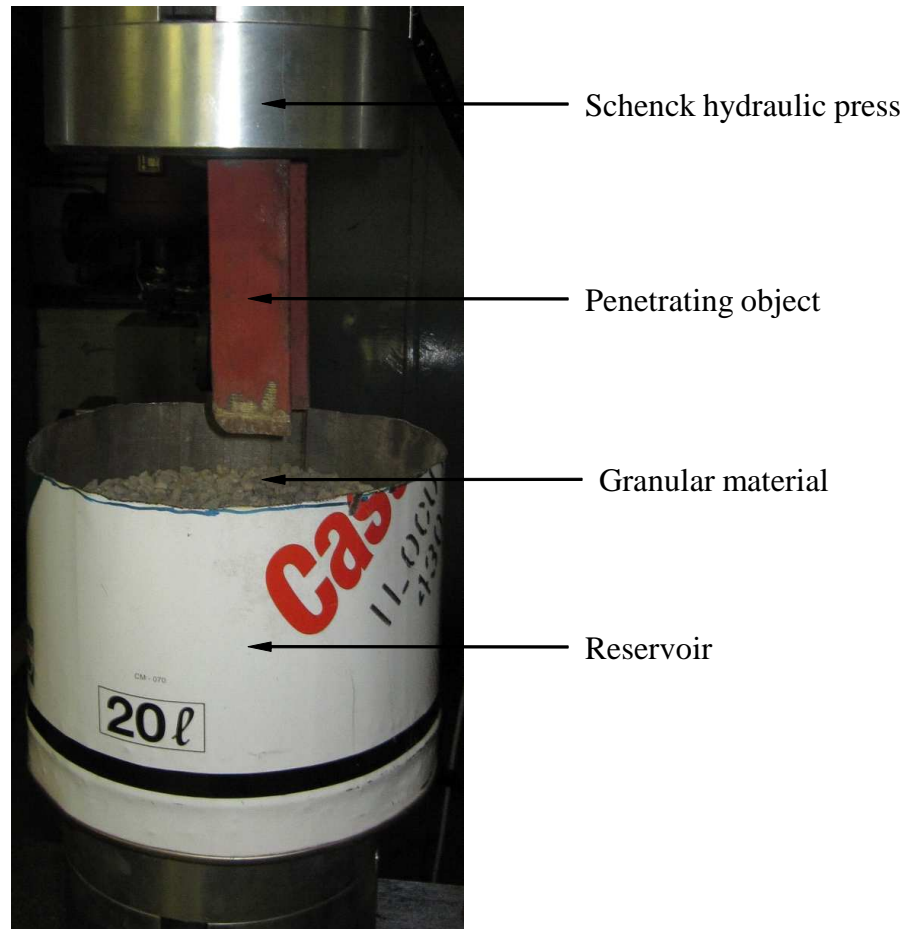


Figure 7.7: Illustration of the experimental set-up to size the hydraulic cylinders.

6. After each cycle, the reservoir was removed from the stand, and the material manually agitated (by shaking the container) so that it did not become compacted.
7. Items 1 to 6 were repeated 6 times.
8. The previous steps were repeated for velocities of 20mm/s, 40mm/s and 80mm/s.

Beyond a depth of 60 mm it was deemed that the proximity of the bottom boundary was responsible for the sudden increase in the penetrating force, due to congestion.

Figure 7.8 illustrates the variation of load with depth for a penetration velocity of 80 mm/s.

The variation of averaged maximum loads with penetration velocity are shown in Figure 7.9.

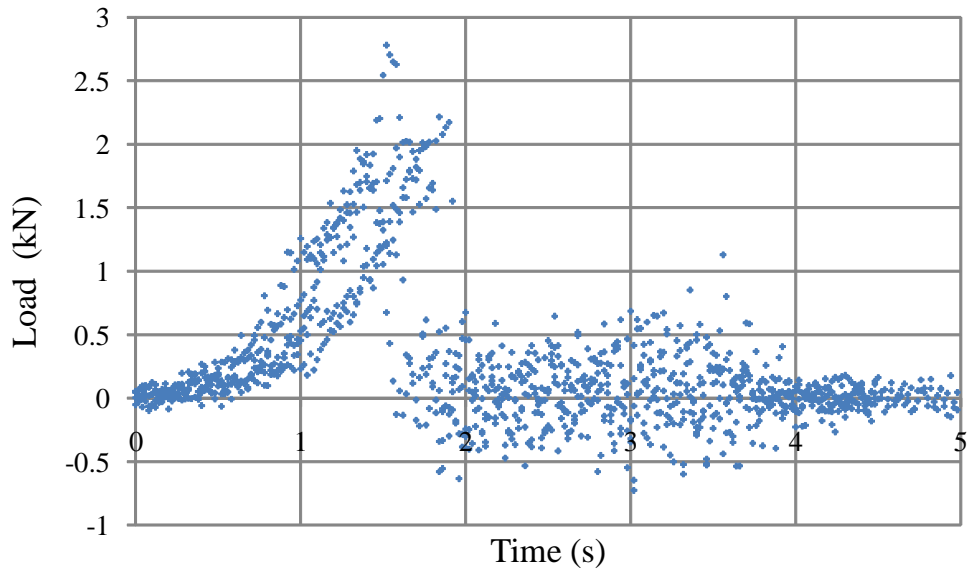


Figure 7.8: Variation of load with time for a penetration velocity of 80mm/s.

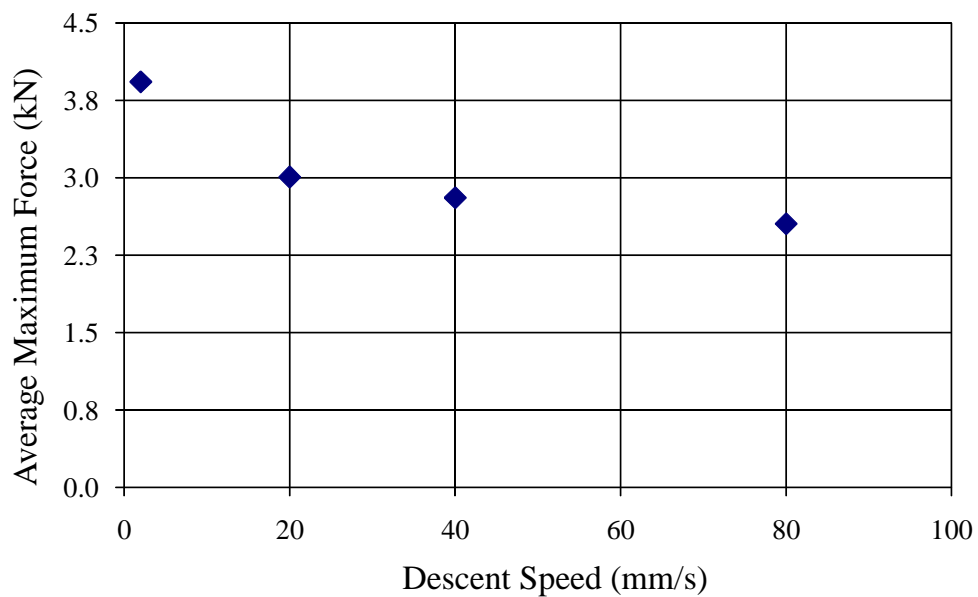


Figure 7.9: Variation of average maximum load with descent speed.

It is seen from Table 2.1 in Section 2.1.3 that the maximum force recorded was 4.7 kN. This value was substituted as the value for  $F_{G1}$  in equation 7.6. Using EES and the eight non-linear simultaneous equations derived in Appendix A, the corresponding force exerted by the cylinder would be 9 kN. This value was then used as a basis for selecting the size of the hydraulic cylinders.

## Appendix C - Detailed Description of Test facility

### Stationary Base

The stationary base (see Figure 7.10) consists of six 8 mm steel plates, laser cut with alignment faces and holes, to simplify the manufacturing thereafter. The slider assembly is also shown in Figure 7.10

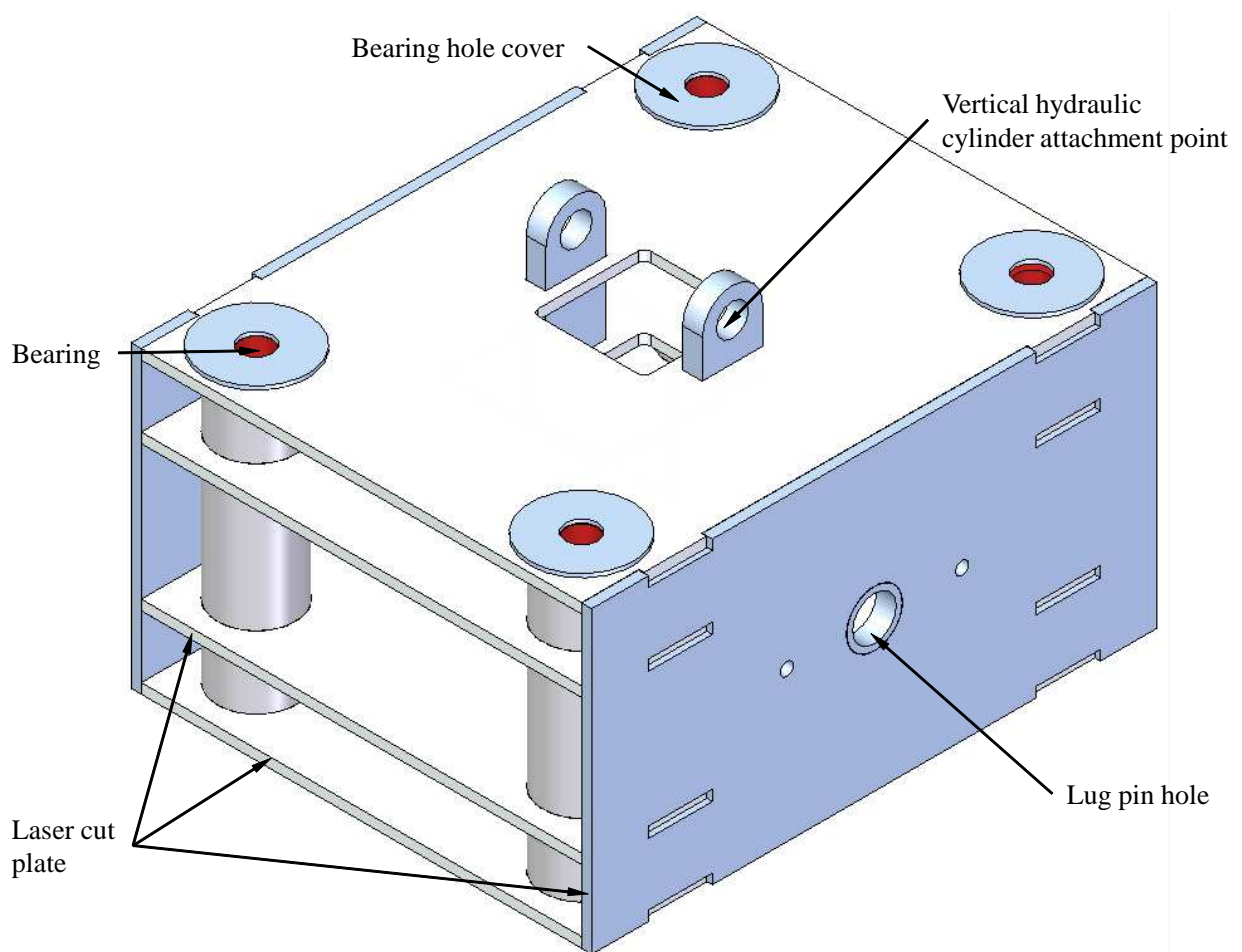


Figure 7.10: Illustration of the stationary base assembly.

The stationary base forms the primary vertical positioning mechanism of the rig; hence it was important to ensure that the four guide rods were perfectly aligned within the bearings of the slider assembly. The correct alignment was achieved using thick walled honed steel tubing (62 mm × 54 mm) as bearing cylinders. The six plates forming the foundation of the stationary base (see Figure 7.11) were assembled and welded together. Thereafter the ends of each of the thick walled tubes were turned out independently, removing a small amount of material and leaving a small

shoulder. A vesconite bush was created, by turning the material until it was a sliding fit. It was placed against the shoulder and retained by welded cover plates (to keep it from being displaced during the digging operation).

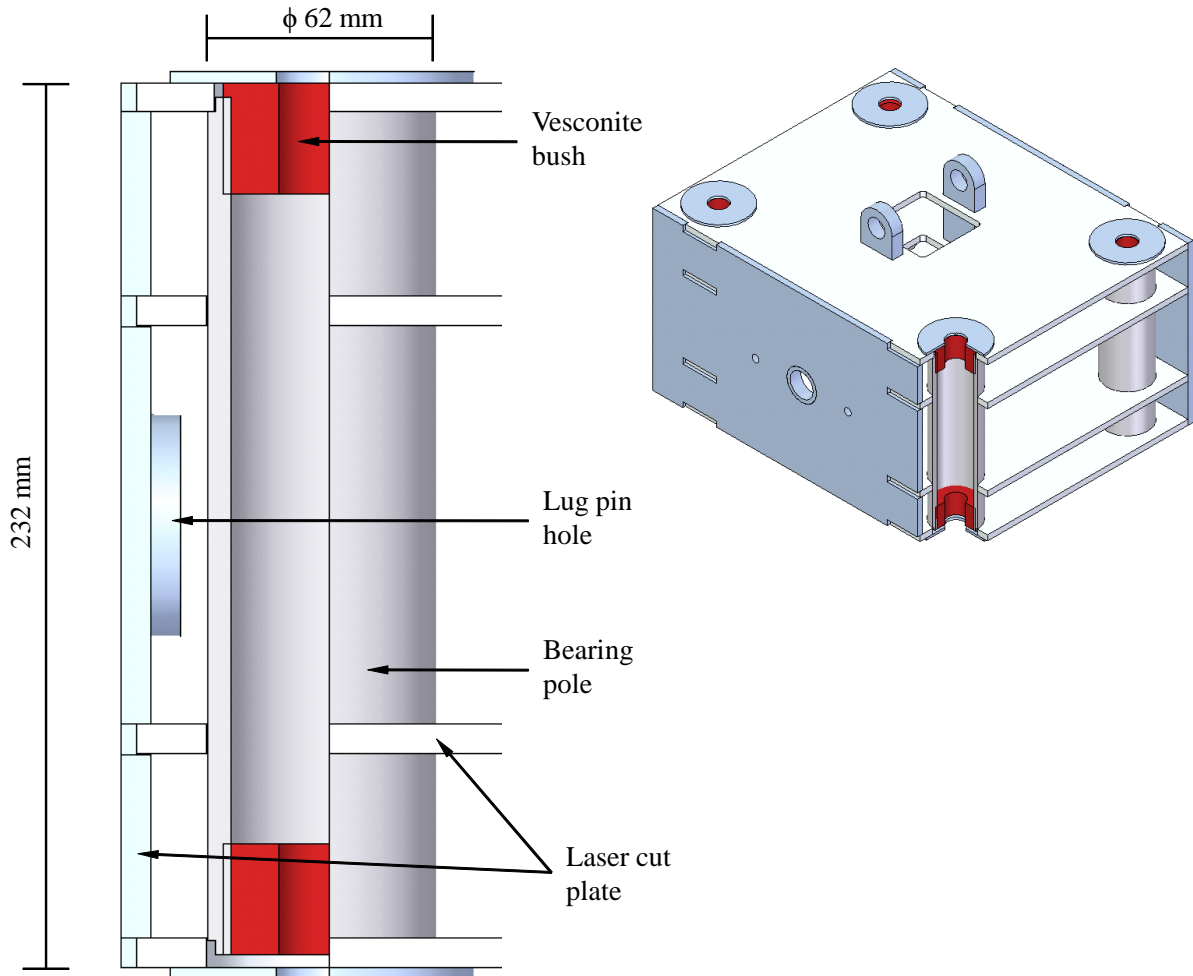


Figure 7.11: An illustration of the bearing assembly.

## Main Body Assembly

The main body assembly (see Figure 7.12) consists of two 10 mm laser cut plates which are held with the requisite distance apart by four strengthening supports made of thick walled tubing. The guide rods are welded into holding blocks (made of 50 mm  $\times$  50 mm square bar) which in turn are welded on to the exterior surface of the two plates.

Each half of the clamshell bucket sides and the linkages attaching them to the cylinder were produced from laser cut steel plate. The linkages are 10 mm thick, while the plates making up the



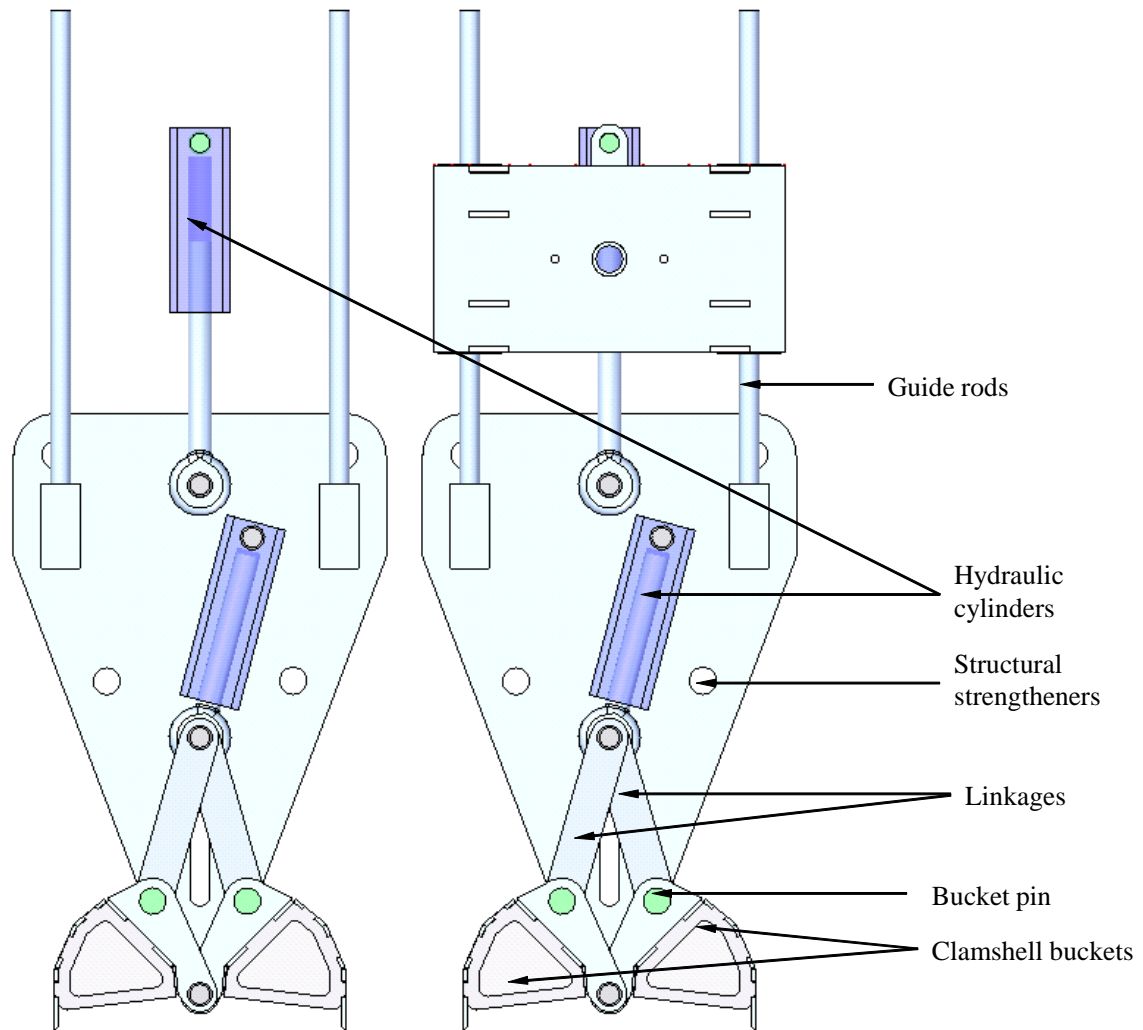


Figure 7.12: Illustration of the main body assembly.

clamshell jaws are 5 mm in thickness. Each bucket half is made from plate cut specifically to fit together (laser cut with alignment faces and holes), for simplicity of assembly. The bottom plate forming the teeth has been cut at an angle of  $45^\circ$  in order to improve the penetration ability. Figure 7.13 illustrates the clamshell configuration.

### The Muck box and Frame Assembly

As mentioned previously, the dimensions of the muck box were based on the those of the clamshell. The clamshell's width, height and depth when open are  $300 \text{ mm} \times 150 \text{ mm} \times 250 \text{ mm}$  and when closed are  $245 \text{ mm} \times 188 \text{ mm} \times 250 \text{ mm}$ , hence the material reservoir's dimensions are  $2000 \text{ mm} \times 750 \text{ mm} \times 800 \text{ mm}$ .

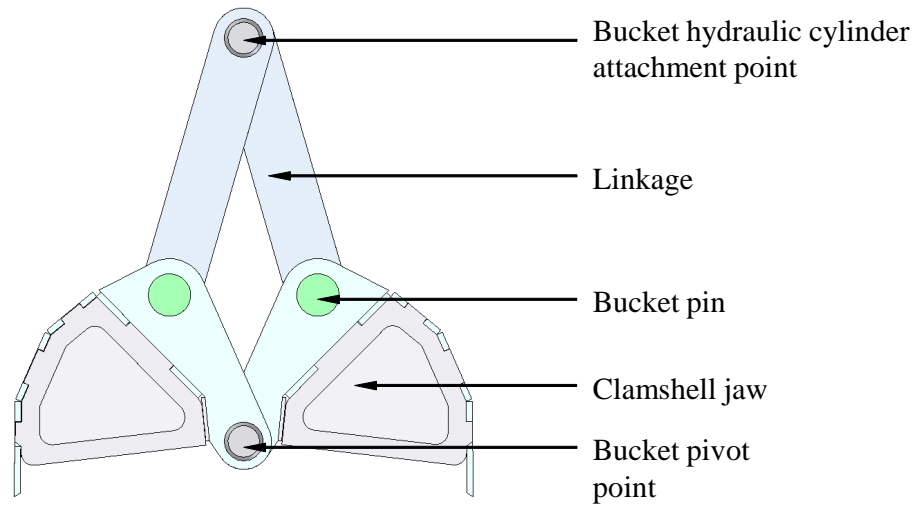


Figure 7.13: Illustration of the clamshell configuration.

The muck box (see Figure 7.14) was designed with a portal or window so that a visual representation of the granular flow during the digging motion could be observed. The dimensions of the window were 550 mm  $\times$  1000 mm.

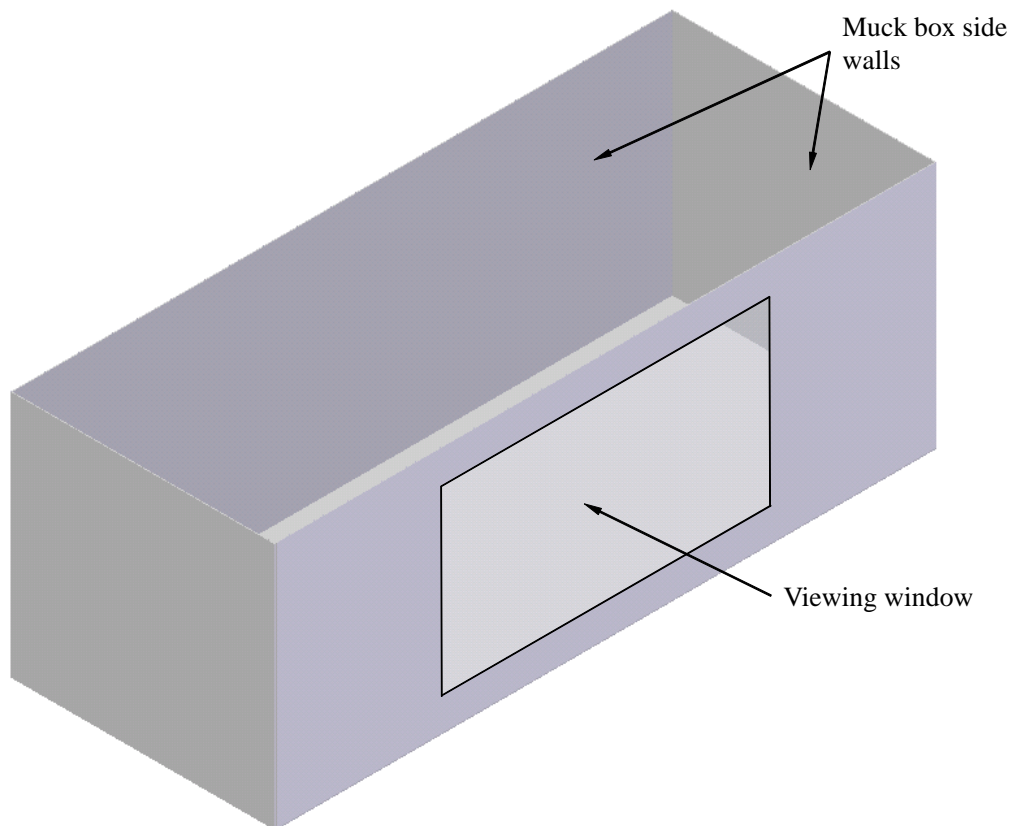


Figure 7.14: Illustration of the muck box.

The frame of the rig was designed to maximise both stability and visibility (see Figure 7.15). It comprises twelve lengths of 120 mm × 50 mm standard tapered C-Channel, making up the legs, the feet, the cross members and the support structures. Holes were drilled into the feet so that the frame could be raw bolted to the floor. The frame was also bolted to the wall to afford the structure extra stability.

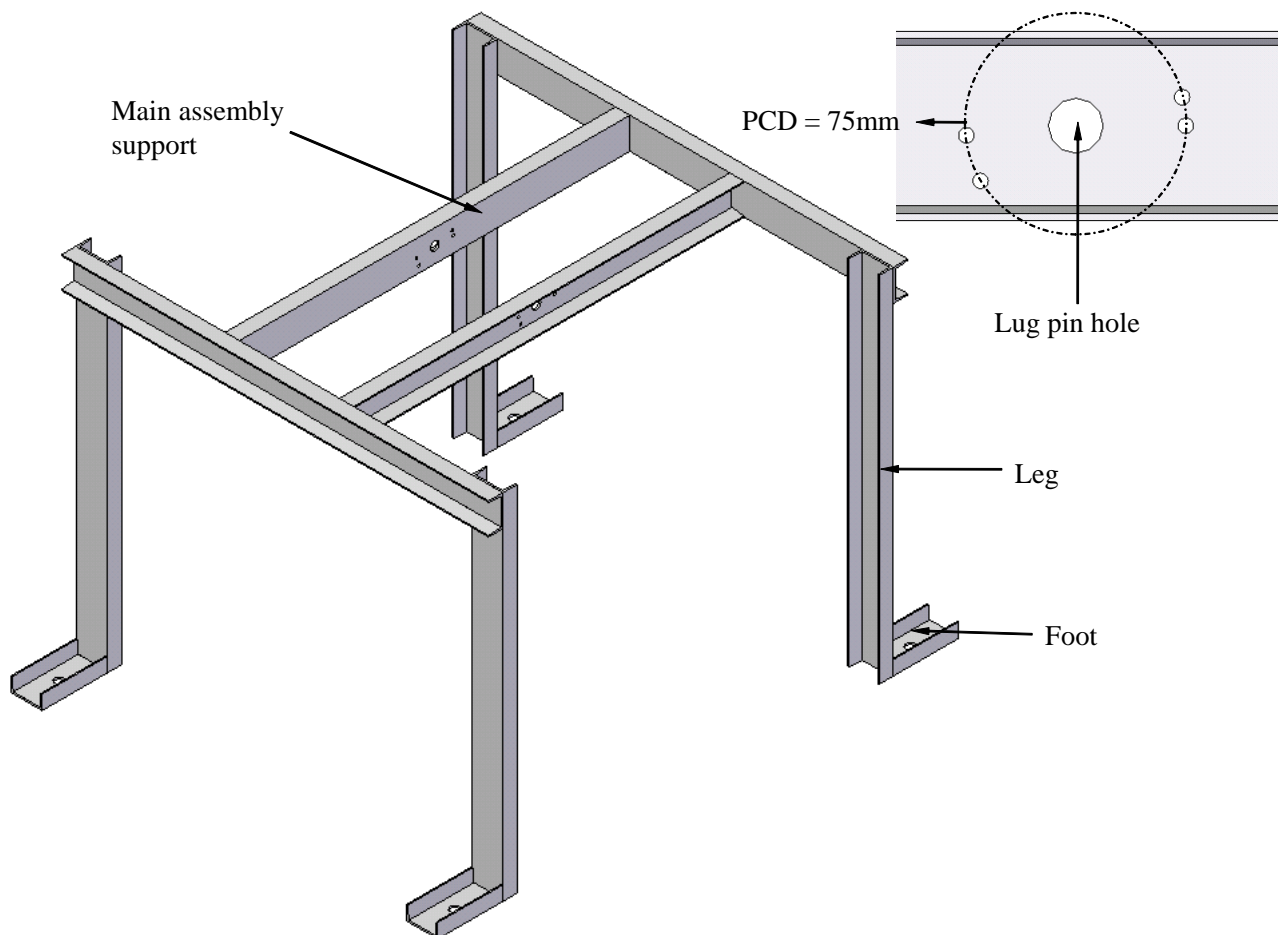


Figure 7.15: Illustration of the assembly frame.

## Hydraulic Circuit

Figure 7.16 represents a schematic of the hydraulic circuit and Table 7.2 the associated parts.

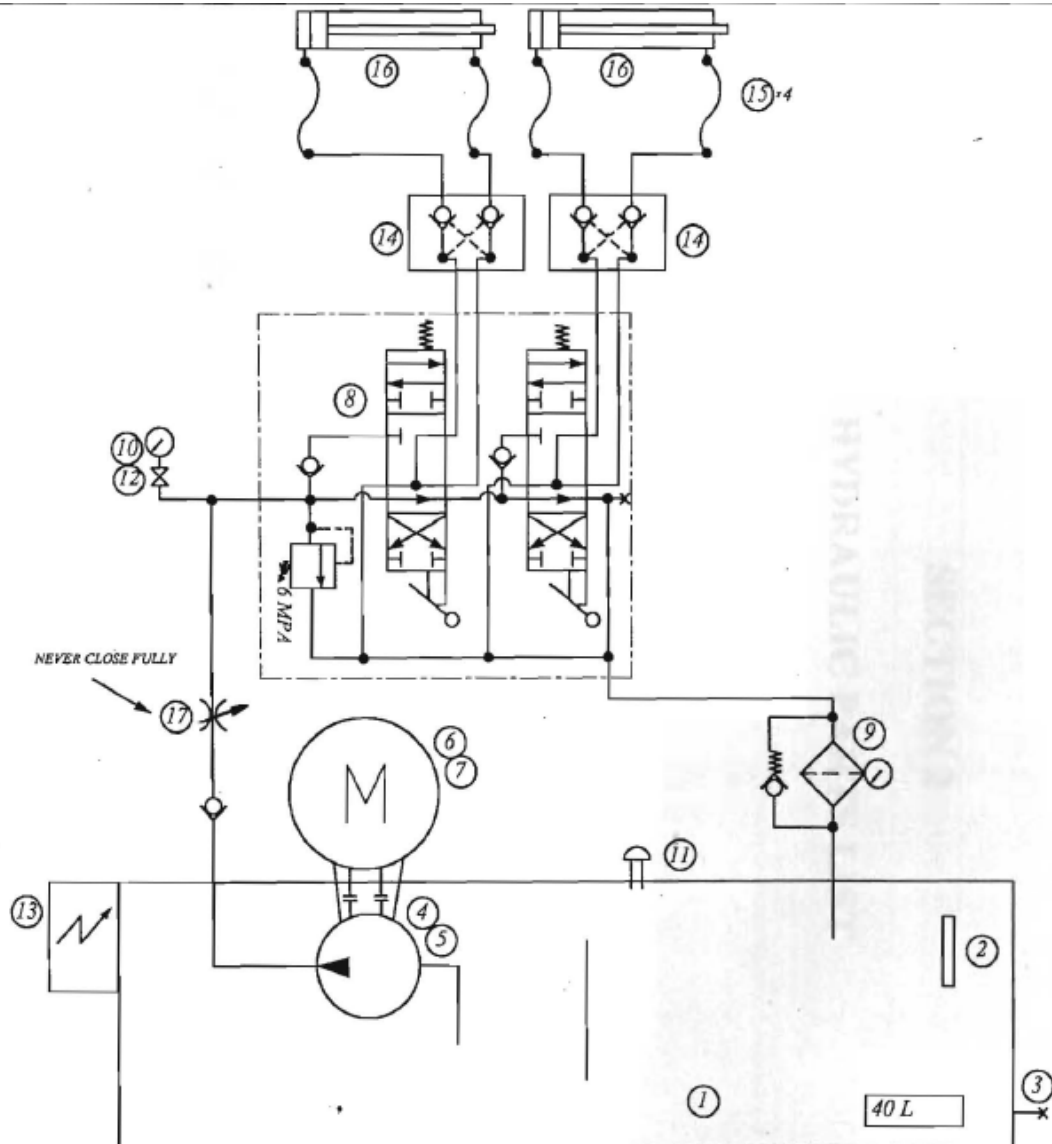


Figure 7.16: Schematic of the hydraulic circuit.

Table 7.2: List of parts for the Hydraulic Circuit

Parts List - For Power Pack - Wits University			Job No. 811119
REF:DRAWING NO: D-1898			Sheet
ITEM	DESCRIPTION	QTY	PART NUMBER
1	Oil Reservoir	1	40 ℓ MINING TYPE+ SHORT BOTTLE
2	Oil level Gauge/Therm	1	HL91-20T1-T-B
3	Drain valve + plug	1	3/4"L.P.BALL VALVE + GALV.PLUG
4	Oil pump	1	PLP10.4.D0-81E1-LGC/GC-N
5	Flex. Drive coupling	1	GE 19-81
6	Electric Motor	1	0,75/220VAC/4-P/Flange only
7	Bellhousing	1	LF200 E1
8	Dual Lever Valve	1	SD5/2-P(KG3-220)/28L/284-AET
9	Return Oil Filter	1	HF550-20-077-AS-FG010-B17-GE-P-G
10	Pressure Gauge	1	DN63/BOTT./0-160 BAR
11	Oil Filler/Breather	1	HB70-FERMEL
12	Gauge Isolator	1	FT 290-14
13	D.O.L Starter	1	TELEMECANIQUE 0,75Kw/220 VOLT
14	Dual P.O. Check Valve	2	VBPDL38/P4
15	Flexible Hose Valve	4	3m LONG/1/4" SINLGE WIRE/8L SW.NUT Each END
16	Hydraulic Cylinder	2	AGRICULTURAL 50/30/200/F.C/F.C

## Instrumentation

Various items of instrumentation were required to obtain the necessary data during experimentation. These items of instrumentation included pressure transducers, a linear and angular potentiometers as well as a Data Acquisition system. The instrumentation was calibrated as described in Appendix E.

The pressure transducers selected were WIKA products; A-10, 0-100 bar pressure transducers, serial number 0012619JK9.

The pressure transmitters output a current instead of a voltage, as required by the DAQ system. This was achieved by adding a resistor in the input line to the Data Acquisition (DAQ) system. The pressure transducers were rated for a pressure of 0 - 100 bar, with corresponding maximum output currents of 19.979 mA and 19.975 mA for the vertical cylinder and bucket cylinders respectively. The DAQ was rated for the voltage range of -10 V - 10 V; therefore the resistors needed a resistance  $\geq 500\Omega$ , to be within this range for the entire expected current output. Appropriate resistors were chosen, of value 555  $\Omega$  and 554  $\Omega$  for the vertical cylinder and bucket cylinder respectively.

Two separate positions needed to be measured simultaneously: the vertical motion of the bucket into the material, and the opening and closing of the bucket. Therefore two different measurement devices were required, one for the linear position and one for the angular position of the bucket during the cycle. A linear potentiometer was selected to measure the linear position of the bucket, (UniMeasure linear potentiometer, model number PA-10-NJC-P10K-L3M, serial number 40080212), and an angular potentiometer was used to measure the angle of the bucket during the motion (a standard  $1k\Omega$  potentiometer).

The Data Acquisition system chosen was a National instruments USB-6009, 14 bit, 48 kcycle/s DAQ with 8 analog and digital inputs.

### Instrumentation Wiring Diagrams

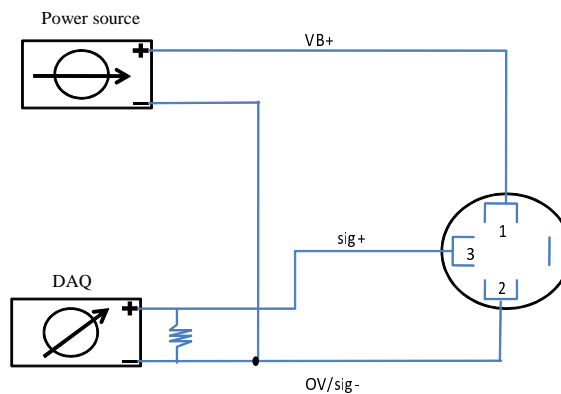


Figure 7.17: An illustration of the wiring diagram for the pressure transducers.

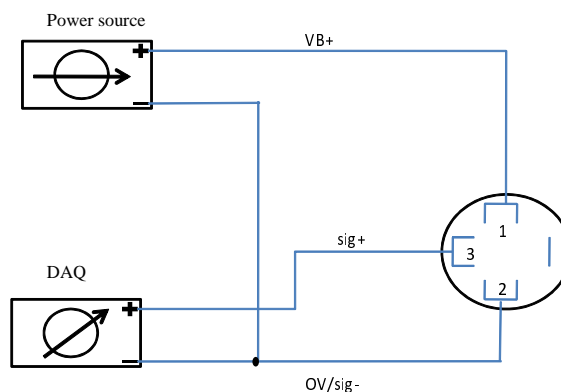


Figure 7.18: An illustration of the wiring diagram for the angular and linear potentiometers.

## Appendix D - Input Parameters and Sensitivity Analysis

### Static Friction

Three materials required testing in the current context; steel (forming the buckets of the rig and the reservoir walls), the gravel material (a standard 13 mm gauge decomposed granite stone) and polycarbonate (the front windows of the box and jaws).

The experimental apparatus comprised:- three interchangeable flat plates (steel, polycarbonate and decomposed granite) that could be inclined as required, a bubble inclinometer, and a non-spherical sample of the granular material.

The testing procedure was as follows:

1. The steel flat plate was positioned horizontally.
2. A sample of the crushed material was placed on the plate.
3. The plate was slowly tilted until the sample of material began to slide.
4. The angular position of the plate relative to the horizontal was measured using the bubble inclinometer (the tan of this angle formed the frictional coefficient).
5. The experiment was repeated 15 times and the average result was used.
6. The above steps were repeated using the flat polycarbonate plate and subsequently the flat piece of decomposed granite.

Thereafter a DEM program was used to emulate these experiments, to ensure that the the physical and numerical properties of the materials matched one another. An identical experimental set up was created in the program, with a flat plate tilting until the sample began to slide and the angle was noted. In order to generate a “flat” side of granite that would not roll, three spherical particles were connected together (see Figure 7.19), to encourage a sliding rather than rolling motion. The angle derived from physical experimentation was used in the model to see if the physical experimentation correlated well with the numerical model. Figure 7.19 illustrates the DEM model.

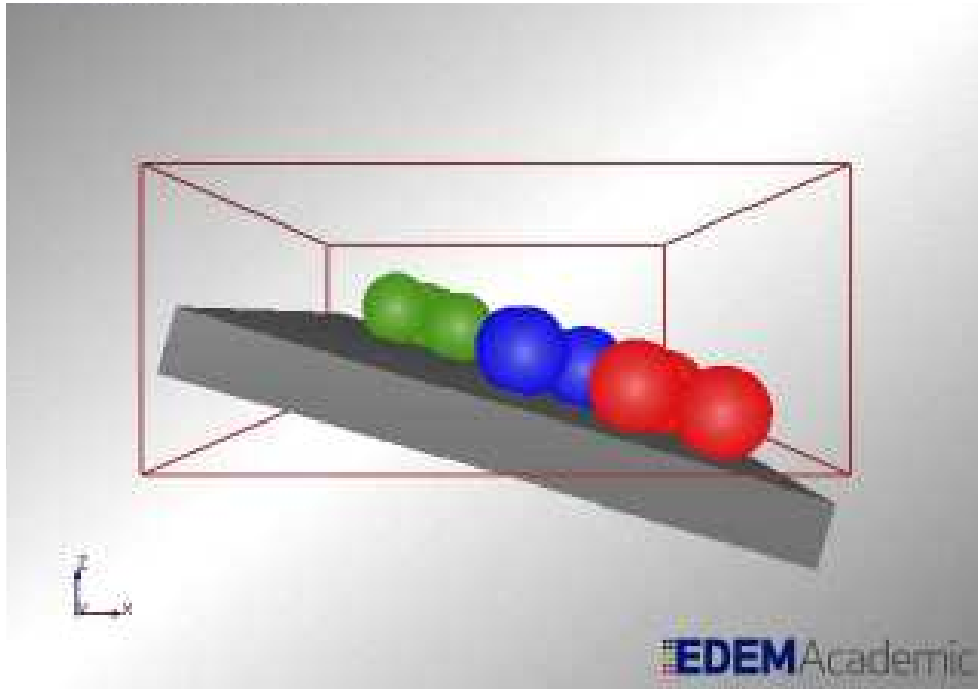


Figure 7.19: DEM model for the friction test using triangular particles.

The results indicate that the polycarbonate had the lowest static friction coefficient, whilst granite was found to have the highest value, these parameters matched well with the published data values (see Table 3.1). Furthermore, the DEM simulation showed that all the particles began to slip at almost exactly the same angle as in the physical experiments for the given materials. Thus the static friction values obtained from experimentation were deemed appropriate to be used in the DEM simulations.



## Rolling Friction

Three materials required testing in this context: steel making up the buckets and the reservoir walls, standard 13 mm gauge decomposed granite stone (the granular material), and polycarbonate for the viewing window of the box and jaws.

The basic experimental apparatus comprised three long flat (as far as was possible) plates (composed of steel, granite and polycarbonate), an inclined plane (of ramp height 5 mm) and a particle (made as spherical as possible) of decomposed granite stone.

The testing method was as follows:

1. It was ensured that the surface upon which the experiments took place was level.
2. The gravel particles were rolled down the ramp.
3. The distance travelled by the particle was measured. The ratio of ramp height to distance travelled defined the coefficient of rolling friction.
4. The previous two steps were repeated 15 times and the average result was used.
5. The above steps were repeated using a flat plate composed of decomposed granite and polycarbonate thereafter.

The results from the experiment were not definitive, displaying a lack of repeatability among the results, and deviating from published data values (see Table 3.1). Because the results obtained were deemed to be inaccurate, published data values were acquired and employed in the simulations instead.

## Co-efficient of Restitution

Apparatus for the experimentation comprised:- a wooden frame, a sample of the granular material (made as spherical as possible<sup>1</sup>, a large flat section of the second test material (i.e steel, granite or polycarbonate), a microphone and a sound recorder.

The experimental methodology was as follows;

1. The wooden frame with the flat steel section attached was placed on a level surface.
2. The granite was held up at a specific height.
3. The granite particle was dropped from rest towards the second test material (in the first case steel).
4. It would bounce off the flat plate and continue to rebound until it came to a rest.
5. The microphone was positioned in such a way so as to capture sound emanating from the particle as it rebounded off the test surface.
6. A program called *Audacity*© was used to read the audio file.
7. The time between each impact was then established using the above mentioned software, and thus used to evaluate the coefficient of restitution.
8. The above steps were repeated using a flat section comprising the other test materials (i.e. granite and polycarbonate).

This method of testing and analysis was obtained from Sim (2010). The time of flight between each bounce was plotted against the bounce number ( $n$ ). Thereafter the logarithm of the time of flight was plotted against  $n$  and a linear least squares regression analysis applied (see Figure 7.20). The coefficient of restitution was obtained from raising the gradient of the least squares regression line to the power of the natural logarithm.

---

<sup>1</sup>Initially an attempt at creating or locating a spherical sample of a decomposed granite particle was made; however this proved to be difficult. No commercial benefit can be derived (as far as the author could find in extensive searches) from creating spherical decomposed granite samples. Hence an effort was made to create a sphere. A granular element was cut with a diamond tipped cutting disc to try and emulate a spherical shape. This proved to be unsuccessful; nevertheless, testing was still conducted.

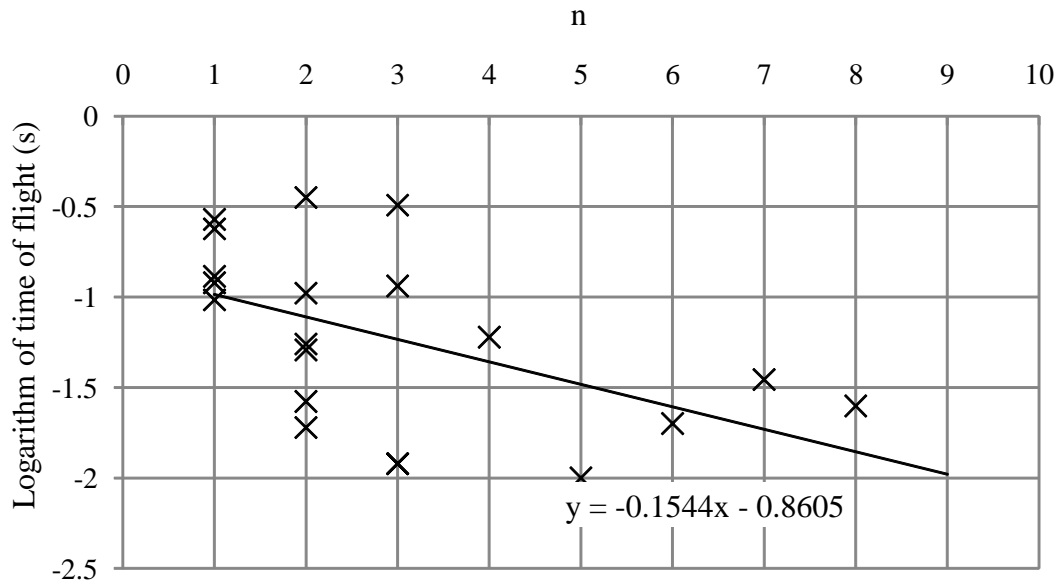


Figure 7.20: Variation of time of flight with bounce number for granite on steel.

From Figure 7.20 it is seen that there is a large variability in the values between successive tests. This gave an average result that was 50% lower than values found in the literature. Hence, as with the coefficient of rolling friction these results were ignored and published data was used instead. The average experimental data and the corresponding published values for the coefficients of restitution may be found in Table 3.1.

## Sensitivity Analysis

A sensitivity analysis was performed to ascertain the effects of the various input parameters on a DEM model. A simplified DEM model was used to achieve this aim, using a simple flat plate entering a round container of granular particles. The least possible number of particles were used to minimize computation time (see Figure 7.21).

A base model was initially used with the coefficients of rolling friction and restitution having published values (as outlined in Table 3.1), and static friction having values derived from experimentation. Thereafter a single parameter at a time was adjusted. The coefficient of static friction, rolling friction and restitution were altered by +30%,  $\pm 50\%$  and -17.3% respectively. The variation of force with penetration depth was then plotted for each of these cases, the results of which may be viewed in Figure 3.1.

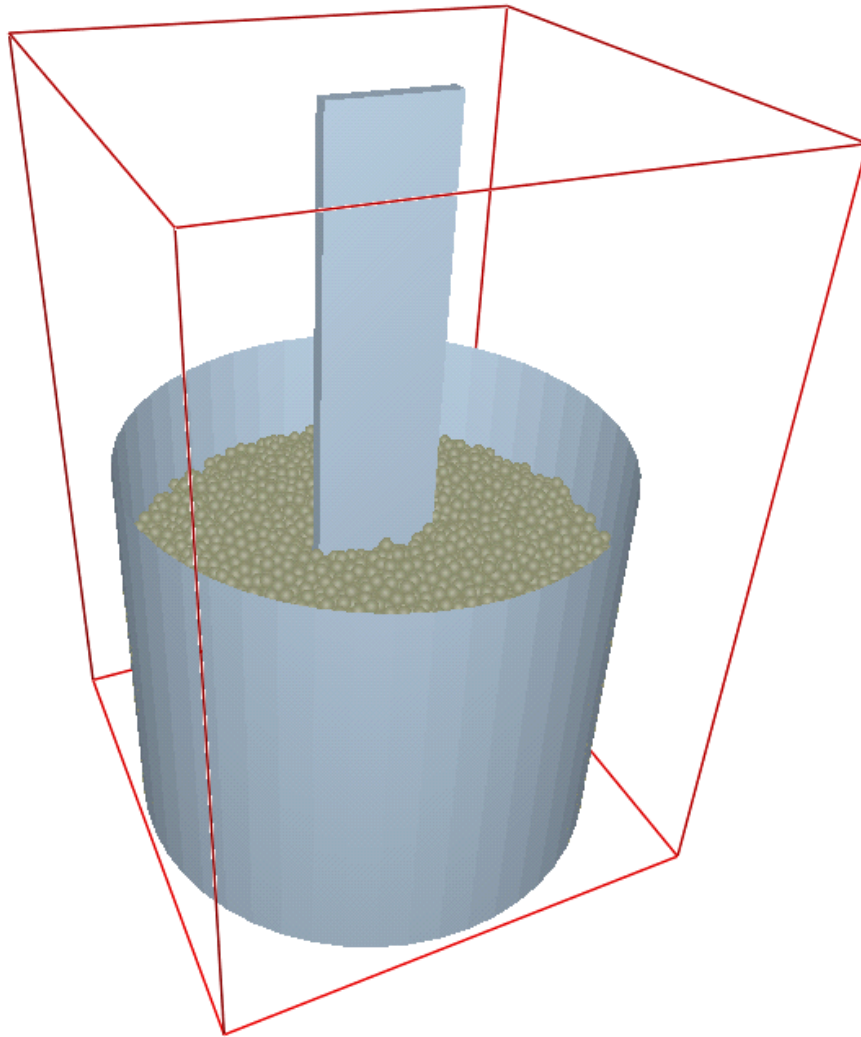


Figure 7.21: DEM geometry setup for the sensitivity analysis.

## **Appendix E - Calibration of Angular Potentiometer; Base Loading**

### **Calibration**

Before the commencement of experimentation it was necessary to calibrate various components of the system. These are described in the following subsections, excluding the pressure transducers and linear potentiometer that had manufacturers' data sheets.

However, the angular potentiometer needed to be calibrated through experimentation. Simultaneously it was necessary to gauge the impact (on the measured readings) of such things as the weight of the rig, stiction due to the seals and other internal cylinder effects, these would not be present in the DEM simulations.

### **Angular Potentiometer**

Prior to testing it was necessary to generate a calibration curve for the angular potentiometer - to ensure that voltage readings correlated with known angular positions of the bucket. The method used was as follows: the reading of the initial position of the bucket was generated as a voltage. The bucket position was then incrementally rotated (approximately  $10^\circ$  at a time), for which each angle was physically measured and recorded using a bubble inclinometer, together with the corresponding voltage readings (see Figure 7.22).

As mentioned previously, calibration data sheets for the pressure transducers and the linear potentiometer were provided with the respective items. The calibration curves for these and their corresponding equations are given in Figures 7.23, 7.24 and 7.25.

### **Control Valve**

It was required to be able to choose the control valve position to give required clamshell bucket closing velocities. For this purpose, various velocities were generated by altering the amount the control valve was opened, giving initially the variations of bucket angular displacement with time

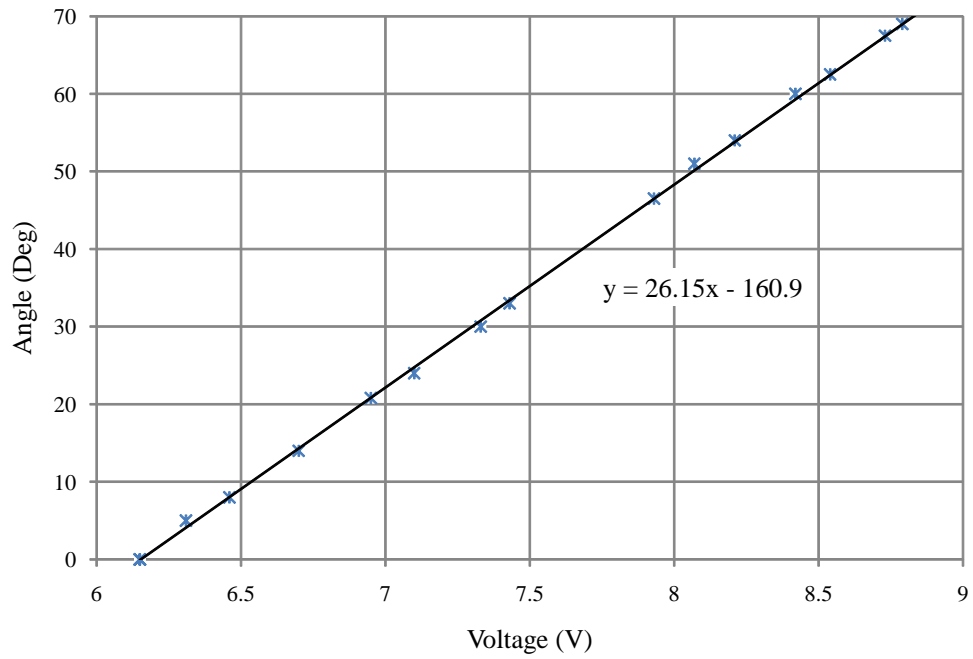


Figure 7.22: Calibration curve for the angular potentiometer.

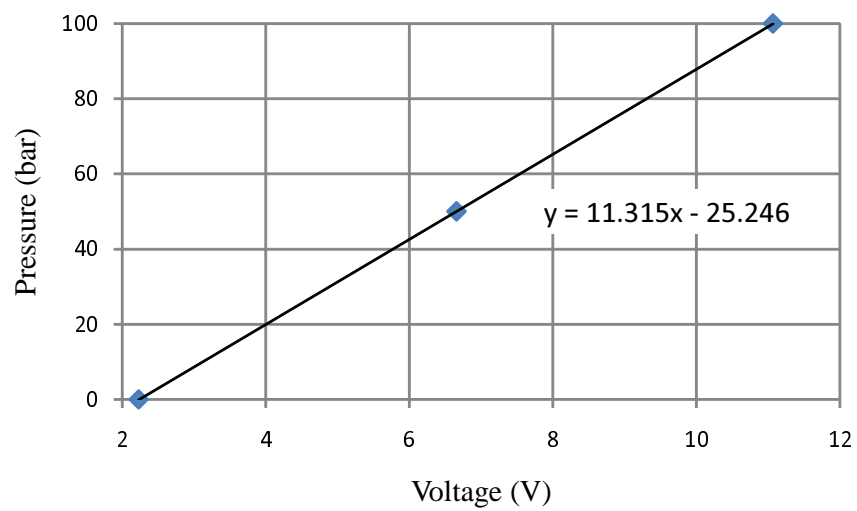


Figure 7.23: Calibration curve for the bucket operation pressure transducer.

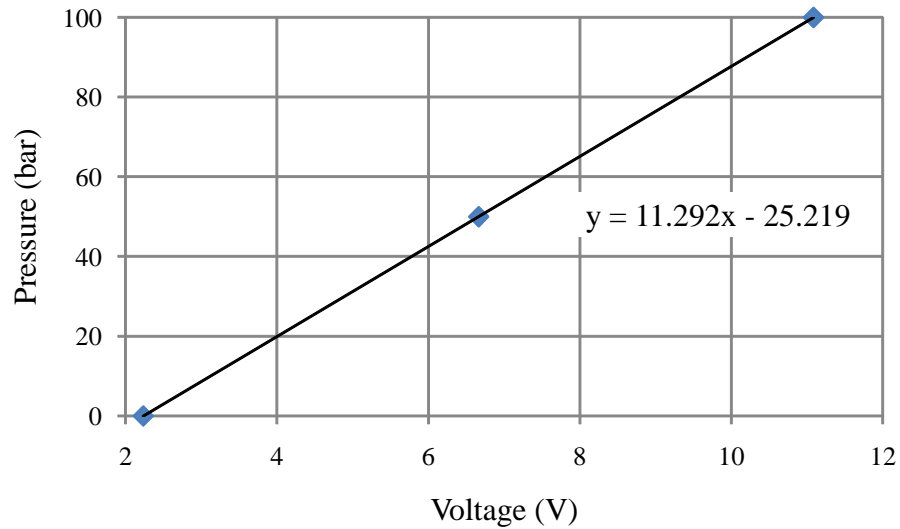


Figure 7.24: Calibration curve for the vertical motion pressure transducer.

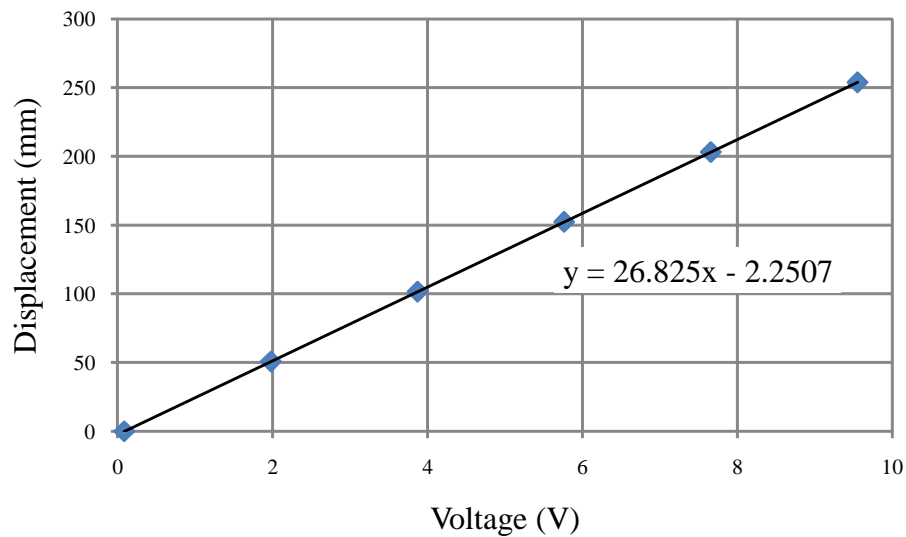


Figure 7.25: Calibration curve for the linear potentiometer.

for various control valve settings, as given by lever displacement from a fixed datum (see Figures 7.26 to 7.28).

## Base Loading of Actuator

From the outset it was decided to ascertain the base loading on the cylinders, excluding the forces arising from the granular material - accounting for stiction, friction, the weight of mechanical components, etc. This was accomplished by testing without a load - i.e. free-air testing where

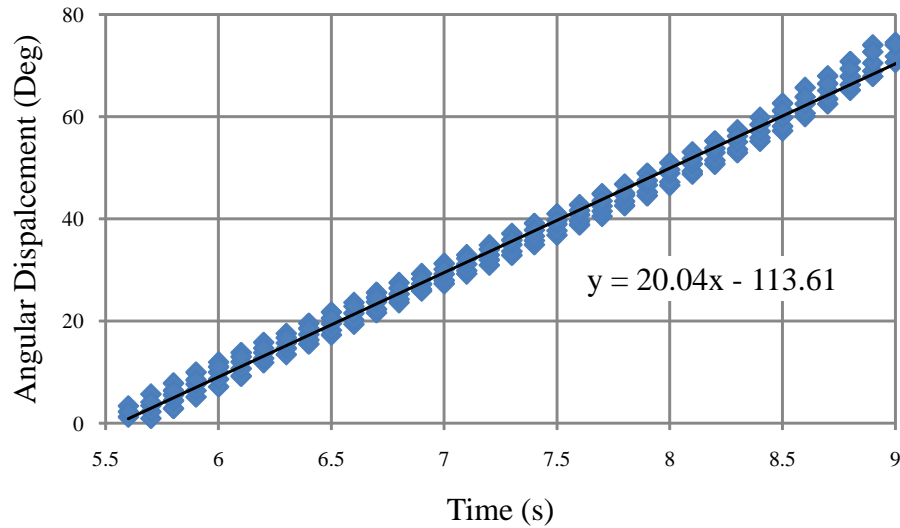


Figure 7.26: Variation of bucket angular displacement with time for a 20 deg/s closing velocity.

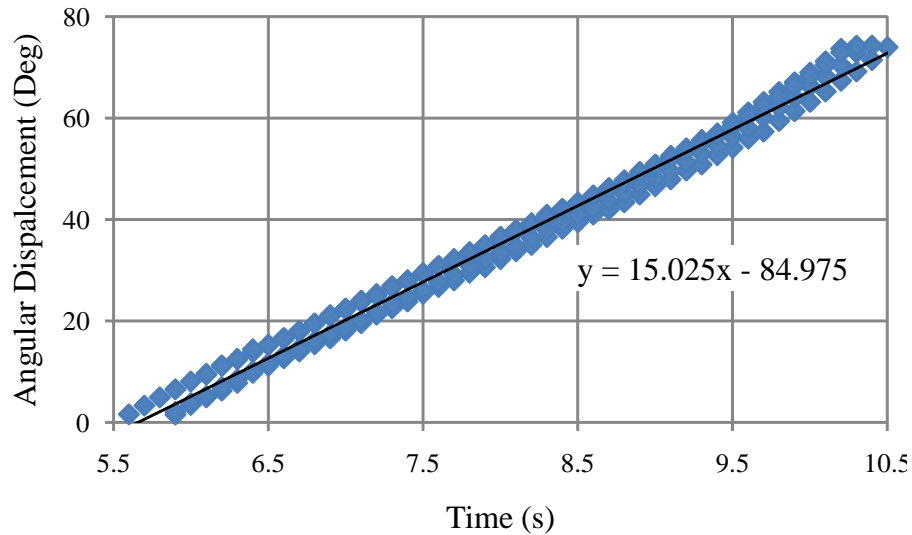


Figure 7.27: Variation of bucket angular displacement with time for a 15 deg/s closing velocity.

the clamshell does not penetrate the granular material. The testing methodology was similar to that of the formal experimentation (detailed in Section 4.2), where the system was tested at three different bucket closing velocities: 20 deg/s, 15 deg/s and 10 deg/s, with each velocity experiment being repeated 15 times to ensure experimental consistency. The actuator forces at each bucket position were then inferred using pressure transducers positioned in the hydraulic lines. Simultaneously, angular and vertical locations of the bucket were monitored with the angular and linear potentiometers, respectively. The results from the free-air experimentation may be seen in Figures 7.29, 7.30 and 7.31 for closing velocities of 20 deg/s, 15 deg/s and 10 deg/s respectively. It should be noted that the scatter is a result of the friction and stiction in the hydraulic cylinders.



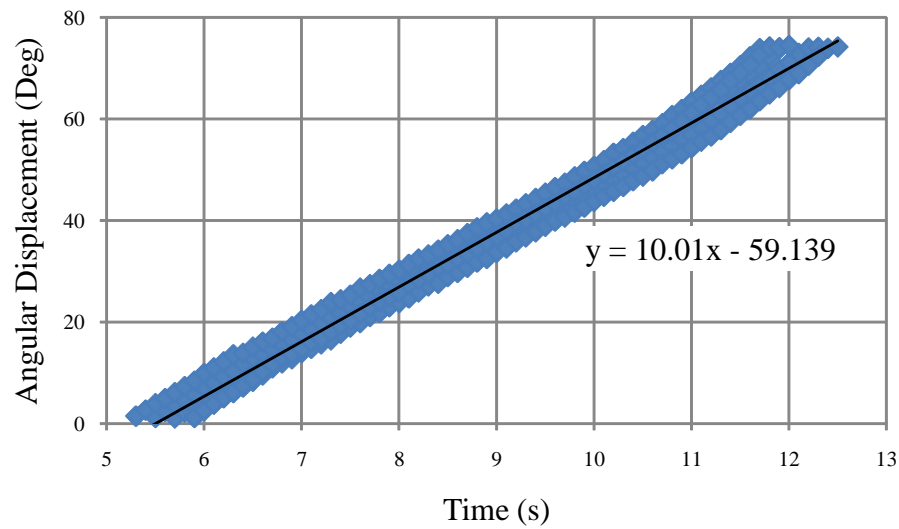


Figure 7.28: Variation of bucket angular displacement with time for a 10 deg/s closing velocity.

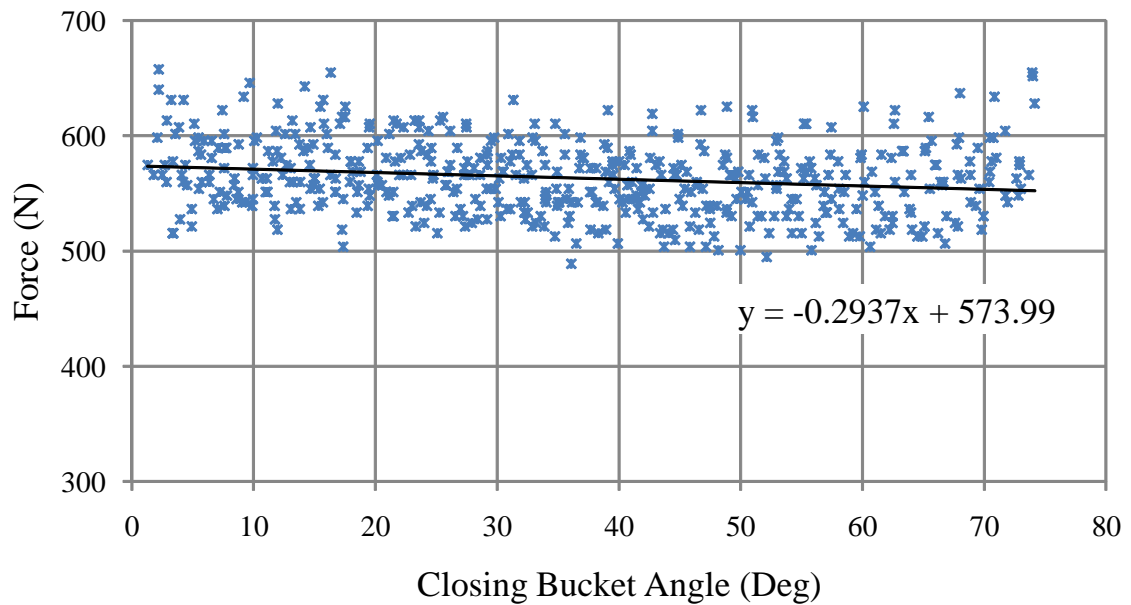


Figure 7.29: Free air (base) test for a 20 deg/s closing velocity.

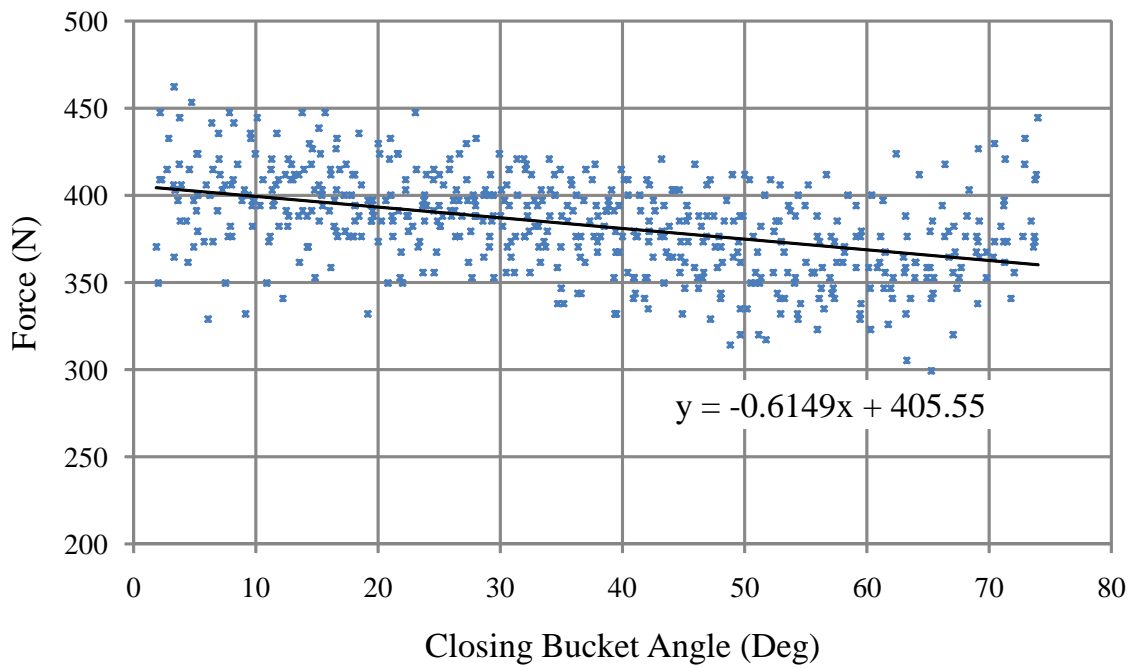


Figure 7.30: Free air (base) test for a 15 deg/s closing velocity.

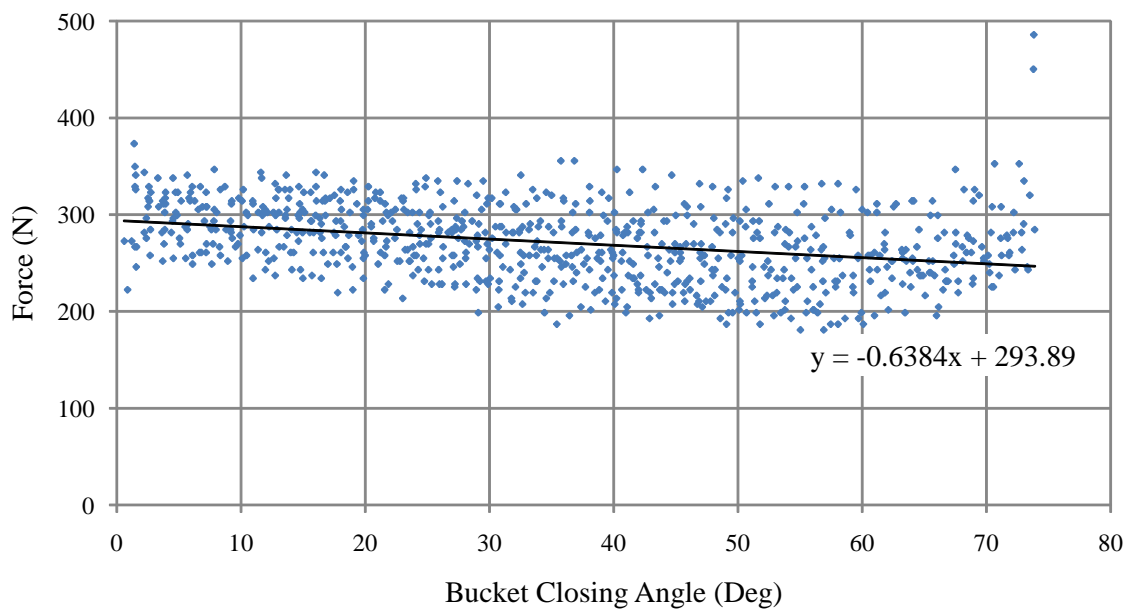


Figure 7.31: Free air (base) test for a 10 deg/s closing velocity.

## **Appendix F - Raw Data**

### **Tables of Raw Data**

Table 7.3 represents a sample of the raw data collected during a typical test run. The data found here is from a test conducted in the middle of the test bed, at an initial distance of 20 mm and a bucket closing velocity of 20 deg/s.

### **Tables of Converted Data**

Tables 7.4 and 7.5 represent raw data (voltage) converted from voltage to pressure and voltage to bucket angle respectively.

Table 7.3: Sample of the raw data generated, with a bucket velocity of 20 deg/s, in the middle of the granular bed and a penetration depth of 20 mm.

Run1 1 - Voltage - Dev1_ai3	
Channels	1
Samples	902
Date	10/15/2008
Time	22:47:16
Y_Unit_Label	Voltage (V)
X_Dimension	Time (s)
X0	16:29.9
Delta_X	0.025
***End_of_Head er***	
X0	Y_Unit_Label
0	2.233049
0.025	2.215225
0.05	2.22541
0.075	2.227957
0.1	2.222864
0.125	2.219045
0.15	2.226683
0.175	2.230503
0.2	2.212679
0.225	2.219045
0.25	2.222864
0.275	2.226683
0.3	2.212679
0.325	2.221591
0.35	2.217772
0.375	2.222864
0.4	2.222864
0.425	2.219045
0.45	2.231776
0.475	2.224137
0.5	2.217772

Table 7.4: Sample of raw data converted into a pressure.

Time (s)	Voltage (V)	Current (A)	Pressure (kPa)
7.5	2.170666	0.003975579	-0.321072366
7.525	2.785583	0.005101845	6.738084696
7.55	2.401101	0.004397621	2.32428767
7.575	2.482581	0.004546852	3.259666132
7.6	2.463484	0.004511875	3.04043537
7.625	2.476215	0.004535192	3.186585385
7.65	2.473669	0.004530529	3.157357678
7.675	2.464757	0.004514207	3.055049223
7.7	2.459665	0.004504881	2.99659381
7.725	2.478761	0.004539855	3.215813092
7.75	2.467303	0.00451887	3.08427693
7.775	2.46985	0.004523535	3.113516117
7.8	2.46603	0.004516538	3.069663077
7.825	2.482581	0.004546852	3.259666132
7.85	2.463484	0.004511875	3.04043537
7.875	2.464757	0.004514207	3.055049223
7.9	2.453299	0.004493222	2.923513062
7.925	2.483854	0.004549183	3.274279985
7.95	2.477488	0.004537524	3.201199238
7.975	2.480035	0.004542189	3.230438425

Table 7.5: Sample of raw data converted into an angular displacement.

Time (s)	Voltage (V)	Bucket Angle (Deg)
7.5	6.195193	0.96964291
7.525	6.199009	1.06836283
7.55	6.224448	1.72646976
7.575	6.23844	2.0884428
7.6	6.265151	2.77945637
7.625	6.280415	3.17433605
7.65	6.30967	3.9311629
7.675	6.330022	4.45766914
7.7	6.354189	5.08286943
7.725	6.369453	5.47774911
7.75	6.389804	6.00422948
7.775	6.4127	6.596549
7.8	6.436867	7.22174929
7.825	6.457219	7.74825553
7.85	6.475026	8.20892262
7.875	6.497922	8.80124214
7.9	6.511913	9.16318931
7.925	6.538625	9.85422875
7.95	6.557704	10.34780248
7.975	6.579328	10.90721536

## Variability of Experimental Data

Figure 7.32 to 7.34 show the variability in the data for a number of test conditions. They display all of the data for all of the runs for each test condition.

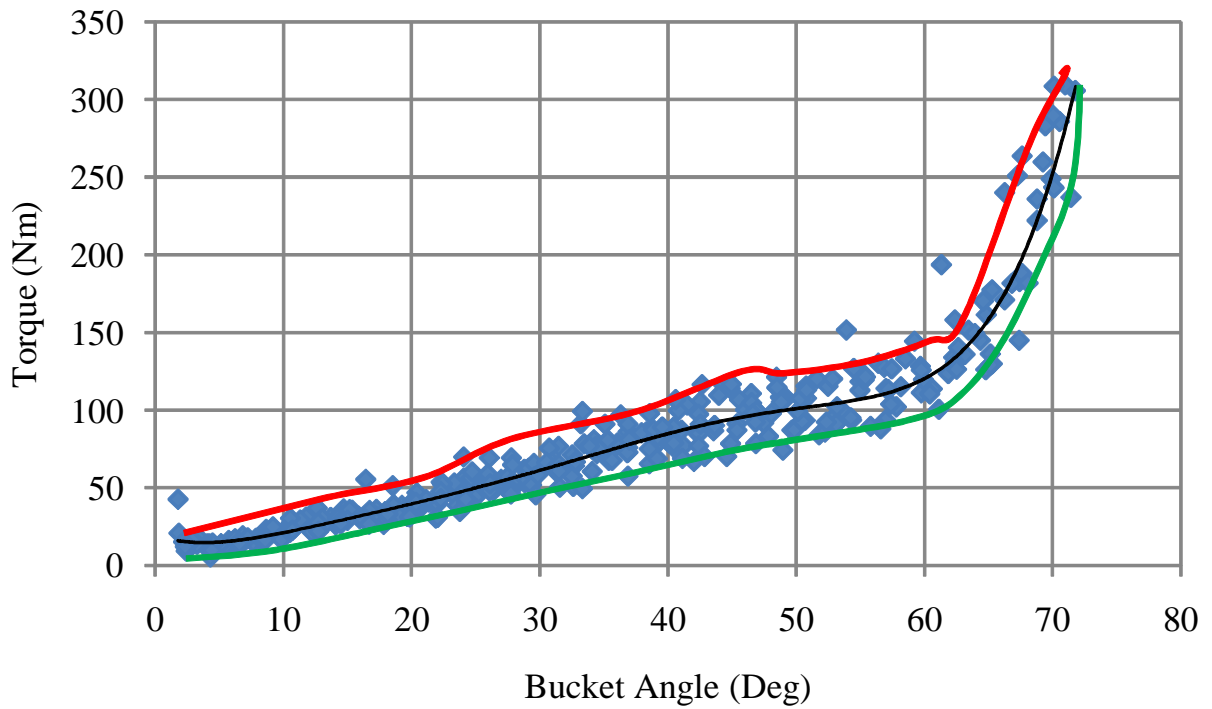


Figure 7.32: Typical variation of torque with bucket angle for a bucket closing velocity of 20 deg/s, in the middle, starting at 10 mm from the surface of the material.

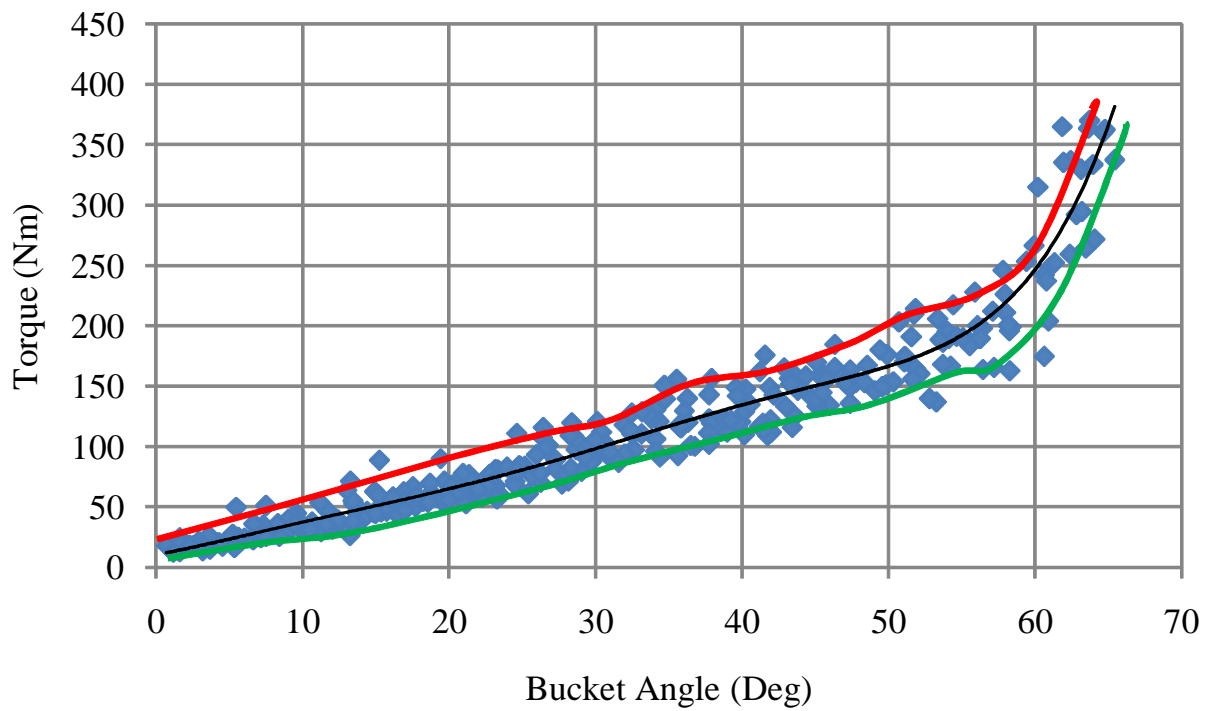


Figure 7.33: Typical variation of torque with bucket angle for a bucket closing velocity of 20 deg/s, in the middle, starting at 0 mm from the surface of the material.

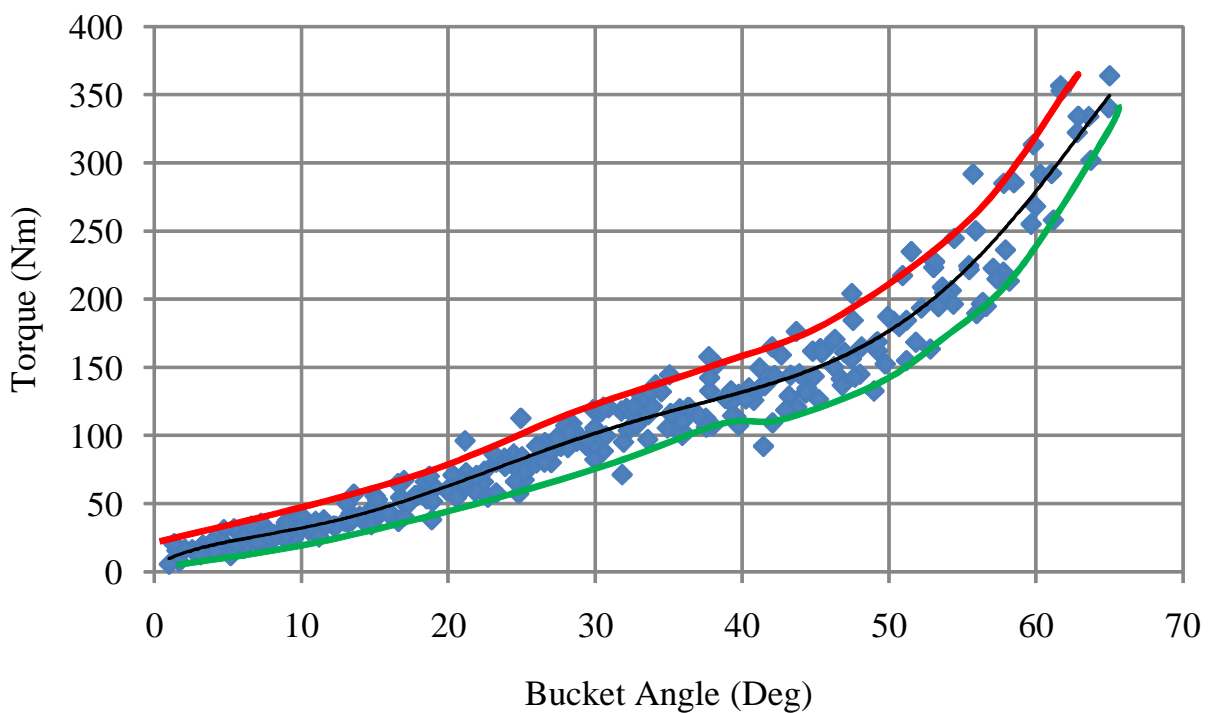
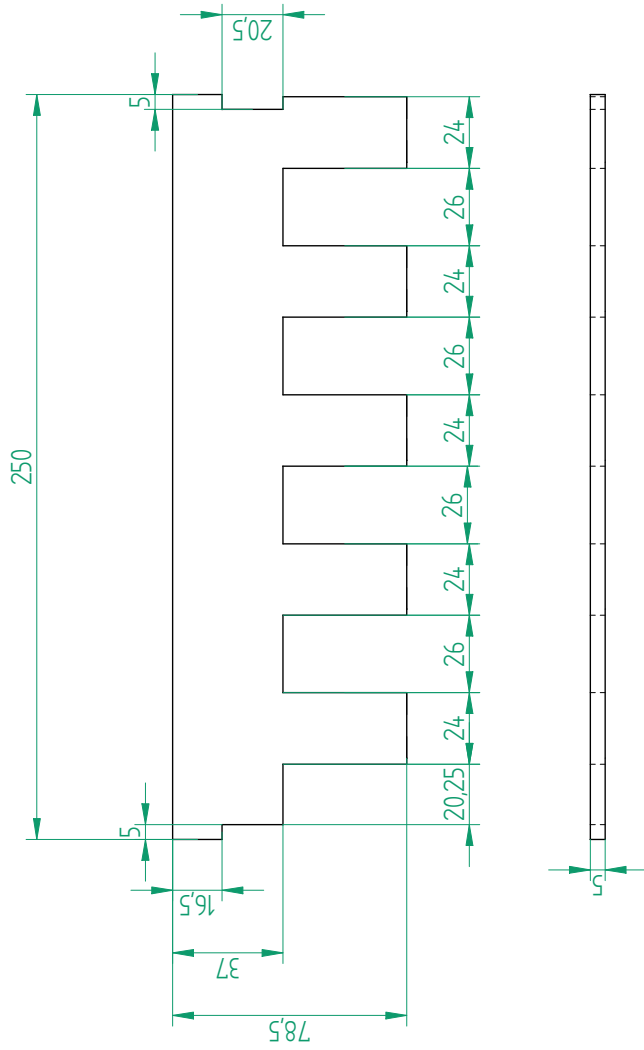


Figure 7.34: Typical variation of torque with bucket angle for a bucket closing velocity of 20 deg/s, at the forward/polycarbonate boundary, starting at 0 mm from the surface of the material.

## **Appendix G - Technical Drawings**

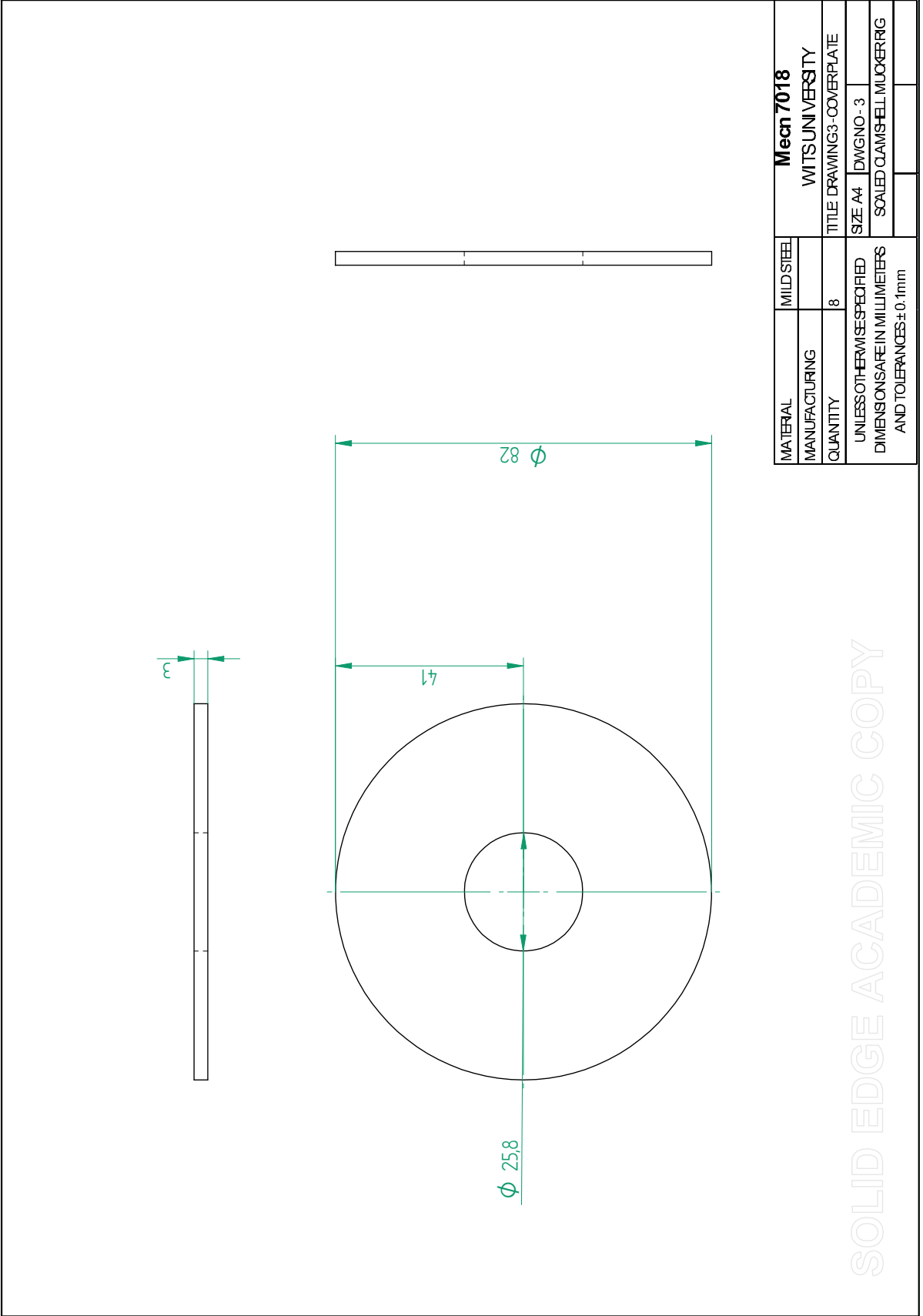






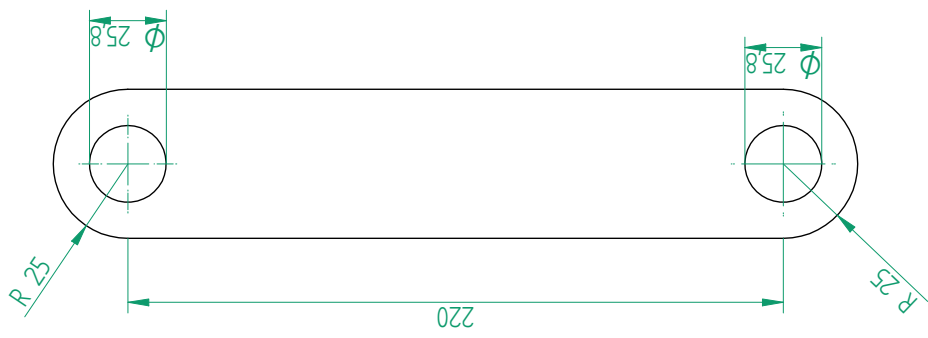
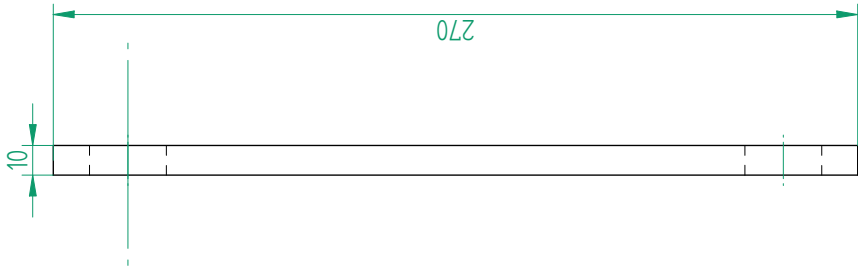
MATERIAL	MILD STEEL	<b>Mecn7018</b>	
MANUFACTURING		WITSUNIVERSITY	
QUANTITY	2	TITLE DRAWING2-JAW	
UNLESS OTHERWISE SPECIFIED DIMENSIONS ARE IN MILLIMETERS AND TOLERANCES ±0.1mm		SIZE A4	DWGNO - 2
		SCALED CLAMSHELL MUCKERRIG	

SOLID EDGE ACADEMIC COPY



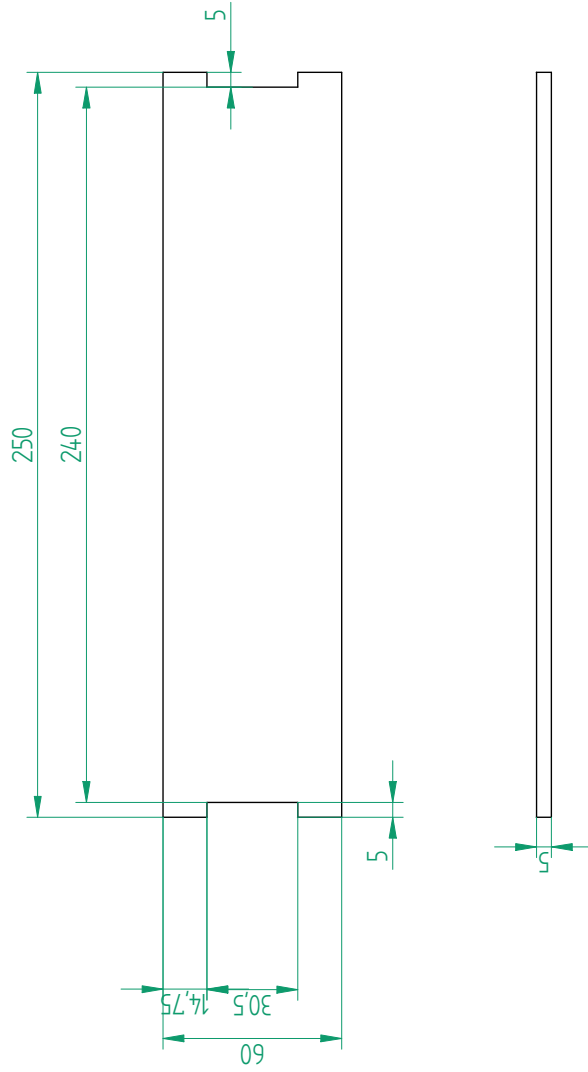
MATERIAL	MILD STEEL	<b>Mecn 7018</b>	
MANUFACTURING		WITS UNIVERSITY	
QUANTITY	8	TITLE DRAWING3-COVERPLATE	
UNLESS OTHERWISE SPECIFIED DIMENSIONS ARE IN MILLIMETERS AND TOLERANCES $\pm 0.1\text{mm}$		SIZE A4	DWGNO - 3
		SCALED CLAIMSHELL MUCKERRIG	

SOLID EDGE ACADEMIC COPY



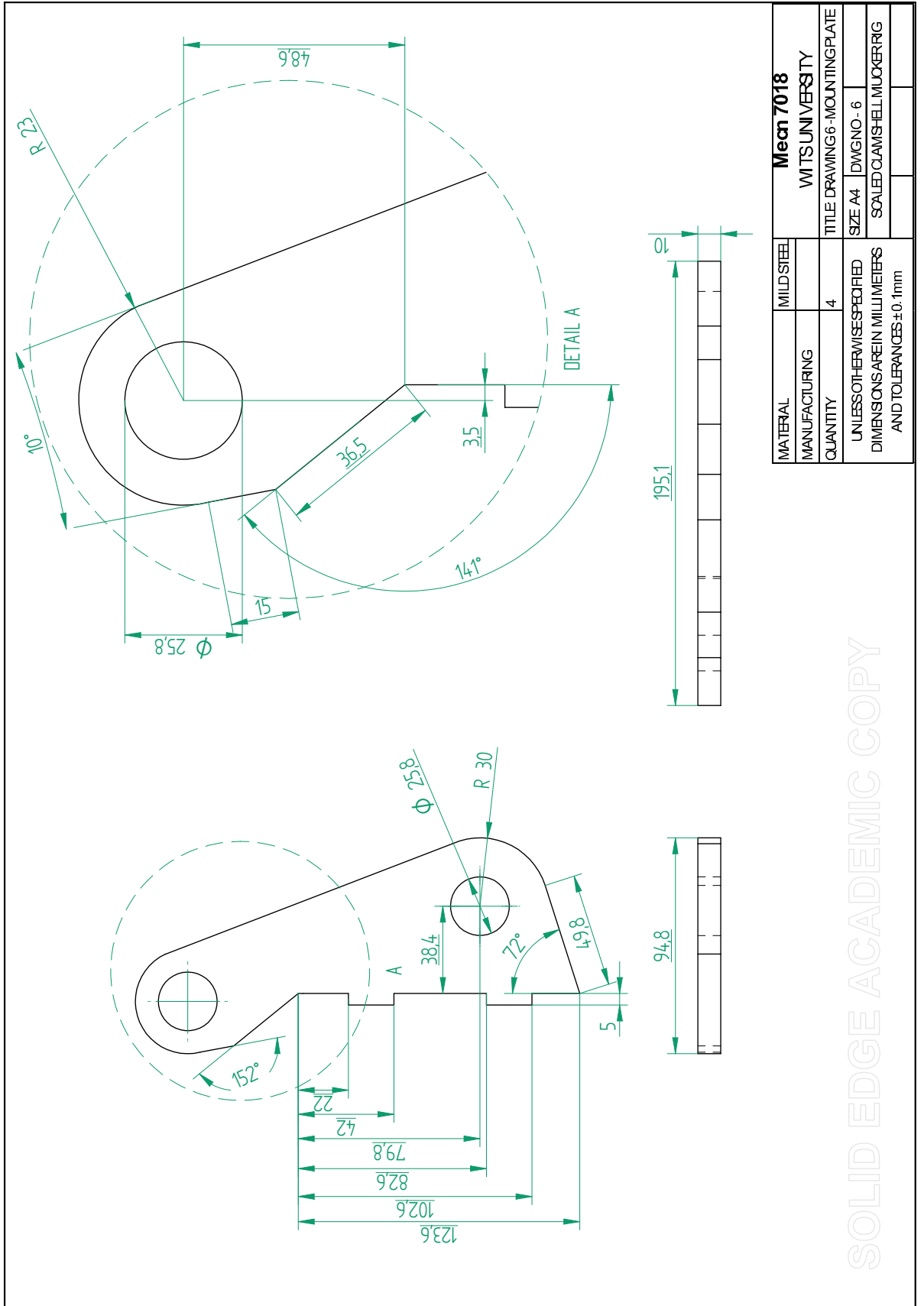
MATERIAL	MILD STEEL	<b>Mecn 7018</b>	
MANUFACTURING		WITSUNIVERSITY	
QUANTITY	8	TITLE DRAWING 4-LINKAGE	
UNLESS OTHERWISE SPECIFIED DIMENSIONS ARE IN MILLIMETERS AND TOLERANCES ± 0.1mm		SIZE A4	DWG NO - 4
		SCALED CLAMSHELL MUCKER RG	

SOLID EDGE ACADEMIC COPY



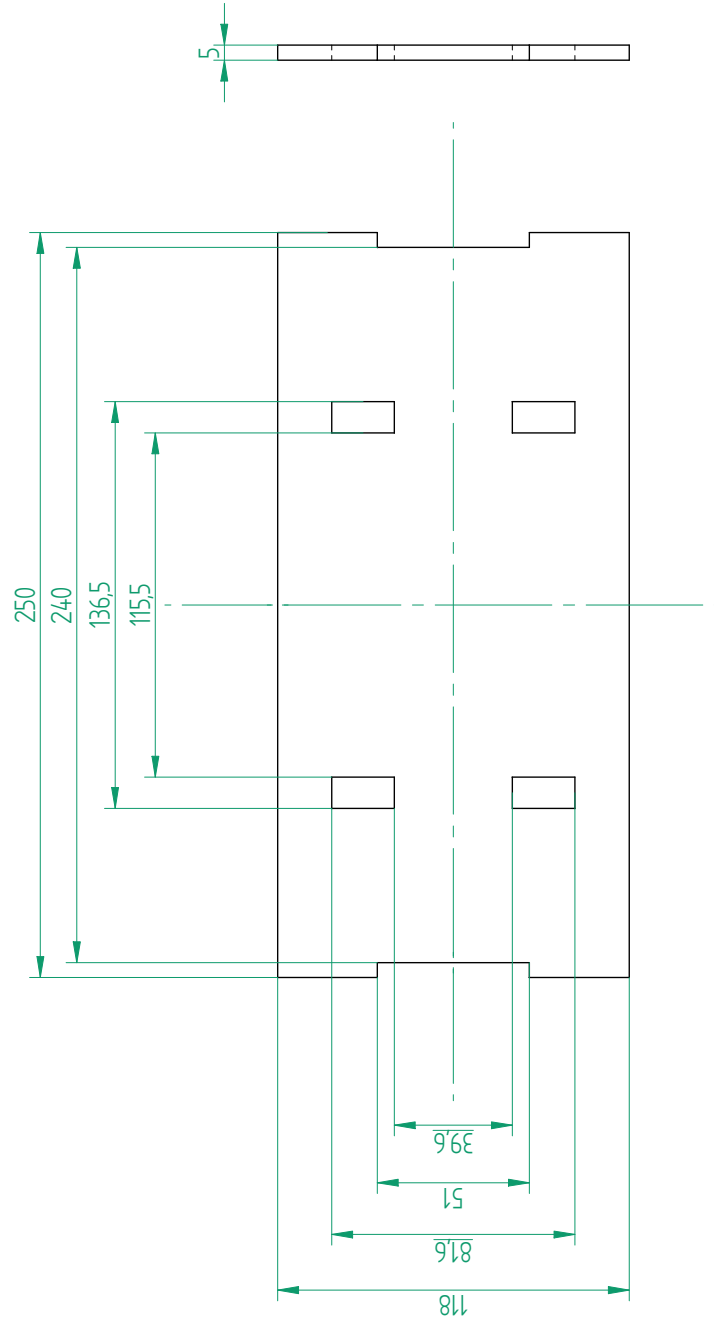
MATERIAL	MILD STEEL	<b>Mecn 7018</b>	
MANUFACTURING		WITSUNIVERSITY	
QUANTITY	2	TITLE DRAWING 5 - MIDPLATE	
UNLESS OTHERWISE SPECIFIED DIMENSIONS ARE IN MILLIMETERS AND TOLERANCES ±0.1mm		SIZE A4	DWGNO - 5
		SCALED CLAMSHELL MUCKERRIG	

SOLID EDGE ACADEMIC COPY



SOLID EDGE ACADEMIC COPY

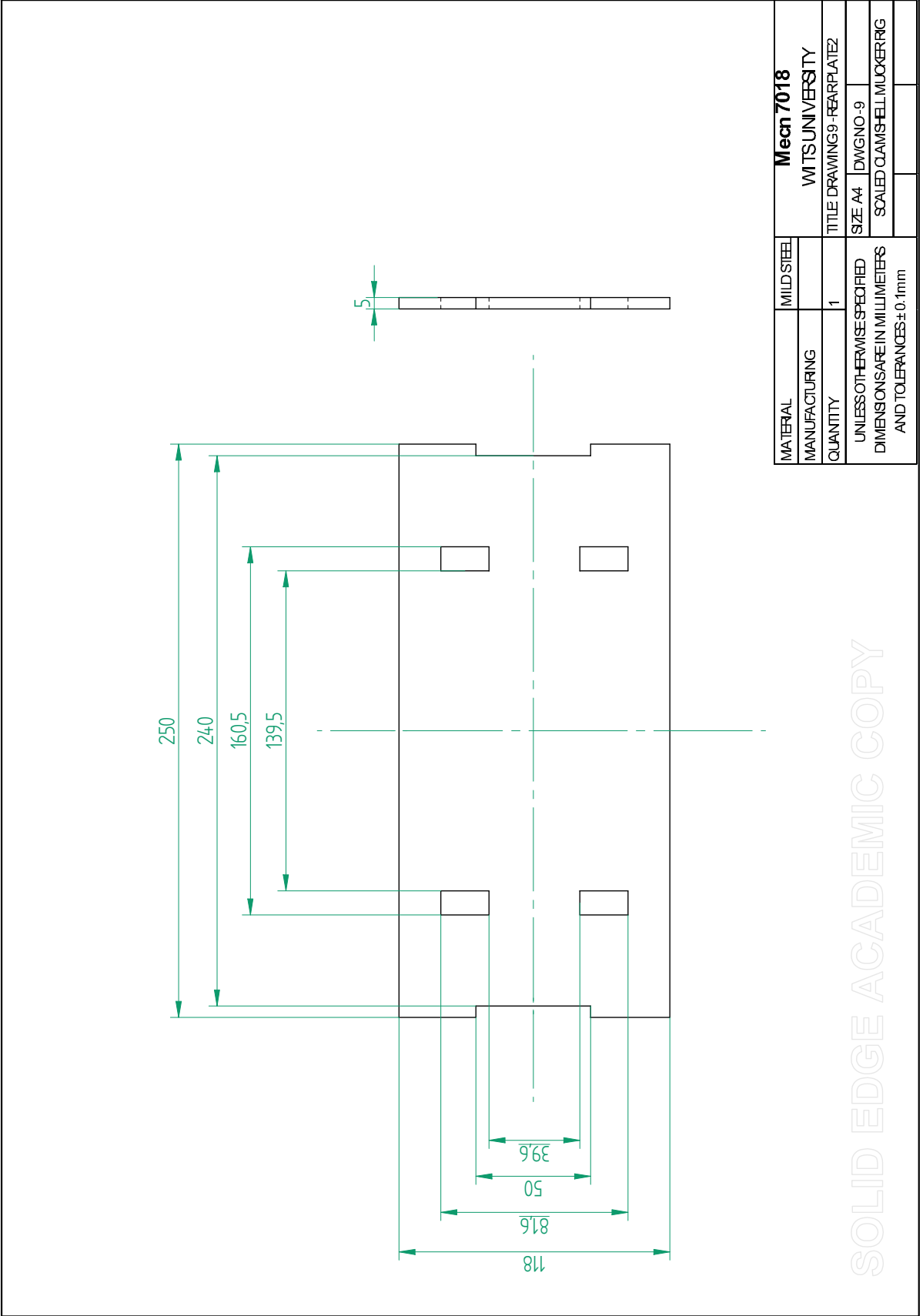




MATERIAL	MILD STEEL	<b>Meen 7018</b>	
MANUFACTURING		WITSUNIVERSITY	
QUANTITY	1	TITLE DRAWING: 8-REAR PLATE	
UNLESS OTHERWISE SPECIFIED DIMENSIONS ARE IN MILLIMETERS AND TOLERANCES ± 0.1mm		SIZE A4	DWGNO-8
		SCALED CLAIMSHELL/MUCKERIG	

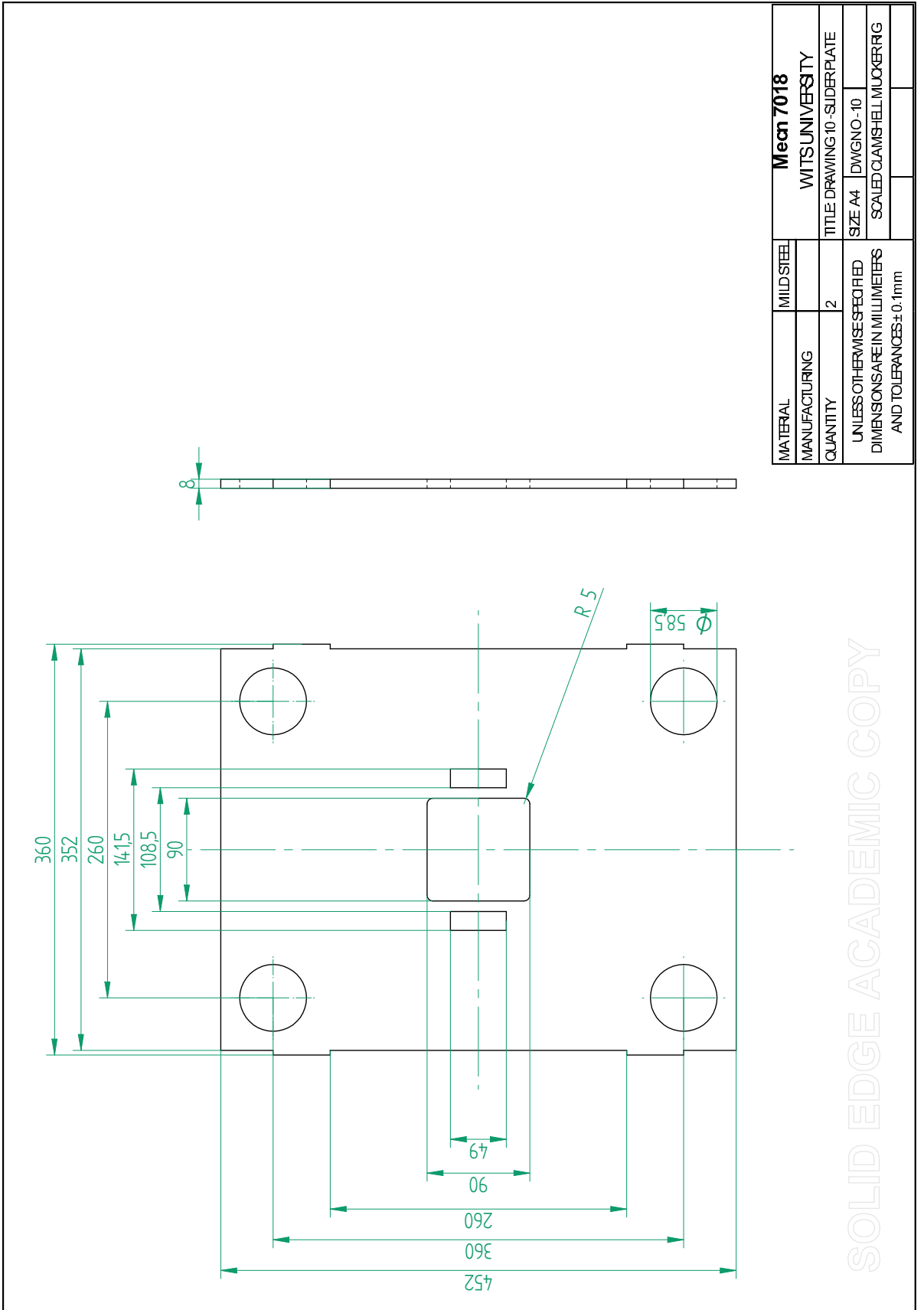
SOLID EDGE ACADEMIC COPY



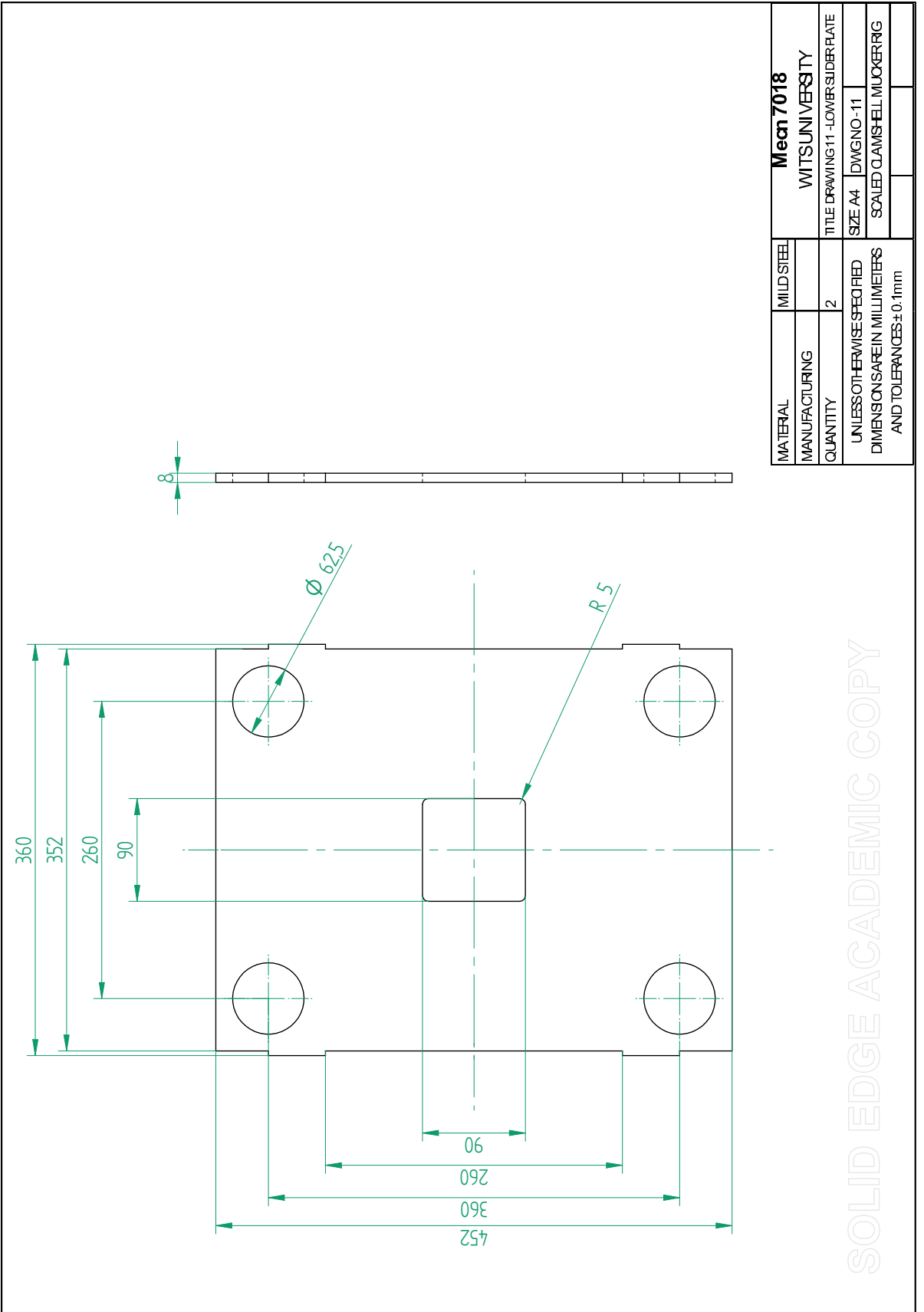


MATERIAL	MILD STEEL	<b>Mecn 7018</b>	
MANUFACTURING		WITSUNIVERSITY	
QUANTITY	1	TITLE DRAWING9-FEARPLATEZ	
UNLESS OTHERWISE SPECIFIED DIMENSIONS ARE IN MILLIMETERS AND TOLERANCES ± 0.1mm		SIZE A4	DWG NO-9
		SCALED CLAM-SHELL MUCKERIG	

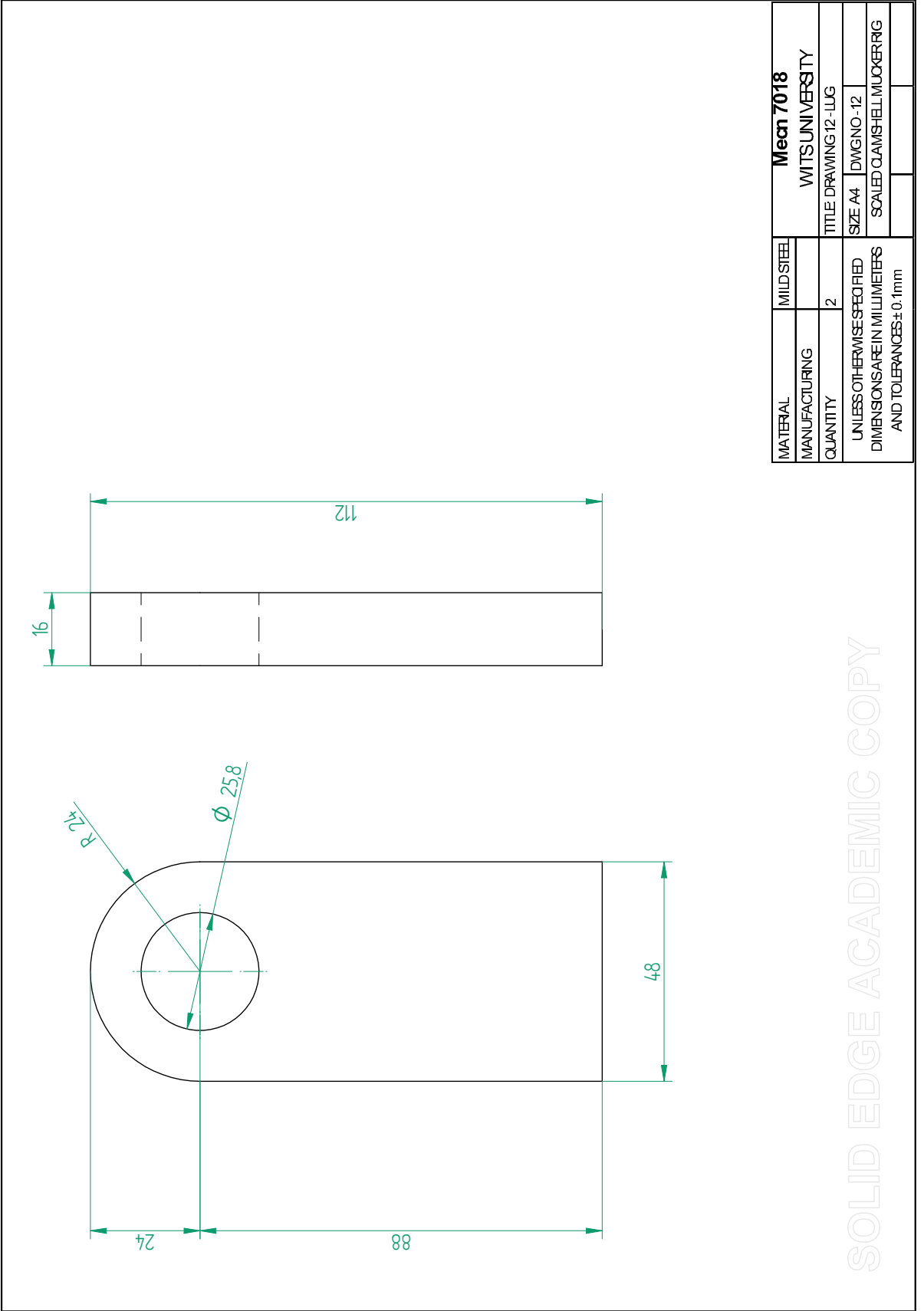
SOLID EDGE ACADEMIC COPY



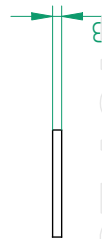
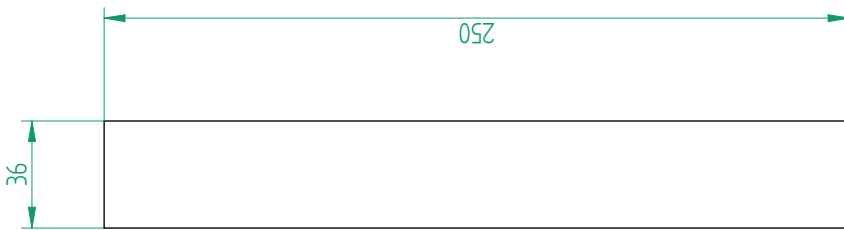
SOLID EDGE ACADEMIC COPY



SOLID EDGE ACADEMIC COPY

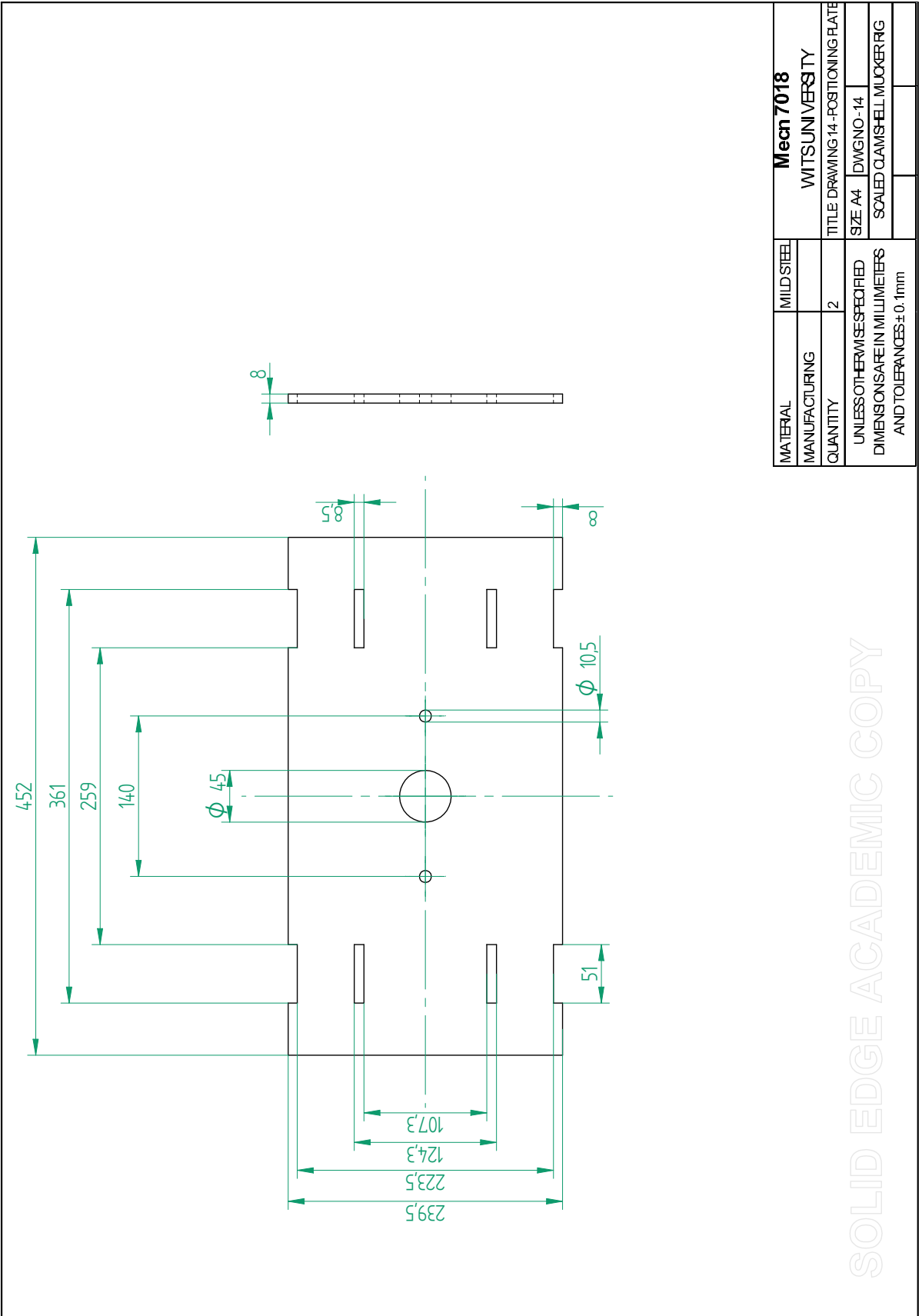


SOLID EDGE ACADEMIC COPY



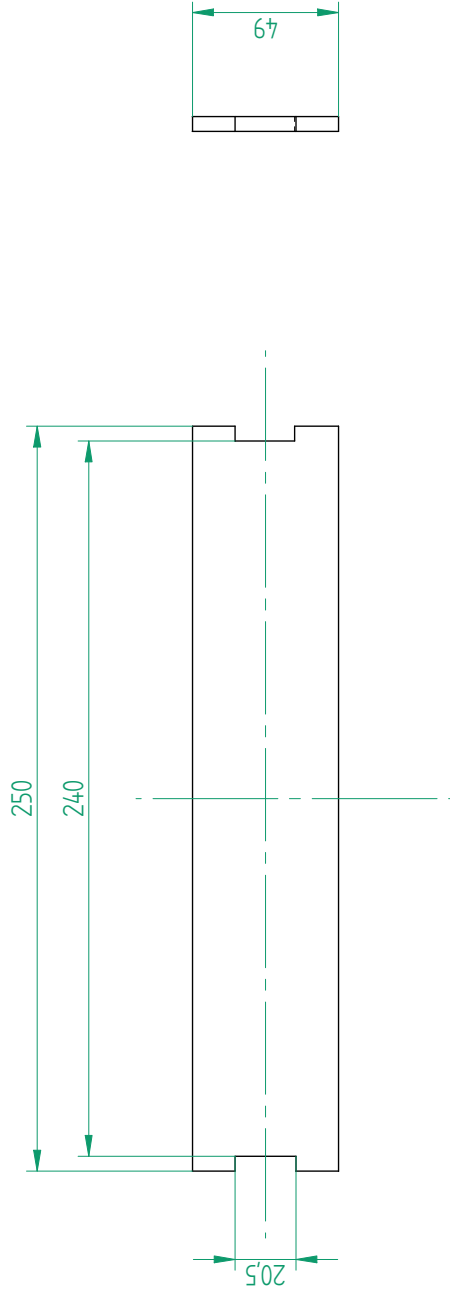
SOLID EDGE ACADEMIC COPY

MATERIAL	MILD STEEL	<b>Mecn 7018</b>	
MANUFACTURING		WITSUNIVERSITY	
QUANTITY	2	TITLE DRAWING 14-BUCKET STRUT	
UNLESS OTHERWISE SPECIFIED DIMENSIONS ARE IN MILLIMETERS AND TOLERANCES $\pm 0.1\text{mm}$		SIZE A4	DWG NO -13
		SCALED CLAIMSHELL MUCKER RIG	



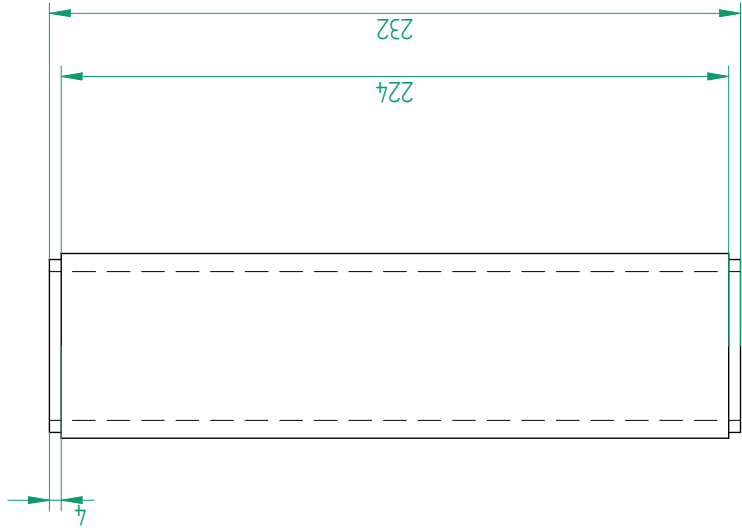
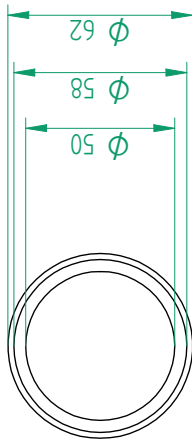
MATERIAL	MILD STEEL	<b>Mecn 7018</b>	
MANUFACTURING		WITSUNI UNIVERSITY	
QUANTITY	2	TITLE DRAWING 14 - POSITIONING PLATE	
UNLESS OTHERWISE SPECIFIED DIMENSIONS ARE IN MILLIMETERS AND TOLERANCES $\pm 0.1$ mm		SIZE A4	DWG NO - 14
		SCALED CLAMSHELL MUCKER RIG	

SOLID EDGE ACADEMIC COPY



MATERIAL	MILD STEEL	<b>Mecn 7018</b>	
MANUFACTURING		WITSUNIVERSITY	
QUANTITY	2	TITLE DRAWING 15 - TOP PLATE	
UNLESS OTHERWISE SPECIFIED DIMENSIONS ARE IN MILLIMETERS AND TOLERANCES ± 0.1mm		SIZE A4	DWGNO - 15
		SCALED CAMSHELL MUCKERRIG	

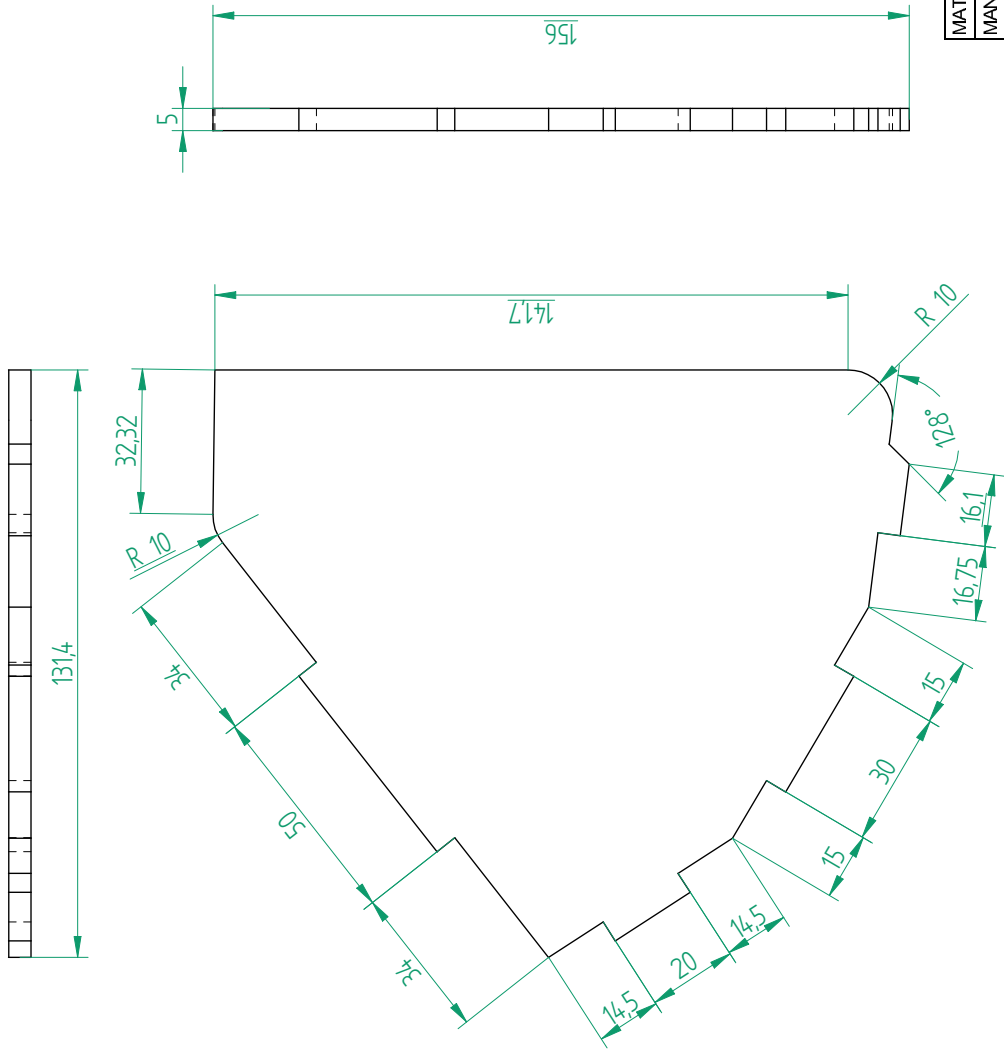
SOLID EDGE ACADEMIC COPY



MATERIAL	MILD STEEL	<b>Mecn 7018</b>	
MANUFACTURING	HONED TUBE	WITSUNI VERSITY	
QUANTITY	4	TITLE	DRAWING: 16 - BEARING ROD
UNLESS OTHERWISE SPECIFIED DIMENSIONS ARE IN MILLIMETERS AND TOLERANCES $\pm 0.1\text{mm}$		SIZE: A4	DWG NO: -16
		SCALED: CLAMSHELL MUCKER RIG	
		SCALE: 2:1	

SOLID EDGE ACADEMIC COPY





MATERIAL	MILD STEEL	<b>Mecn 7018</b>	
MANUFACTURING		MITSUNIVERSITY	
QUANTITY	2	TITLE DRAWING 16- CLOSED SIDE	
UNLESS OTHERWISE SPECIFIED DIMENSIONS ARE IN MILLIMETERS AND TOLERANCES ±0.1mm		SIZE A4	DWG NO - 16
		SCALED CLAM SHELL MUCKER RIG	

SOLID EDGE ACADEMIC COPY

